ESTABLISHING PROBABILITY OF FAILURE OF A SYSTEM DUE TO ELECTROMAGNETIC INTERFERENCE

By

VIGNESH RAJAMANI

Bachelor of Engineering (ECE)
University of Madras, India
2002

Master of Science in Electrical Engineering
Oklahoma State University
Stillwater, OK
2004

Submitted to the Faculty of the
Graduate College of the
Oklahoma State University
in partial fulfillment of
the requirements for
the Degree of
DOCTOR OF PHILOSOPHY
July 2010

ESTABLISHING PROBABILITY OF

FAILURE OF A SYSTEM DUE TO

ELECTROMAGNETIC INTERFERENCE

Dissertation Approved:

Dr. Charles F. Bunting

Dissertation Adviser

Dr. James C. West

Dr. Rama G. Ramakumar

Dr. Manjunath Kamath

Dr. Mark. E. Payton

Dean of the Graduate College

ACKNOWLEDGMENTS

This thesis has had mentorship from numerous outstanding individuals both from within the university and outside of it. Many people have been a part of my graduate education, as friends, teachers, and colleagues. Dr. Charles F. Bunting, first and foremost, has been all of these. The best advisor and teacher I could have wished for, he is actively involved in the work of all his students, and clearly always has their best interest in mind. Thank you for pushing me. On the personal side, he did not hesitate to invite his students to become an extended part of his family.

I have been indebted in the preparation of this thesis to Dr. James C. West whose patience and kindness, as well as his academic experience, has been invaluable to me. My special thanks are to Dr. Rama Ramakumar for his advice in Markov Chain modeling. Dr. Kamath Manjunath has been instrumental in advising me on the final part of this thesis and my hearty thanks goes out to him.

I shall always be grateful to Dr. Gustav Freyer for the long telephonic discussions we had together and the knowledge I gained from him. This work would not have been possible without the support and encouragement of, Ted Lehman whom I know is wishing me well from above.

I would like to thank several of my friends for helping with the preparation of this thesis especially my lab mates. Their honest yet considerate criticisms of this work have helped much in improving its quality. I cannot end without thanking my wife Subha, the constant support and encouragement from her which was always there when I needed it.

Lastly, and most importantly, I wish to thank my parents, Rajamani and Bhama. They bore me, raised me, supported me, taught me, and loved me. To them I dedicate this thesis.

TABLE OF CONTENTS

LIST OF TABLES

LIST OF FIGURES

LIST OF SYMBOLS

V – Volume

D – Directivity

λ – Wavelength and scale parameter

r – Distance between antennas

S_{21} – Transmission coefficient

$\frac{\langle P_r \rangle}{P_t} = \langle |S_{21}|^2 \rangle$ - Chamber gain

τ – Chamber time constant

A – *A*rea

c – Speed of light

η - Absorption coefficient

r_d - Reverberation distance

S – Surface Area

T_c - Wall scattering time

S_{11} and S_{22} – Reflection coefficient

ρ - Correlation coefficient

μ - Mean or permeability

σ – *Variance*

Γ - Gamma function

S_n – Normalized standard deviation

1/e – Time constant

E – Electric Field

$< P_r >$ - Average received power

ε - Permittivity

m, n and p – Mode numbers

a, b and c – Length, Width and Height of a cavity

f_0 – Resonant frequency of the first mode

$Z_{w\text{-}s}$elf impedance of the wire

Γ_w - Reflection coefficient of the wire

Z_0 - Characteristic impedance

Z_L - Load impedance

Z_A - self impedance of the wire

I_L - Load current

V_L - Load voltage

V_{OC} - Open circuit voltage

I_{SC} - Short circuit current

k – Shape parameter

N(t) - Number of active EM disturbances that occur during the time t

t_i - Arrival time i^{th} disturbance

d_i. - Duration of disturbance

α - Average (mean) number of successes per unit time

p – Conditional probability of failure in the presence of EMI

q and *r* – Transitional probabilities from EMI absent to present and vice versa

Ts - One step of duration

p1 and *p2* – Conditional probabiltity that EMI exists and causes a failure and EMI exists and does not cause a failure

LIST OF ACRONYMS

EMI/C – Electromagnetic Interference/Compatability

EME – Electromagnetic Environment

EUT – Equipment Under Test

OATS – Open Area Test Site

AC – Anechoic Chamber

RAM – Radar Absorbent Material

RF – Radio Frequency

RS – Radiated Susceptibility

RC – Reverberation Chamber

FALC – Fully Absorber Lined Chamber

SAC – Semi Anechoic Chamber

TEM – Transverse Electromagnetic Cell

GTEM – Gigahertz Transverse Electromagnetic Cell

LUV – Lowest Usable Volume

Q – Quality Factor

K – Rician Factor

VNA – Vector Network Analyzer

CW – Continuous Wave

LOS – Line of Sight

IL – Insertion Loss

Tx and Rx – Transmit and Receive antennas

CDF – Cumulative Distribution Function

JFTA – Joint Frequency and Time Analysis

BW – Band Width

LP – Log Periodic Antenna

FD – Frequency domain

TD – Time domain

IS – Independent Samples

VT – Vertical Tuner

HT – Horizontal tuner

ST – Small tuner

HERO – Hazard of Electromagnetic Radiation to Ordnance

D.O.F – Degrees of Freedom

MLFMA – Multi Level Fast Multipole Algorithm

OSU – Oklahoma State University

SE – Shielding Effectiveness

Chapter 1

1.0 INTRODUCTION

Electromagnetic interference can be defined as a disturbance, intentional or unintentional, emitted from an internal or external source that affects an electrical circuit. The disturbance can be just a nuisance or fatal depending on the severity of the situation. In order for the electronics to be electromagnetically compatible, the emissions and susceptibility levels must be established and proper care needs to be taken to shield the components to prevent damage.

Establishing the threat levels, both emission and susceptibility, are of critical importance. Most of the electronic components operate inside cavities or enclosures and assessing the electromagnetic damage and upset of these components under various conditions will provide insight to minimize such failures during operation. Estimating the failures becomes an ill defined problem when the details of the equipment, enclosure, interconnecting cables and surrounding geometrical details are not well known.

Reworking the solution for every change to the system in terms of size, position, etc… when performing theoretical or numerical analysis, advocates the need for statistical methods. These problems are challenging to simulate as it requires intricate details which

may not be quite consistent from one system to another. For example the cable routing is not very consistent between the same models of planes. Solving for every problem hence becomes an impossible task. Statistical methods use all these uncertainties that exist in such a problem to its advantage. These methods are widely applied in EMI/C problems due to the very nature of the problem and will be very heavily used in all our discussions.

The final outcome of this work is to establish the probability of failure due to current coupled onto a cable or a cable bundle that is located close to the wall of a cavity due to external or internal coupling of EM. The electromagnetic environment of the cavity needs to be determined to estimate the probability of threat depending on the location of the cable inside the cavity. Given that the probability of threat exists, then the probability that the value of the current or field that exceeds a certain threshold must also be determined. To obtain the threshold probability, the environment in which the EUT operates and the also the influence of the environment on the observable that is being targeted needs to be known. Finally, the net probability of failure of a system will be determined from the individual probabilities.

The important properties of the cavity that need to be known are the shape, size and volume of the cavity and also the material of the cavity along with what is present inside the cavity. The cavity could vary anywhere from a compartment in a submarine, aircraft cockpits, hallways, office spaces, warehouses, etc… to electronic equipments operating inside rectangular enclosures.

Conveniently most of the cavities in which electronics operate are rectangular in nature or at least the cavities can be approximated as rectangular cavities, hence simplifying some calculations. These environments can also be recreated in a laboratory setup easily making research on such problems plausible.

In this study a first order model will be analyzed experimentally to obtain the individual and net probabilities of observables and EMI failure. Brief introductions of test facilities that are at the disposal of an EMC engineer to analyze the common EMC/I problems are given below to enable the reader to understand the different electromagnetic environments (EME) that could exist and also ways to establish such EME that would enable testing of equipments in operational conditions. The limitations of each test facility will also be discussed. The extensive use of reverberation chambers for measurements and creating different electromagnetic environments for testing the first order model will be justified. Some of the details that need attention while using reverberation chambers and using reverberation techniques in other operational environments are also discussed.

1. 1 Open Area Test Site (OATS)

The Open Area Test Site (OATS) is a 3 and 10 meter emissions test range (Ref: Figure 1.1). An OATS facility must be free from any other electromagnetic disturbance. So the cables that are used to power the equipments, control lines, signal lines must be isolated from one another and usually run underground to a control room which will be again a

shielded room. The radiated field from the source reaches the equipment under test (EUT) via direct line of sight and via reflections from the ground plane usually enhanced by a steel sheet.

Limitations

The EUT must be placed on a turntable and turned to expose all parts of the EUT to the source field. Most OATS facilities are contaminated with noise from nearby transmission lines and cell phone towers. In order to perform a statistical study on the EME and also the effects of EUT to determine the probability of failure of the system, the EUT has to be tested at all possible angles of incidence and polarizations at every frequency which might not be practical to perform for all test objects. Hence this test technique will be used only when necessary.

Figure 1. 1 Open Area Test Site [64]

1. 2 Fully Anechoic chambers

An Anechoic chamber is a RF test facility where the electromagnetic wave echoes are suppressed (Ref: Figure 1.2). Such construction isolates the device under test present inside the anechoic chamber from any other electromagnetic interference. The EUT receives EM energy only from the source (usually in the line of sight) and there are minimum reflections from the walls, floor or roof. Anechoic chambers are used in antenna radiation pattern measurements, radar cross section measurements and electromagnetic compatibility measurements.

The lowest operating frequency determines the size of the chamber. The walls are coated with radar absorbent material (RAM) to minimize reflection. The equipment under test is placed on a turntable at a specified distance away from the source antenna. The source antenna is powered by a signal source and an amplifier. When a radiated susceptibility test is done, the antenna and the EUT on the turntable must be rotated to expose all parts of the EUT to the RF field. It is required by standards that the EUT must be completely enclosed in the 3dB bandwidth of the source antenna which becomes impossible when the EUT is large. Hence only parts of the EUT are exposed to the RF field.

A fully anechoic chamber is preferred for radiated susceptibility (RS) testing if a plane wave environment (with minimum reflections) is desired. In order to do a complete radiated susceptibility test, the entire sphere surrounding the device must be sampled to predict the direction maximum coupling to the device. This test is practically impossible and not economical to be performed in any situation. Because of the time and cost

involved usually the radiated susceptibility test in an anechoic chamber is performed over a limited number of aspect angles and polarizations which may cause a high risk of missing (and under-testing) some susceptibilities as many EUT's are highly directive (susceptible). The region where the field levels are not significantly different is defined as the uniformity region. It is necessary that the EUT is enclosed inside the uniformity region during the test as all parts of the EUT will be equally illuminated.

Limitations

The absorber material used in the construction of the chamber is not efficient in the 30-200 MHz range. Testing of equipment at microwave frequencies in an anechoic chamber (AC) may lead to stress levels on electronic components inside the equipment that are more than 10dB higher than what is achieved in a reverberation chamber (RC) [34], given the same magnitude of the exciting field and the known directivity of the EUT. The outcome of a radiated susceptibility test in an AC will strictly depend on the choice of the direction and polarization of the incident field. In case of an anechoic chamber, the field uniformity levels are not good (6-12 dB variation) giving rise to uncertainty levels that are large (not desirable for a susceptibility test). The uncertainty associated with this testing also limits the capability of arriving at a probabilistic model for failure. A thorough test will be required to establish the distributions with reasonable accuracy hence only limited tests will be performed in this study using FALC.

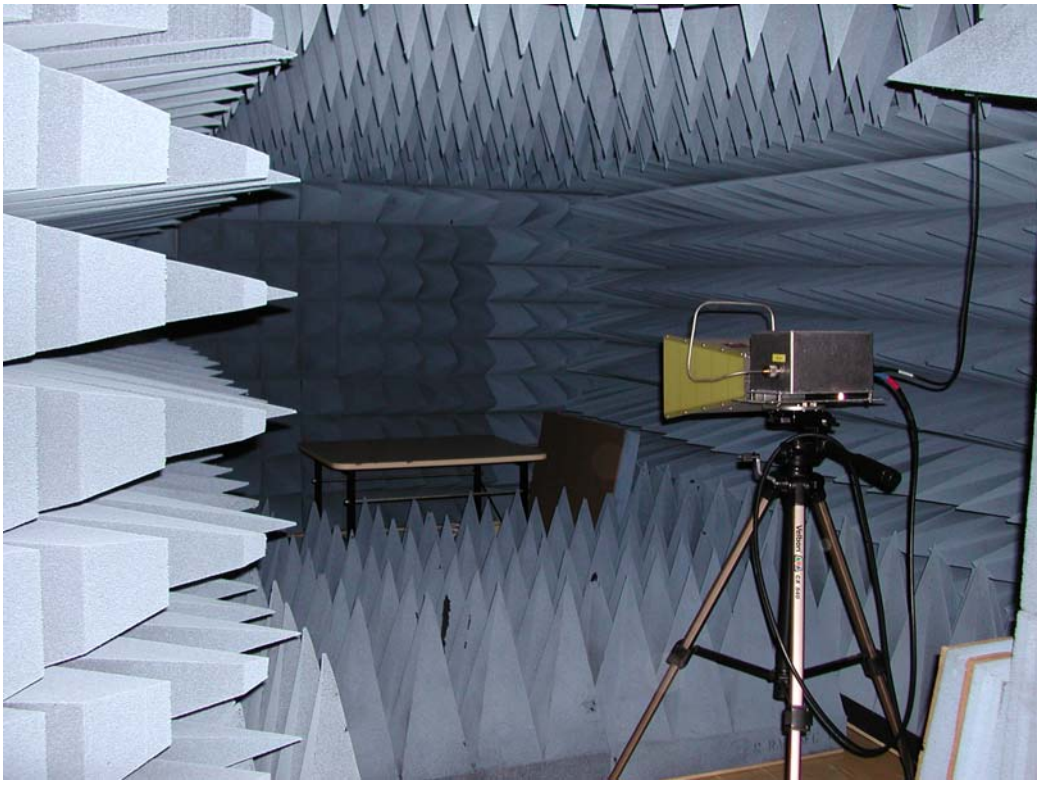

Figure 1. 2 Fully Absorber Lined Chamber or Anechoic Chamber [65]

1. 3 Semi Anechoic chambers

A semi anechoic chamber pretty much resembles an anechoic chamber in construction except for the absence of absorbing material on the floor and usually a metal sheet is provided as a floor to enhance reflections and simulate ground (Ref: Figure 1.3). The one advantage of a semi anechoic chamber is that the results can be directly compared to the results from an open area test site (OATS). Commercial radiated emissions standards demands testing inside a semi anechoic chamber. The advantages and disadvantages of using a semi anechoic chamber are similar to an anechoic chamber.

Limitations

In a semi anechoic chamber when radiated emissions or susceptibility measurements are made, reflections can produce unpredictable results. The variable results might be because of the standing waves (due to reflections). Variation is likely if the position of the test set up in the chamber is changed. Similar limitations to FALC exist with testing in semi anechoic chambers with respect to measuring an observable for statistical study.

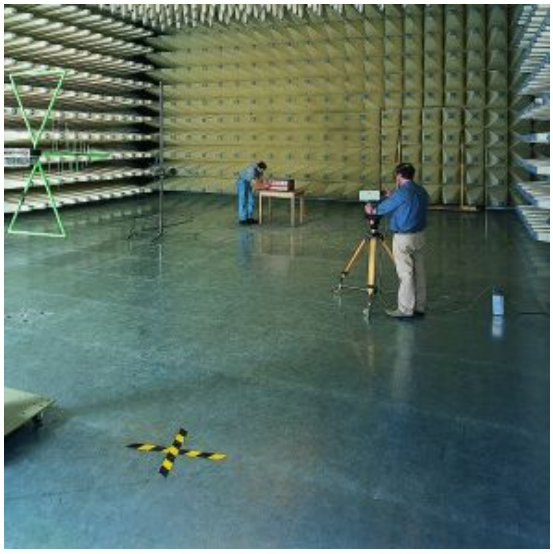

Figure 1. 3 Semi Anechoic Chamber [66]

1. 4 TEM

TEM is a type of guided wave environment which is a form of plane wave environment. Because of the uniformity of the test field, TEM cavities are used for probe calibration. Broadly TEM can be classified into TEM Cell, TEM Waveguide and GTEM cell.

1. 4. 1 TEM Cell

A closed measuring device consisting of an inner and an outer conductor in which a voltage difference creates a transverse electromagnetic (TEM)-mode electromagnetic field between these conductors (Ref: Figure 1.4). Two-port TEM cells typically have symmetrical tapered input and output ports, whereas a one-port TEM cell typically has a tapered input port and a integral, closed non tapered termination in place of the output port [67].

1. 4. 2 TEM Waveguide

An open or closed transmission line system that uses the TEM mode over the frequency range of interest is called a TEM waveguide. The TEM mode is defined as an electromagnetic field in which the electric and magnetic field vectors are orthogonal to each other and orthogonal to the propagation direction. Common examples are the two-port TEM cell (Crawford cell), the one-port or wideband-TEM cell (example GTEM), and the parallel-plate stripline [67].

1. 4. 3 GTEM

A TEM cell that has been altered to extend the usable frequency range is called a Gigahertz Transverse Electromagnetic Cell. Typically, this is achieved by replacing one port of a two-port TEM cell with a wideband, non-tapered, hybrid discrete resistor/wave

absorber termination [67]. GTEMs are also preferred for some RS testing but they are usually limited by size.

Limitations

The tapered geometry of TEM cell makes it impossible to use in some radiated susceptibility tests. It cannot enclose larger test bodies and so the applications are very limited. The field uniformity also degrades at higher frequencies. To do a 3D test inside GTEM both the antennas and the EUT must be rotated. TEM cells will not be used in any of the measurements.

Figure 1. 4 TEM cell [68]

1. 5 Reverberation chambers

A reverberation chamber is a large welded enclosure with highly conducting walls. Reverberation chambers are used to expose the EUT to random electromagnetic fields at high frequencies (Ref: Figure 1.5). The vulnerability of the equipment is tested under robust conditions of electromagnetic exposure inside the reverberation chamber. In the case of an Anechoic or a Semi Anechoic chamber, the field structure can be defined as plane wave. Because of the presence of absorbing walls, the EUT is exposed to the fields in only one direction. In order to do a susceptibility test, the EUT must be placed on a turntable to expose all parts of the EUT to the fields but in the case of a reverberation chamber, due to highly reflecting walls, the EUT is illuminated by fields from many aspect angles. Hence the EUT need not be rotated inside the chamber. Reverberation chamber closely resembles the environment in which the EUT will be operating when it is placed inside a cavity. The field structure inside the reverberation chamber can be considered as a superposition of plane waves at random phases [1].

Random fields are created inside the reverberation chamber by varying the boundary conditions of the chamber walls. This is accomplished usually with the use of a tuner which is typically both electrically large and occupies an appreciable portion of the cavity volume. This is referred to as mechanical stirring or mode stirring. The input frequency can be varied over a band to realize the complexity inside the chamber and this method of stirring is called frequency stirring. RF energy will be injected into the chamber at one of the corners and allowed to reflect on the side walls, top and bottom plates several times

before reaching the EUT. The revolving tuner also contributes to this phenomenon by changing the path lengths of the waves. In all through our analysis, phase will be considered to be evenly distributed (uniform) inside the chamber and no analysis will be done with the phase information.

The reverberation chamber is an ensemble of a large number of cavities with different shapes [2]. The well stirred field inside the reverberation chamber also satisfies Maxwell's equations. The fields inside a stirred reverberation chamber can be approximated by a sum of plane waves which highly helps in calculating the responses of the test objects [1]. Because of the multipath scattering inside reverberation chambers, the phase information is totally lost [3]. Thus the field inside the well stirred chamber is the sum of large number of multipath rays with random phases.

Deterministic mode theory is not suitable for predicting the response of the test object that is present inside a mechanically stirred reverberation chamber because the problem has to be solved for every change (antenna, EUT position, tuner position etc..) which becomes impractical and hence statistical theory has to be employed to resolve for the fields near or on the EUT. The field that is created inside the reverberation chamber is stochastic in nature, so statistical techniques will be applied to analyze these fields.

The range of possible measured responses, indicated by the uncertainty levels, is generally smaller in a reverberation chamber test. The EUT is equally illuminated in all directions hence the effective directivity of the RC is one. The EUT inside the lowest

usable volume (LUV) of the RC will still respond depending on its directivity but the chances of finding more susceptible parts inside an RC is more than in any other test facility.

Figure 1. 5 Reverberation Chamber

Limitations

For radiated susceptibility testing, the EUT has to be exposed to certain field levels as specified by a standard [4, 5]. Though frequency stirring is a valid method to expose the EUT inside a reverberation chamber, the standard calls for mechanical stepping (the tuner is stopped before taking a measurement) with a minimum of 12 tuner positions at all frequencies. While this process is efficient, the test time can be significant. Mechanical stirring (the tuner is rotated continuously) is another means by which a similar field change could be attained. A more important question may be “How long is the EUT being exposed to that same/required field level during the continuous rotation of the tuner?” Rotation of a tuner combined with an effective change in frequency, for which the equipment must be tested, may be a method to reduce the test time. This will be

discussed again after establishing the failure models for different device types. Once the failure model is developed, an appropriate test method could be chosen to reduce the test time.

The number of discrete tuner steps increases with decrease in frequency of operation due to the inability of the tuner to generate statistically independent fields. This increases the test time considerably. Continuous tuner rotation can reduce the test time provided the EUT responds quickly to the rapidly changing local fields. To identify the response of the devices to the EM field, the failure mechanisms of different components and devices that will be installed in aircrafts/automobiles/consumer electronics must be studied. If most of the devices respond to a peak field more than an average field, then continuous rotation of the tuner can be considered.

In a mechanically stepped test, the EUT is exposed to a particular intensity of field for a period called the dwell time for the EUT. By rotating the tuner at a faster rate, a cumulative dwell time can be established. The tuner can be rotated at a rate faster than the decay rate of the modes inside RC which then can retain the same field level for the period of time needed. Though this seems to be a viable option, more research has to be done to support this argument. Though this issue is not directly addressed in this work, the failure models developed will help in answering some of these questions.

1. 6 Why use Reverberation Chamber in this study?

The statistical nature of the fields inside the RC represents the field structure that exists in cavities in which electronics operate. There is also a need for "in-situ testing" i.e.… to test the equipments during its operation in a particular location and also assessing the influence of EMI when a new system is installed in the same space. The statistics that govern the typical RC operation are also well established hence throughout this problem, most of our tests will be performed in RC but often, comparisons will be made to other test techniques like OATS and AC for cross checks.

To understand the statistical nature of the problem and how to apply the statistics to very complex scenarios, this study will focus on analyzing some simple and somewhat ideal cases to begin with. Such cases involve the determination of field and power distributions as well as induced currents in the "middle" of sparse or unloaded cavities using simple aperture models. The study then investigates how the distributions change as a function of excitation frequency, cavity modes, and more complex aperture models. More complicated overmoded cavities generated by the variation of frequency, cavity fill etc will be discussed while closely examining the EM phenomena occurring at/near interior metallic walls and surfaces representing cables for example.

The complications and complexities that will arise due to the variability of cavity fill, existence of multiple apertures of various types, EM source characteristics, near-field proximity effects, and so forth will help answer another critical research question: Are

there other effective ways of reducing simulation complexity in addition to applying statistics? It is anticipated that this research will result in a set of guidelines that may alleviate the need to unnecessarily generate highly-detailed computational models especially if there are no enhanced accuracy obtained due to simulation of every minor change that occurs in the system.

Reverberation chambers will be used in all the measurements performed on the metal box with apertures. A piece of wire placed inside the metallic box will serve as the equipment under test and the distributions of current and fields will be calculated via measurements. From the distribution, the probability that the observable exceeding a certain threshold can be determined. From the nature of the EME generated, the probability of threat can be determined. Combining both the probabilities, the net probability of failure of the system could be determined. Reverberation chambers will be useful in measurements in this study as they simulate operating conditions of the EUT inside a cavity and as the EUT is exposed in all directions to the electromagnetic field, the uncertainty is also reduced. The probability models can provide insight into what type of testing is required to assure worst case testing with reasonable accuracy.

1. 7 Organization of the thesis

The tasks are broken down into multiple subtasks and a procedure is developed in terms of subtasks. The final outcome of this research is to find a probability of failure of a system due to electromagnetic interference while operating in a given electromagnetic

environment. In order to calculate the probability, the electromagnetic environment in which the system operates needs to be understood/captured/analyzed. What kind of data is required to capture this EME quickly and efficiently? Given the EME, how does the system react to the EME in which it is operating? Finally, from all these data, the probability that the system will fail given a threshold has been crossed can be calculated. The step by step procedure in setting up the problem is enumerated below.

1. How to characterize the electromagnetic environment (EME) of a work space using standard frequency domain and time domain approaches? What will be advantages and disadvantages of these methods? What other parameters of the work space can be determined from the collected data.

2. What are independent samples and why are they important while performing a measurement and what do they say about EME? What is the effect of loading on independent samples? Is there a way to increase the number of independent samples by using a second tuner?

3. How could we apply the lessons learnt from 1 and 2 for a practical problem of current coupling on to a wire located inside a cavity of known dimensions and what probabilistic models could be developed to assess the probability of threat for an arbitrary case? These results will also be supported with simulations where applicable.

4. Can the failure mechanisms due to EMI/C be classified into subsets and failure models developed for each subset? If a failure model could be established, appropriate test methods can be chosen to ensure a better test while saving resources (money and time!).

These tasks will be explained in separate chapters with each chapter clearly summarizing the knowledge gained and limitations understood at the end of each chapter.

Chapter 2

2.0 ASSESSING THE ELECTROMAGNETIC ENVIRONMENT

Measurement of *Q* and Reverberation distance (A Method to Determine the Dominance of Direct or Scattered Path)

When dealing with chambers or enclosed spaces, the quality factor, '*Q*' which can be simply defined as the energy storing/dissipating capacity is of importance because it defines how much energy could be available that could potentially interact with the operating electronics in that cavity. When the *Q* is high, the space is reverberant leading to a significant amount of scattered path energy than the direct component. When the *Q* is low, the loss that is associated with the space such as loss through walls, apertures, seams, etc are larger, resulting in poor reflections. Hence the direct path energy is dominant over the scattered path energy. Classifying the problem into low, medium and high *Q* spaces helps in the determination of the electromagnetic environment in that space. There needs to be an efficient way to calculate the *Q* of the space and thereby determining the dominance of the scattered or direct path energy. This chapter will explore ways to determine *Q* of a controllable environment (such as reverberation chambers) both via frequency and time domain techniques and also examine the dominance of direct and scattered path via simple measurements. With the knowledge

gained from a controllable environment, on the determination of *Q* and reverberation distance, the procedures can be extended to simple spaces.

With the advent and abundance of wireless devices and the confined spaces in which they are installed, the exposure dominance of the direct path and the scattered path needs to be studied. When there is a line of sight between the transmitter and the receiver, the direct path seems to dominate and the received power varies as $1/r^2$.

Aircraft cavities, metal rooms and below deck environments are considered to be highly reverberant spaces where determination of shielding effectiveness (defined as the ratio of field strength without the shield to field strength with the shield) is important. The field measured at any point inside these cavities will be a sum of some direct path (mostly line of sight) from some transmitter and multipath (due to the reflection of electromagnetic energy from the metal walls). At some locations, the multipath effects can be higher than the direct path effects hence the dominance of the direct path compared to the multipath needs to be explored. In order to qualify the placement of any wireless devices inside such reverberant cavities the distance at which the multipath effects seem to dominate needs to be found. In this chapter an attempt has been made to compute the reverberation distance for such a scenario and the results have been compared and validated in frequency and time domain.

It was suggested in [6] that the distance between the transmitter and the EUT (in our case the receiver antenna) can be varied to simulate different Rician environments (*K* factors).

The same idea has been explored in this chapter to obtain different *K* values and we go further to calculate the distance at which the dominant and scattered path will carry equal power.

2. 1 Theoretical estimation of K

The Rician *K* factor can be defined as the ratio of the direct path component to the scattered path component [6]. *K* can be expressed as a function of the chamber and antenna characteristics. The expressions for *K* are given below. The detailed calculation of expressing *K* in terms of *Q* is shown in [6].

$$K = \frac{\text{Direct component power}}{\text{Scattered component power}}$$

$$K = \frac{3}{2}\frac{V}{\lambda Q}\frac{D}{r^2} \qquad \textbf{(2.1)}$$

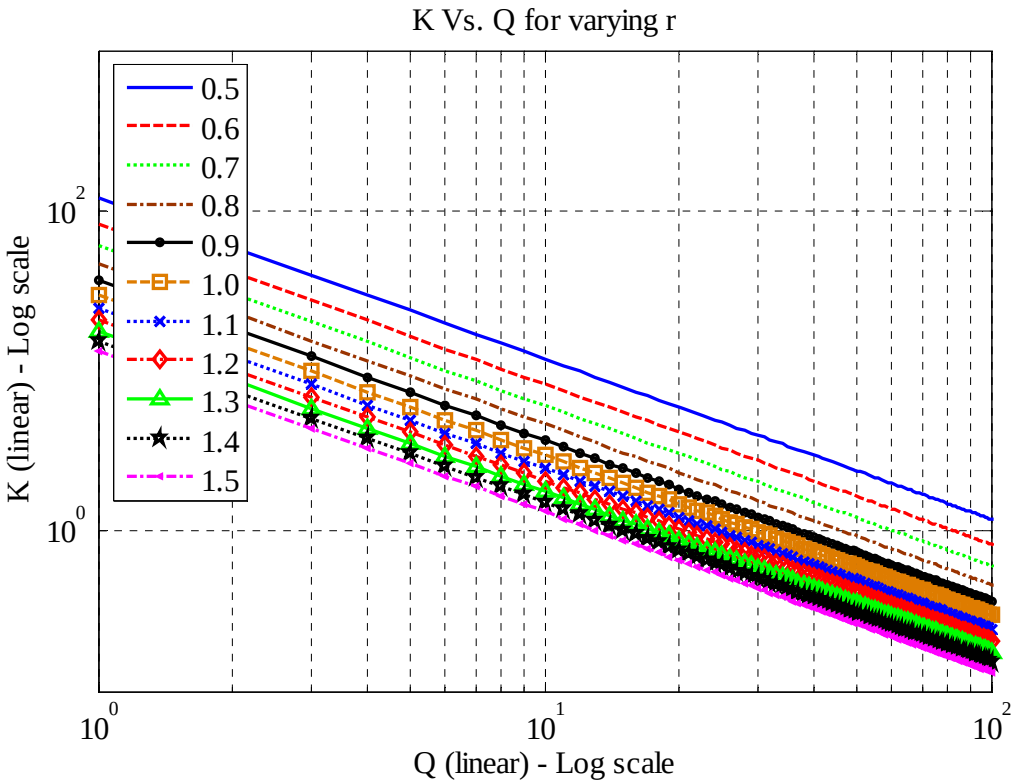

Figure 2. 1 Estimation of K for different Q values at different distances of separation

From eqn. (2.1), we can see that the *K* factor can be controlled by varying the directivity of the antenna, or the volume (hence the *Q*) of the room and also by varying the distance between the transmitter and the receiver antenna. To understand the effects, a theoretical estimation of *K* for multiple separation distances is calculated using eqn. (2.1) for varying *Q*'s (1 to 100 in steps of 10) of the same volume (1.98m^3) and frequency of operation (2 GHz) and for antenna directivity, D=1.5 (dipole directivity). The results are plotted in Figure 2.1. The point where the *K* equals 1 is of importance as it can be looked on as the point where the direct path and multipath powers are considered to be equal [7]. From Figure 2.1, the reverberation distance can be found if the *Q* of the volume can be measured. The line for a separation distance of 0.5m, crosses *K*=1 for a much larger *Q* than the line for separation distance of 1.5m. As expected, when the *Q* is high, even for

small separation distances between the antennas, reverberation starts and the multipath power starts to dominate and when the *Q* is low, the direct path dominates for longer distances. The $1/r^2$ dependence of *K* can also be seen from the exponential decay trend of the curves represented as straight lines in Figure 2.1 as it is a Log-Log plot.

The problems with theoretical estimation of the *K* factor are the unknowns in eqn. (2.1). The directivity varies as a function of frequency making it harder to have a good estimation. The variation in the estimation of the *Q* of the chamber can be as high as 3dB for different points of measurement [4]. Hence all these factors make it difficult to calculate *K* values from eqn. (2.1). The best possible estimation of the *K* values or the reverberation distance can be obtained from measurements. Measurements will be performed in both frequency and time domain to calculate *K*, *Q* and eventually the reverberation distance. Validation of these results will be obtained by comparing one against the other.

2. 2 Frequency domain

In the frequency domain analysis, the signals are analyzed with respect to frequency and not as a function of time. By fixing the frequency, the *Q* of the room (in our case an RC) is also fixed as *Q* is also a function of frequency. Thereby for varying distances of separation between the two antennas, the EME can be determined. The Rician *K* factor in terms of scattering parameters (S parameters) following [6] is given by

$$K = \frac{\left(\left|\left\langle S_{21}\right\rangle\right|\right)^2}{\left\langle\left|S_{21} - \left\langle S_{21}\right\rangle\right|^2\right\rangle} \quad \textbf{(2.2)}$$

K includes ensemble averages as presented in eqn. (2.2) which are denoted by the angled brackets. The ensemble averages are calculated as the average value over the entire sweep of the tuner. The numerator is related to the direct component and the denominator, the mean normalized S_{21}, is related to the multipath component. Thus the Rician *K* factor can be measured as the ratio of the direct to the multipath component. Scatter plots of real and imaginary parts of S_{21} reveal that the "cluster radius" is determined by σ_R and the distance of the "cluster centroid" is d_R from origin [6] (not shown). When the ratio of the numerator to the denominator is small, then the multipath dominates and so S_{21} will be normally distributed.

Because reverberation chamber test methods have been well established and also more controllable, measurements were performed in a reverberation chamber first and then the analysis will be performed for other not so predictable environments.

2. 2. 1 Experimental procedure

For a *Q* measurement to be performed in a reverberation chamber, any direct coupling between transmit and receive antenna has to be eliminated as direct coupling skews the statistics of the chamber. This will be true for any spaces that are reverberant. In the *Q* measurements that were performed inside the reverberation chamber, the antennas were

separated by a large distance and the transmitter is focused on a corner while the receiver antenna was facing the tuner. The polarization of transmit and receive antenna were avoided to be the same [4].

VNA in the CW (single frequency or constant wave) mode was used in the measurement process. The transmitter was connected to port 1 and the receiver was connected to port 2. Calibration was performed until the end of the cables and the antenna efficiency is assumed to be 100%. S_{21} or the transfer function of the chamber at that frequency was measured for different positions of the receiver inside the usable volume of the chamber at 1 GHz for one complete rotation of the vertical tuner. Maximum number of available data points (1601) is used in all our measurements.

The dimensions of the chamber are L – 13.2m, W – 6.15m and H – 4.95m. Though there is a vertical and the horizontal tuner, at 1 GHz the mode density (defined as the number of modes per bandwidth) is significantly high that any one of the tuners is sufficient to give good statistics. This is proven in the statistical analysis performed on the data that was captured during these measurements as shown in Figure 2.2. Autocorrelation analysis performed on the data that was captured shows that there are nearly 250 independent samples associated with the chamber with the vertical tuner operating at 1 GHz. From the mean received power, *Q* of the chamber was calculated using [4]

$$Q = \frac{16\pi^2 V}{\lambda^3} \times \frac{\langle P_r \rangle}{P_t} \qquad \textbf{(2.3)}$$

$$\text{Where, } \frac{\langle P_r \rangle}{P_t} = \left\langle \left| S_{21} \right|^2 \right\rangle$$

The Q measurement was repeated with 10 different transmit and receiver antenna positions to look at the variation of Q and K values as just a function of statistical sampling.

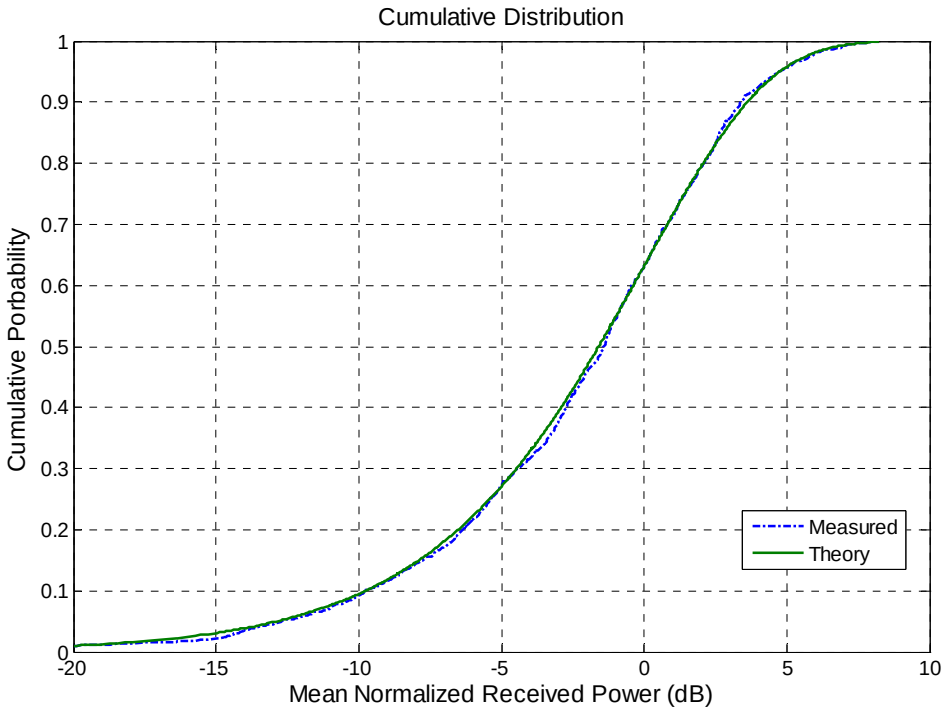

Figure 2. 2 Cumulative distribution plot for received power inside a reverberation chamber

To measure the Rician K factor, a direct line of sight component must be present else K will be close to zero [6]. This was established by locating the antennas facing one another and the polarization is maintained to be the same (co-polarized). The distance between the transmitter and the receiver was varied from 0.5 feet to 10 feet in 0.5 feet steps. As the distance between the transmitter and the receiver was increased, more of the tuner was exposed to the transmit antenna field (as the tuner is present behind the receiver antenna) hence the scattered power domination is expected to increase. The ratio of the received power to transmit power in the form of S_{21} was captured at every position of the

receiver for one complete rotation of the tuner (stirred) using the same VNA experimental setup discussed earlier. Illustrations of both the measurement setups are provided in Figures 2.3 and 2.4.

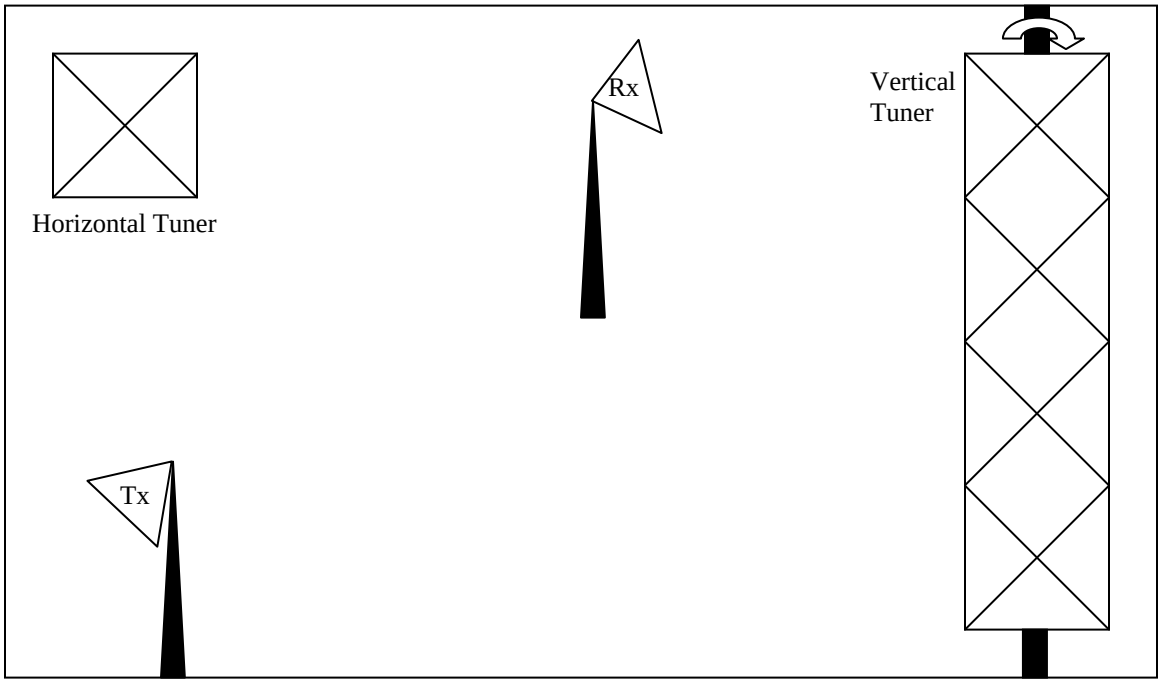

Figure 2. 3 Q measurement setup

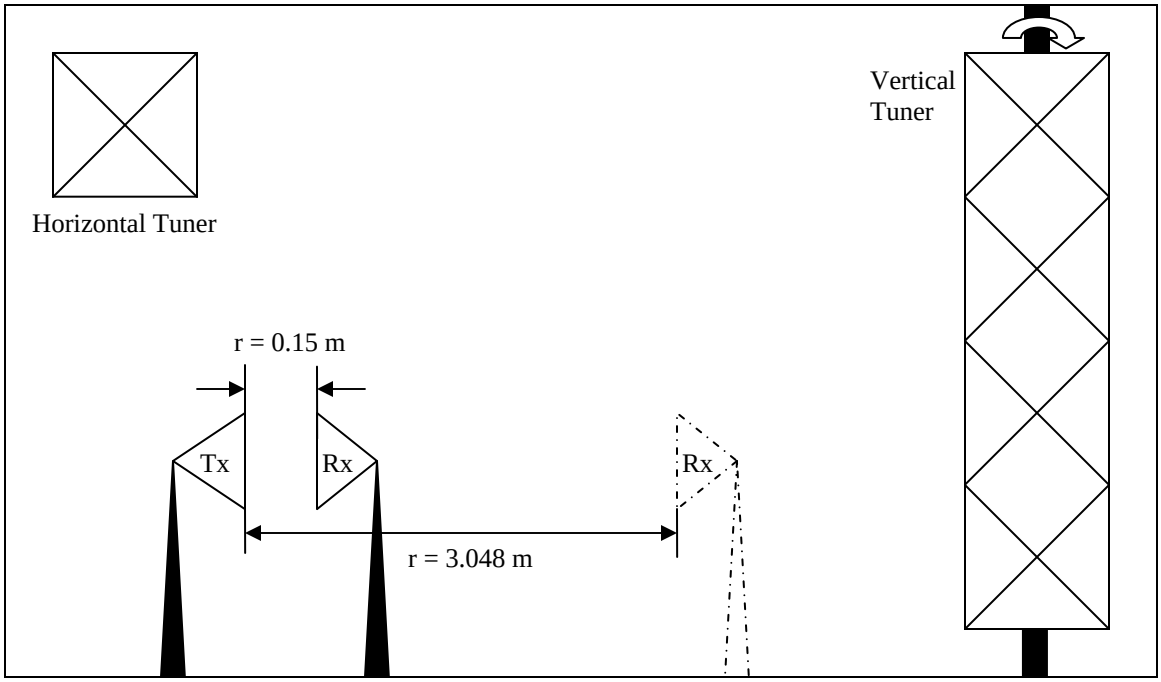

Figure 2. 4 K measurement setup

The *Q* and *K* values were calculated from the measured S parameter data using eqn. (2.3) and eqn. (2.2) respectively. When there is no direct coupling between the transmitter and the receiver antenna, *K* values are reported to be significantly less than 1. *Q* and *K* values measured for ten different receiver antenna positions inside the chamber with no direct coupling between the transmit and receiver antenna are given in Table 2.1.

Table 2. 1 Q and K values for a reverberation chamber (no direct coupling between the antennas)

Position	***Q***	***K* (from S21)**
1	38093	0.01
2	37064	0.01
3	44629	0.00
4	49280	0.10
5	43283	0.01
6	45051	0.11
7	43808	0.00
8	42585	0.04
9	42283	0.02
10	41911	0.01

In Table 2.2 *K* calculated from S_{21} data measured for different separation distances are reported (Direct LOS component present for this set of measured data). Referring to Table 2.2, it can be noted that the *K* values increase with decreasing separation distance. The distance at which the *K* values start to be less than 1 can be reported as the reverberation distance. As per the definition the reverberation distance is the point at which the direct path and scattered path power would be equal [7]. For this chamber/antenna settings and frequency of operation, the reverb distance is estimated to be about 2.5 feet. The calculated reverberation distance will be verified against the time domain measurements discussed in the next section. *Q* values are not reported because eqn. (2.3) does not hold true when there is a direct coupling between the antennas.

Table 2. 2 K values for a reverberation chamber (direct coupling between the antennas)

r in feet	r in m	*K* (from S21)
0.5	0.15	32.46
1	0.30	10.47
1.5	0.46	4.54
2	0.61	1.89
2.5	0.76	0.43
3	0.91	0.40
3.5	1.07	1.32
4	1.22	1.28
4.5	1.37	0.83
5	1.52	0.90
5.5	1.68	0.68
6	1.83	0.38
6.5	1.98	0.41
7	2.13	0.44
7.5	2.29	0.34
8	2.44	0.58
8.5	2.59	0.22
9	2.74	0.16
9.5	2.90	0.06
10	3.05	0.31

2. 2 Time domain

In the time domain analysis, the signals are analyzed with respect to time. In the reverberation chamber, generally the excitation pulse required in time domain measurement is short compared to the chamber time constant [8]. This was made possible by using a VNA with time domain option and controlling the bandwidth of the input signal. The Fourier transform is performed on the signal from the receiver antenna by the VNA thereby transforming the frequency domain data to time domain. In our measurements, the bandwidth was chosen to be 200 MHz around 1GHz. Given the size of the chamber, 200 MHz bandwidth is sufficient in producing a statistically equivalent field configuration inside the chamber compared to CW operation of the chamber combined with tuner rotation.

The reverberant environment can be separated into a reverberant and pre reverberant phase. The pre-reverberant phase transforms into the reverberant phase as the number of wavefronts that has many polarizations and direction of propagation increases from a single plane or spherical wavefront [8]. As the pre-reverberant phase transforms into the reverberant phase, the field starts to decrease exponentially. During the single pulse excitation, both the phases are separated in time. The pre-reverberant phase is short lived in a highly reverberant environment and the pre-reverberant phase die out before transforming to the reverberant phase in a poorly reverberant environment. In the CW mode of excitation, both the phases coexist. The time domain technique has its advantages over the frequency domain technique as the contamination of the reverberant field data by any direct path or pre reverberant field components can be eliminated. The

exponential decay of the reverberant field can be used to estimate the *Q* of that space. The pre-reverberant phase is very interesting in understanding the mode formation and mode distribution inside the space at the moment of energy being coupled into the space which is beyond the scope of this effort hence not studied here.

Figures 2.5 and 2.6 are the time domain response measured between two antennas that do not have a direct line of sight coupling. The measurements were performed in a reverberation chamber. The thin lines are measurements at a fixed tuner position, for multiple tuner positions. Measurements were made at 50 such tuner positions (equiangular distributed around one rotation of the tuner). The thicker line is the ensemble average of all the 50 fixed tuner point measurements. All the 50 tuner positions used in the measurements are considered to be independent. From the reverberation chamber theory, when the number of measured samples is far less than the total number of available independent samples (50 << 250 in our case), all the measured samples are considered to be independent. The measurements were performed for two different time windows. The time windows represents the time for which the power decay in the chamber has been observed. The smaller time window is useful in studying the pre-reverberant phase of the field while the larger time window is useful in studying the reverberant phase. As maximum number of data points was captured in every measurement (1601 points), the resolution differs for the time windows. When the time window is short (~500 ns), the resolution is higher and when the time window is large (~ 8us), the resolution is low.

Figure 2.5 with the smaller time window shows the time delay of the energy to reach the receiver antenna and a maximum there after indicating the formation of the first or dominant mode inside the chamber. The under moded characteristics (direct coupling + unstirred energy) of the chamber before the establishment of reverberant fields can be seen in the smaller time window.

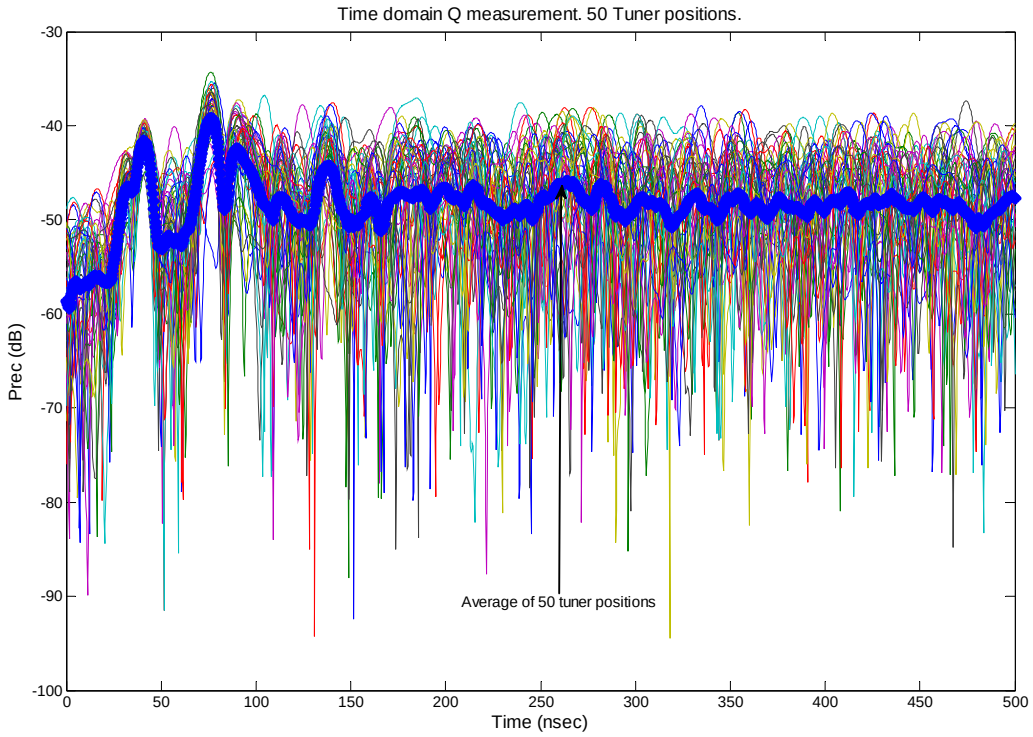

Figure 2. 5 Time domain response of received power (no direct coupling between antennas)

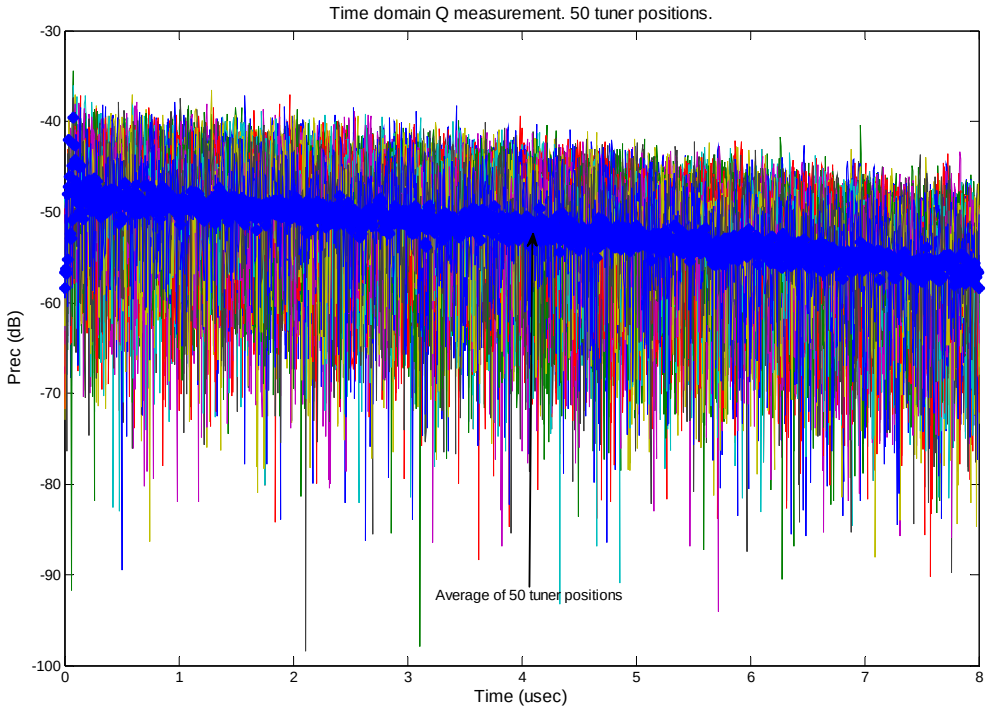

Figure 2. 6 Time domain response of received power (no direct coupling between antennas)

The fixed tuner position measurements at first (~ 35 nsec) seem to follow each other consistently though not exactly over lapping but later, they deviate from each other indicating the transformation to a reverberant phase when the wavefronts have different polarizations and direction of propagation and arriving at the receiver end at different times. This was an interesting observation which will help us understand the under moded regime of a chamber and needs further exploration.

In Figure 2.6, with the time window being larger, though the fixed tuner position measurements are noisy and deviate from each other significantly, suggest an exponential decay of the field. By fitting a straight line to the ensemble average, the slope of the exponential curve can be found. From the slope, the chamber time constant or the time

required for the signal to decay to 37% of the maximum (1/e time) can be estimated. The slope for this set of measurements was calculated to be 1.4 dB/usec.

The chamber time constant can be calculated as below following [8].

log(1/e)= -0.43429 = 4.3429 dB

Slope = 1.4 dB/usec

$$\text{Reverberation time} = \tau = \frac{4.3429}{\text{Slope}} \qquad \textbf{(2.4)}$$

$\tau = 3.1$ usec

Q of the chamber can be calculated from the chamber time constant, $Q = \tau \times 2\pi f$, yielding a Q of 42.9 dB [4].

The same procedure was repeated for calculating the time response of the chamber when the antennas are facing each other (strong line of sight expected) at different separation distances. Data was collected for 50 different tuner positions as mentioned before and the ensemble average was calculated from the fixed tuner position measurements.

Figures 2.7 and 2.8 show the time response for a time window of 500 nsec for separation distances of 1ft and 10 ft respectively. As the distance between the transmitter and the receiver increases, there is a larger delay for the energy to reach the receiver end (delay in direct coupling). The slope of the ensemble curves (for all separation distances) from data for a time window of 8us were calculated in a similar fashion and the slope were found to be 1.1 dB/usec. The reverberation time was calculated to be 3.9 usec yielding a Q of 43.9 dB.

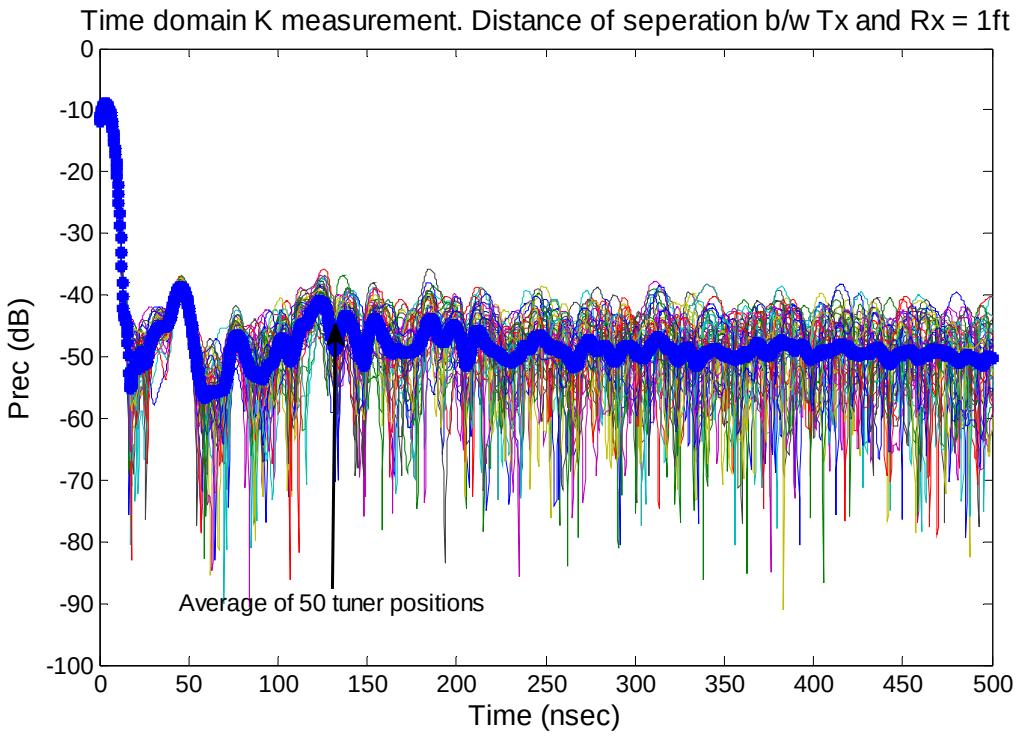

Figure 2. 7 Time domain response of received power (direct coupling between antennas; separation = 1 ft)

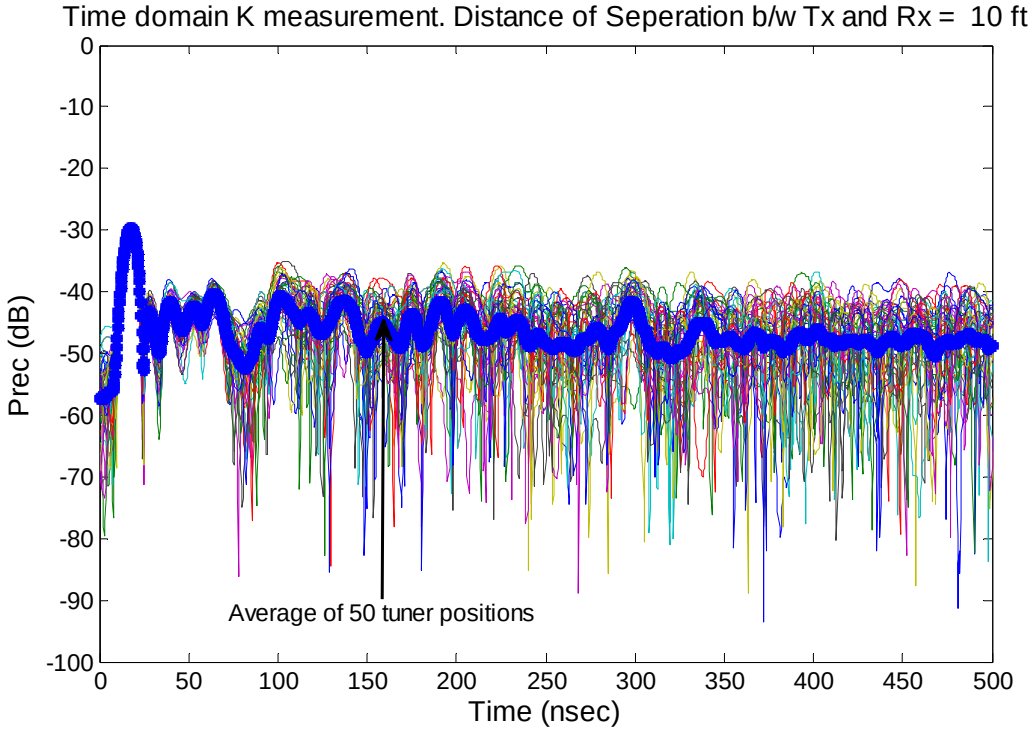

Figure 2. 8 Time domain response of received power (direct coupling between antennas; separation = 10 ft)

2. 2. 1 Calculation of reverb distance from time domain data

The reverberation time was calculated to be 3.9 usec from the slope decay rate of 1.1 dB/usec. The average absorption coefficient can be found using the reverberation time in equation below [7].

$$\text{Absorption coefficient} = \eta = \frac{4V}{c\tau A} \quad \textbf{(2.5)}$$

Where, V is the volume and A is the surface area. The volume and surface area of the cavity used in this measurement were calculated to be 401.84 m^3 and 353.93 m^2 respectively resulting in an absorption coefficient of 0.004. The absorption coefficient can be used to calculate the reverberation distance [7]:

$$\text{Reverberation distance} = r_d = \frac{1}{2}\sqrt{D_1 D_2 \eta A} \quad \textbf{(2.6)}$$

D_1 and D_2 are the directivities of the two antennas (transmitter and the receiver) used. Due to the reflective nature of a reverberation chamber and multipath propagation pattern, the directivities of any device or antenna placed inside the chamber are washed away. Directivity being an intrinsic property of the device or the antenna in use, is not lost in a reverberation chamber but the effects of it is less pronounced and hence considered to be washed away ($D_1 = D_2 = 1$). Substituting the directivity values, the reverberation distance is calculated to be 0.6m or 1.95 ft. the reverberation distance calculated from the frequency domain approach is around 2ft. The calculation is shown below.

Inside a reverberation chamber D1 and D2 are 1.

Hence $r_d = \frac{1}{2}\sqrt{\eta A}$

$r_d = 0.6m = 1.95\,ft$

Reverb distance calculated for two horn antennas inside the chamber at 1GHz using time domain is around 2ft. Though the reverb distance was comparable to frequency domain calculation of reverberation distance (2.5 ft), the *Q* that is obtained in time domain was at least 3dB lower than the frequency domain *Q* at that frequency. The disagreement raises the question of which test data to believe? Though time domain data is over a number of frequencies, the *Q* variation with respect to frequencies might not be as much as 3dB. Also the bandwidth over which this test was performed was small hence the difference in *Q* should be minimal amongst the frequencies. More measurements were performed in frequency and time domain at many frequencies and varying bandwidths to answer some of the questions that were raised here. These measurements and results will be discussed later.

2.3 Insertion loss and its implication to reverberation distance

Insertion loss in a reverberation chamber is defined as the ratio of maximum power received to power transmitted. As the maximum power received is a function of number of measured samples, the mean power received is used which would be a better estimate (because variation in the mean from run to run is smaller than the variation in maxima from run to run) to calculate insertion loss.

$$IL = \frac{\langle P_r \rangle}{P_t} = \langle |S_{21}|^2 \rangle \quad \textbf{(2.7)}$$

From the measured samples and the analysis of independent samples, the maximum can be predicted. Received power follows a chi square or exponential distribution in a multipath environment [4]. From the number of independent samples, an estimate for maximum can be established for that distribution and the maximum will lie within the uncertainty (1 or 2 standard deviations). Hence the maximum to mean ratio number can be added to the mean received power to calculate the insertion loss. Here, mean power received will be used in all calculations.

The insertion loss measurements were performed for 2 chamber configurations, one with the unloaded chamber and other with 5 dB of loading. The mean received power will vary for the two different chamber configurations hence the insertion loss will also vary. Data were collected using the same setups described earlier. When the antennas are not pointing at each other, ten different antenna positions are used to find an "average" insertion loss (this is the insertion loss we expect if we do not have any direct coupling and the multipath power dominates). The antennas are pointed at each other and the separation distance is varied in 0.5 feet steps from 0.5 to 10 feet and the insertion loss is calculated at every step from the ratio mean power received data to the input power ($<S_{21}>$).

From Figure 2.9 it can be seen that the insertion loss decreases with increase in the separation distance. The slope is larger for smaller distances and later it traces close to the average insertion loss. When the chamber is loaded, the surface area is reduced resulting

in fewer reflections and subsequent reduction in *Q* and thus directs path dominates for a longer time which is reflected in our measurements. Measurements performed at 300 MHz (not shown here) with log periodic antennas follow the same pattern.

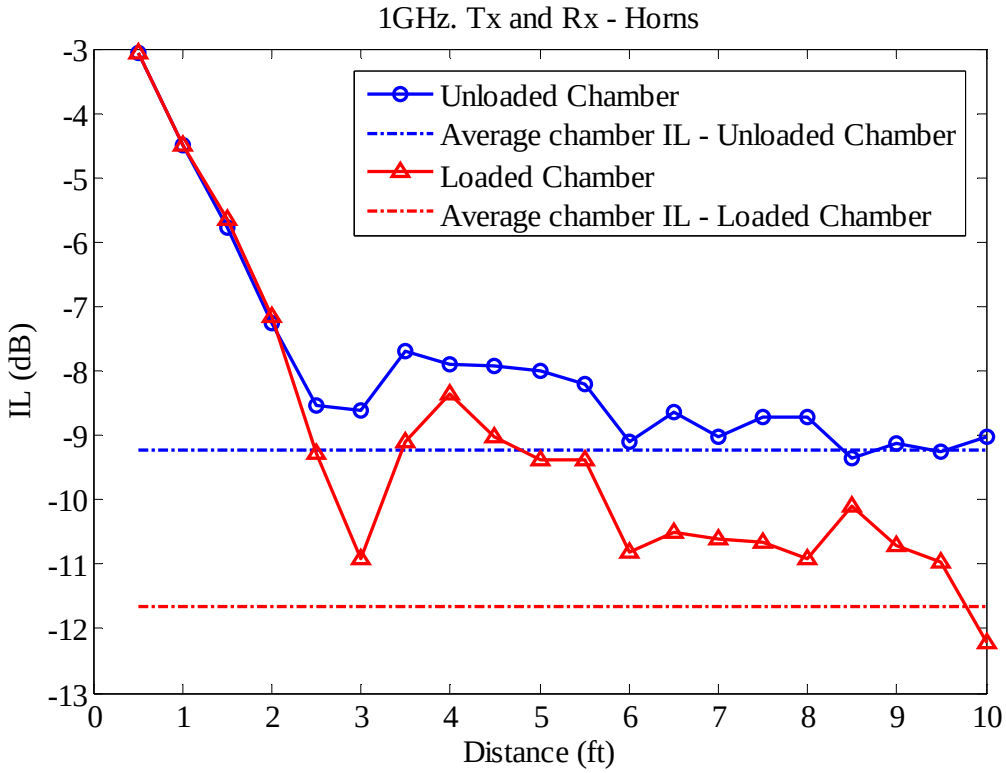

Figure 2. 9 Insertion loss for empty and loaded chamber at 1 GHz

Comparison of the insertion loss of the empty chamber with *K* measured for varying distances and empty chamber shows, at the distance where *K* equals 1 (reverberation distance), the slope of the insertion loss changes and experiences a more average behavior after that distance [Ref: Figure 2.10] which again ascertains the fact that the reverberation distance calculated has more significance. The multipath power dominates the direct path, reflected by *K* values less than 1 and the change in insertion loss slope to follow a more average behavior happens around the same distance.

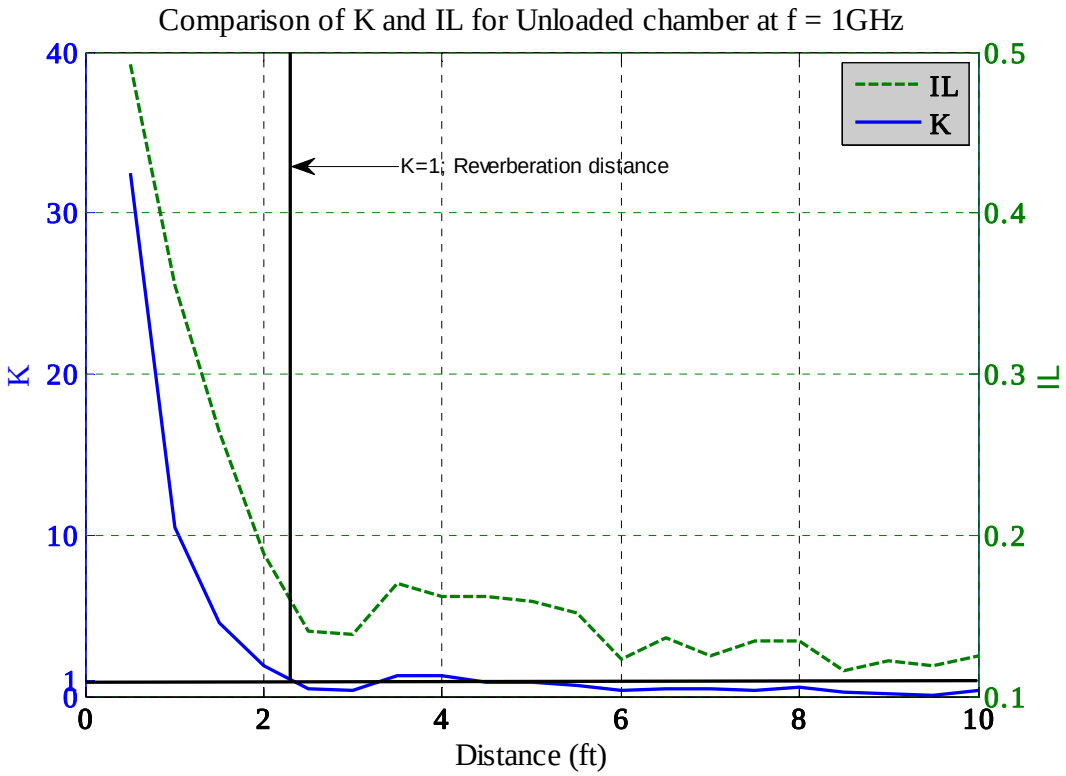

Figure 2. 10 Plot of K and Insertion loss for empty chamber at 1 GHz

The quest behind this exercise was to quickly determine the EME of the space with quick set of measurements which will then enable a test engineer to make a meaningful estimate about assessing what type of testing must be done on the equipments that will operate in such environment. Tests were performed in a reverberation chamber in frequency domain at 1 GHz and the same tests were performed in time domain for comparison and also to establish the advantage of one method over other if there is any.

Several parameters about the environment were calculated in frequency domain. The two that were of importance is the *Q* of the cavity and the reverberation distance, i.e. the distance at which the direct path and multipath powers are equal. When compared to the

results obtained from time domain, the reverberation distances obtained from both were comparable while the *Q* was at least 3dB different. The time domain data seems to under predict the *Q* compared to frequency domain. This discrepancy needs to be resolved before concluding the accuracy and efficiency of one method over the other.

The advantage of a time domain method in the estimation of reverberation distance is that the direct path components can be windowed out the multipath effects can be used in determining the 'tau' hence the absorption coefficient and reverberation distance. Moving the antennas thereby increasing the separation distance between them like in frequency domain can be eliminated in time domain resulting in the reduction of test time.

The analysis of estimation of *Q* was extended to a small room and a hallway to see the if difference between the time domain and frequency domain *Q* persists in the not so reverberant environments. As the room and the hallway do not have a stirrer to stir the fields efficiently, source stirring was used in data collection. Source stirring indicates that the source antenna and the receiver antenna are moved in the space and received power samples are collected as a function of position of the Tx and the Rx antennas [10 11].

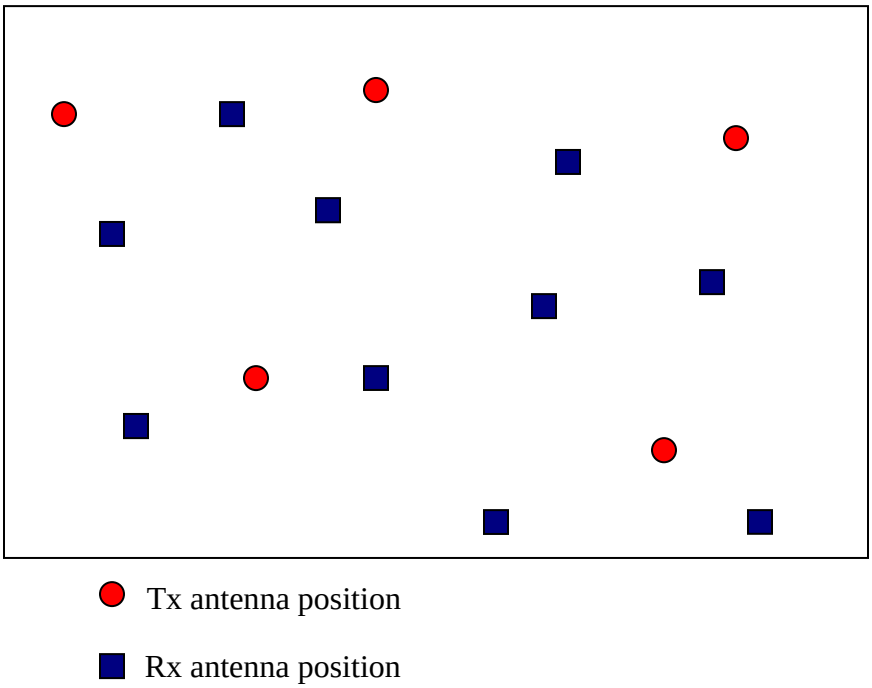

Figure 2. 11 Illustration of the source stirring measurement points in a room

50 total measurement points were chosen in the space. Spatial correlation was considered while choosing every measurement point hence every point is at least half a wavelength from the previous one [12]. For every Tx antenna position, 10 different Rx antenna positions were chosen for measurement. This was repeated for 5 different Tx antenna positions leading to 50 measurement points on the whole as shown in Figure 2.11. The chosen 50 positions are arbitrary, to do a better analysis, more positions may be needed. 50 positions were chosen mainly depending on the time that was available for data collection. At any measurement point, direct coupling between the Tx and Rx antennas was avoided to eliminate the bias in the statistics.

Both time domain and frequency domain measurements were performed in the small room and the hallway. Pictures of the Hallway and small room are shown in Figure 2.12 along with their dimensions.

Hallway –
17.6 x 1.9 x 2.9 (m)

Small room –
5.5 x 2.1 x 2.7 (m)

Figure 2. 12 Pictures of the hallway and the small room

2. 4 Measurements in Hallway

2. 4. 1 Frequency domain

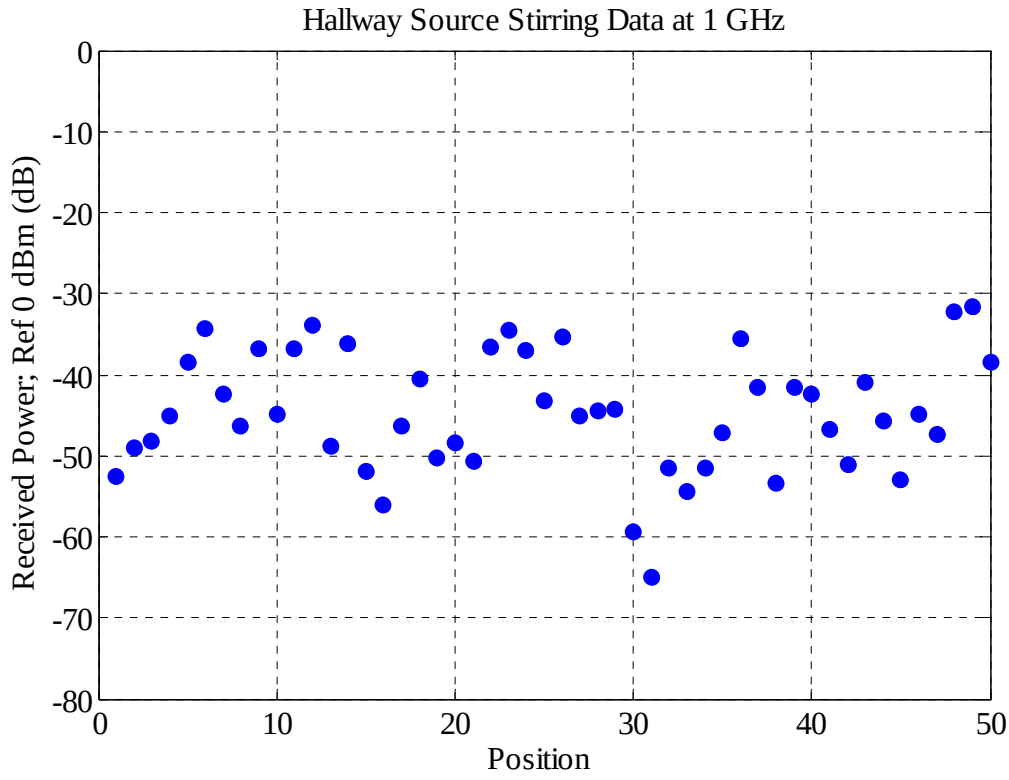

Figure 2. 13 Received power as a function of position (source stirring) in the hallway at 1 GHz

The received power as a function of position of the antenna is shown in Figure 2.13. The stirring ratio which the ratio of the max to the min turns out to be about 30 dB. It has been suggested that for good reverberation inside a cavity, the stirring ratio should be at least 20 dB [4]. Hence this space would qualify for the application of RC statistics on the data collected.

Following the standard procedure of analyzing this data, the *Q* of the space was found to be about 18 dB. The cumulative distribution function (CDF) comparison between the

measured data and theory is marginal (not shown). The reason for the marginal agreement is suspected to be the poor reverberant nature of the space due to the associated losses and insufficient amount of data points.

2. 4. 2 Time domain

For the same antenna positions at which frequency domain data was collected, time domain measurements were also performed. A bandwidth of 200MHz was chosen around the center frequency of 1GHz for this measurement. From the 50 different frequency sweep data, an average of the sweep was calculated and used for analysis of *Q* and reverberation distance. Two different time windows were also observed to look at the early and later effects of cavity buildup.

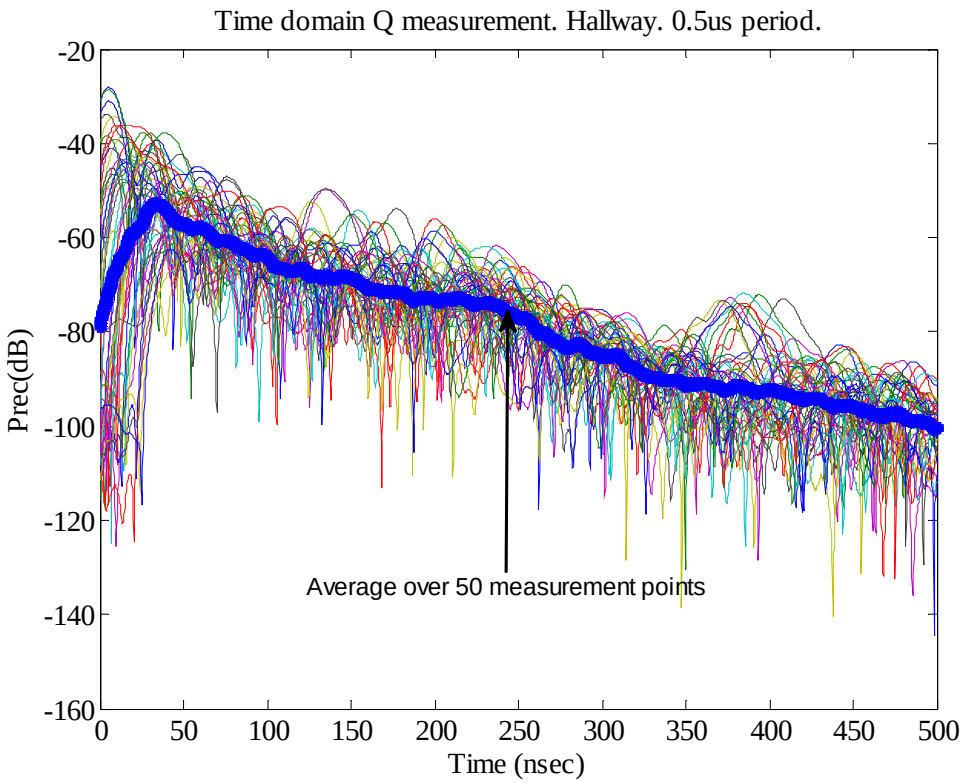

Figure 2. 14 Received power as a function of time in the hallway; smaller time window

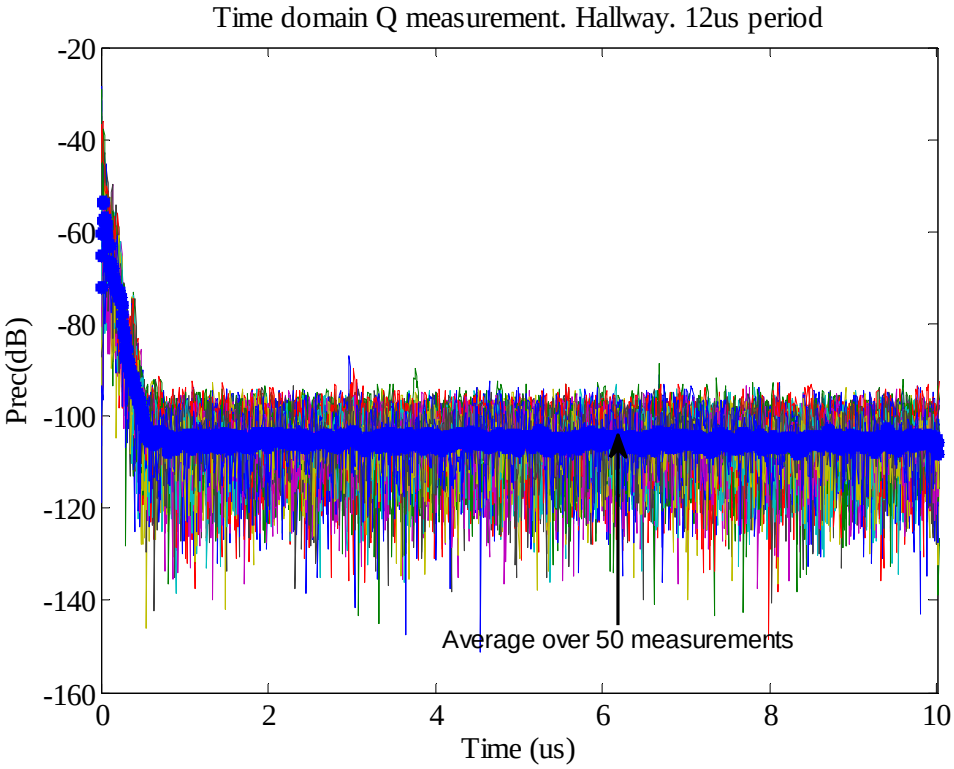

Figure 2. 15 Received power as a function of time in the hallway; larger time window

From Figures 2.14 and 2.15 it can be seen that the losses associated with the space is large hence beyond 0.5us most of the measured samples are lower than the noise floor. Fitting a line to the mean curve, the slope was obtained to be 92 dB/usec. Following the same procedure as before, *Q* was obtained to be 24.7 dB and reverberation distance = 2.6 m or 8.6 ft. In this set of measurements, time domain *Q* (decay *Q*) is higher than the frequency domain estimate.

2. 5 Measurements in Small room

2. 5. 1 Frequency domain

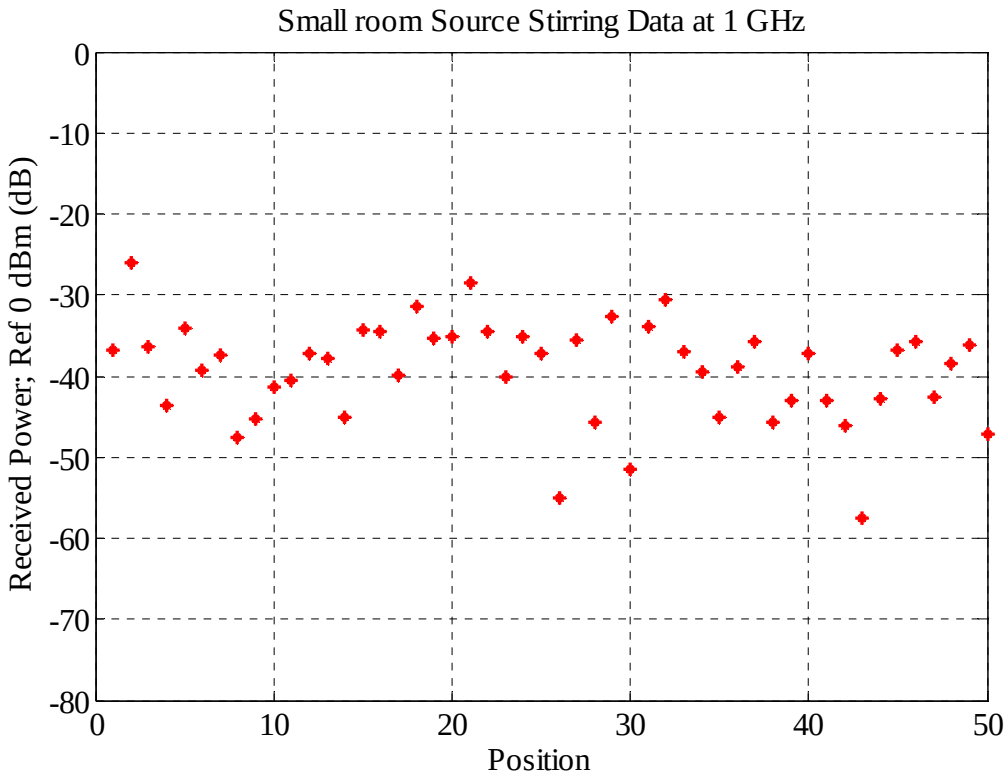

Figure 2. 16 Received power as a function of position (source stirring) in the small room at 1 GHz

The received power as a function of position of the antenna for the small room is shown Figure 2.16. The stirring ratio which the ratio of the max to the min turns out to be about 30 dB. By the 20 dB criterion explained before, this space would qualify for the application of RC statistics on the data collected. Following the standard procedure of analyzing this data, the *Q* of the space was found to be about 17 dB. The CDF comparison between the measured data and theory is also marginal (not shown) as the hallway data previously mentioned.

2. 5. 2 Time domain

For the same antenna positions used in the frequency domain measurements, time domain measurements were also performed. A bandwidth of 200MHz was chosen around the center frequency of 1GHz for this measurement. From the 50 different frequency sweep data, an average of the sweep was calculated and used for analysis of *Q* and reverberation distance. Two different time windows were also observed to look at the early and later effects of cavity buildup.

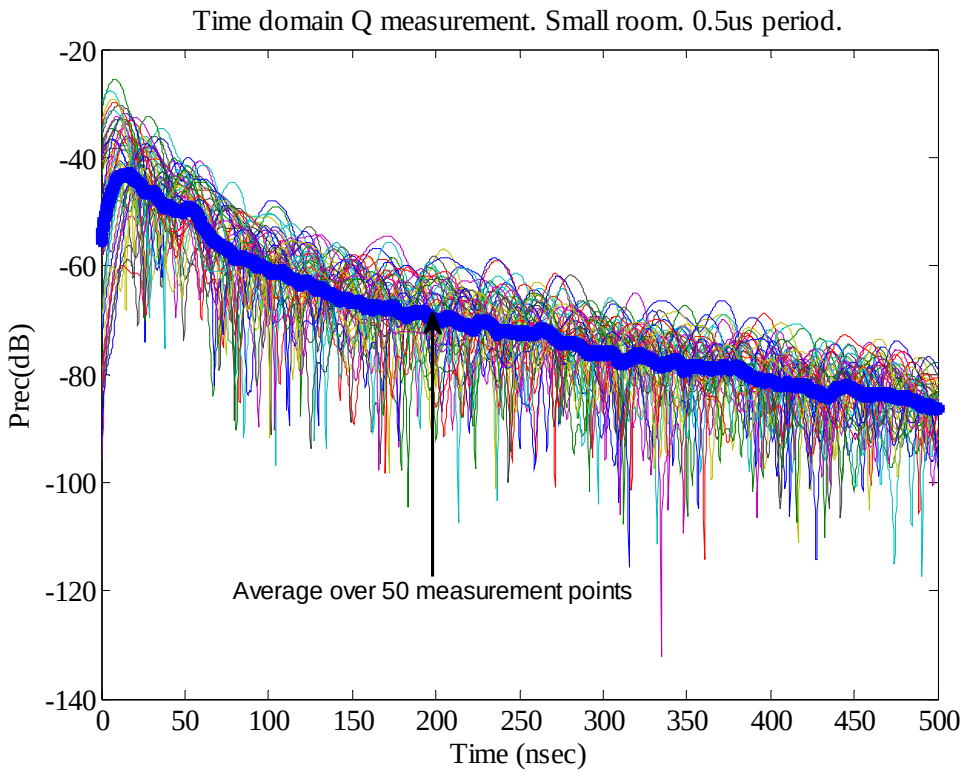

Figure 2. 17 Received power as a function of time in the small room; smaller time window

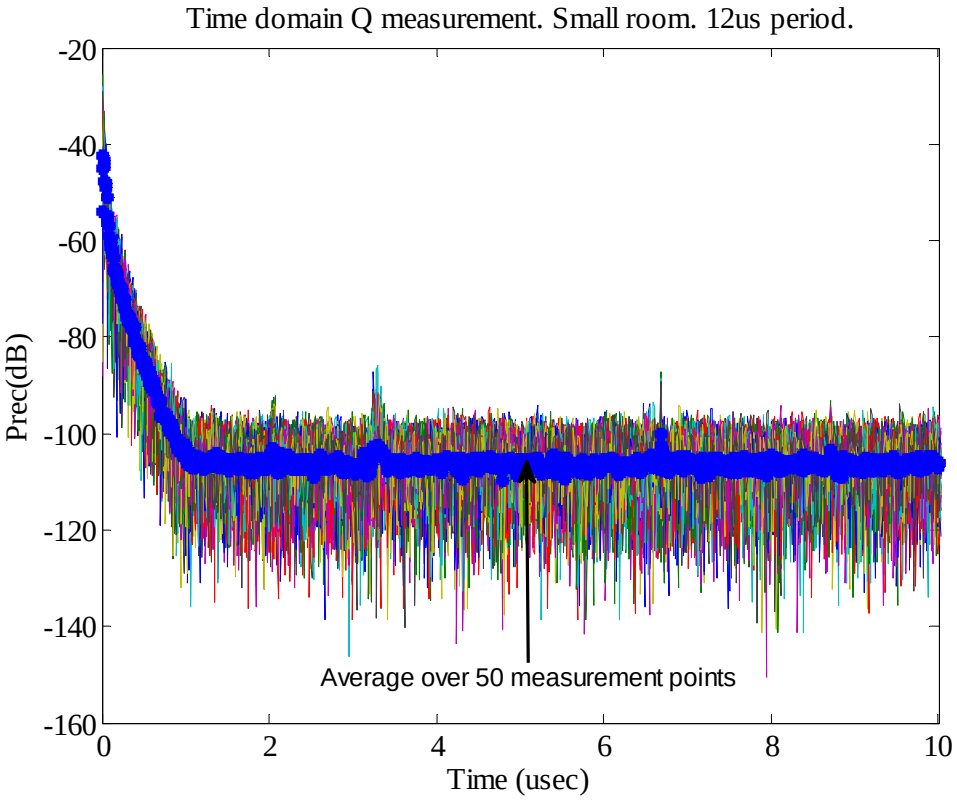

Figure 2. 18 Received power as a function of time in the small room; larger time window

As in the hallway, in the small room losses associated with the space is large hence beyond 0.5us most of the measured samples are lower than the noise floor as can be seen in Figures 2.17 and 2.18. Fitting a line to the mean curve, the slope was obtained to be 77 dB/usec. Following the same procedure as before, *Q* was obtained to be 25.5 dB and reverberation distance = 1.5m or 4.75 ft. In this set of measurements, time domain again predicts a higher *Q*.

Comparing the measurements from hallway and small room, the reverb distance for the small room is smaller than the hallway. The small room is about 3 times smaller than the hallway in both volume and surface area so we expect the multipath to take over at a shorter distance than the hallway and that is reflected in the reverb distance calculation.

A comparison of the time domain measurements for the room and hallway are presented in Figure 2.19. The decay profile of both the room and the hallway can be clearly differentiated along with different times to peak power. By comparing the amplitude of peak received power in the room to that of the hallway, it appears that the *Q* of the room is higher than that of the hallway. The time to peak power for the room is also shorter than that of the hallway which may suggest that the losses associated with the room are less than the hallway leading to a higher *Q* value for the room compared to the hallway.

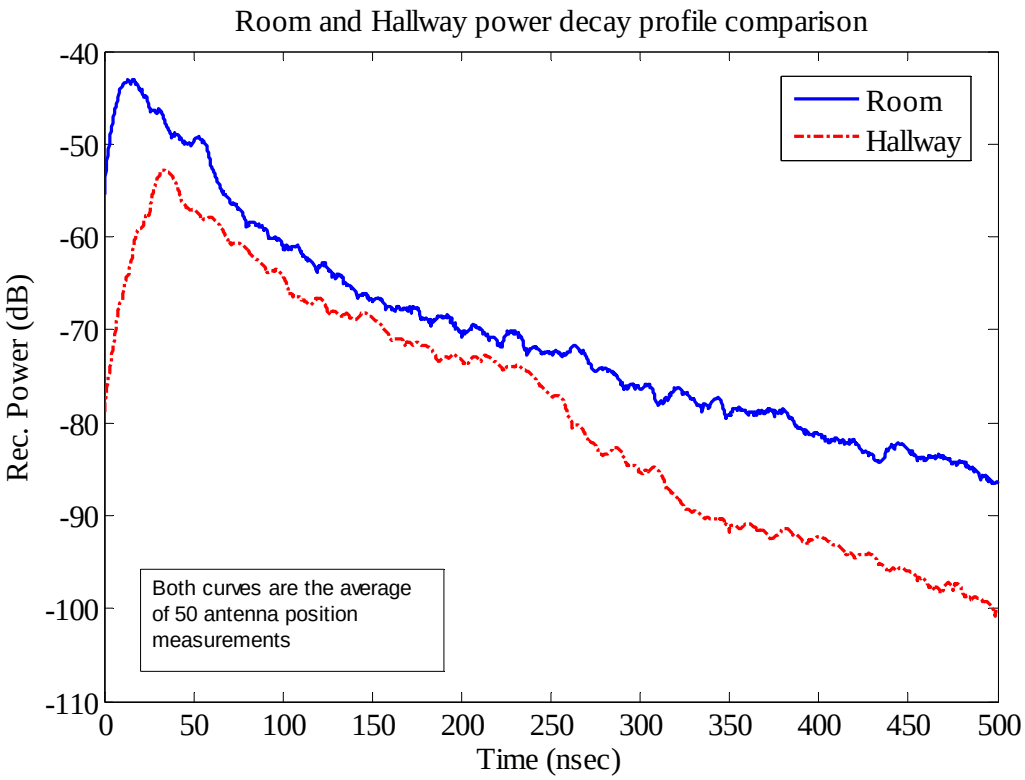

Figure 2. 19 Power decay profile of the hallway and small room at 1 GHz

2. 6 Comparison of frequency and time domain Q measurements from literature

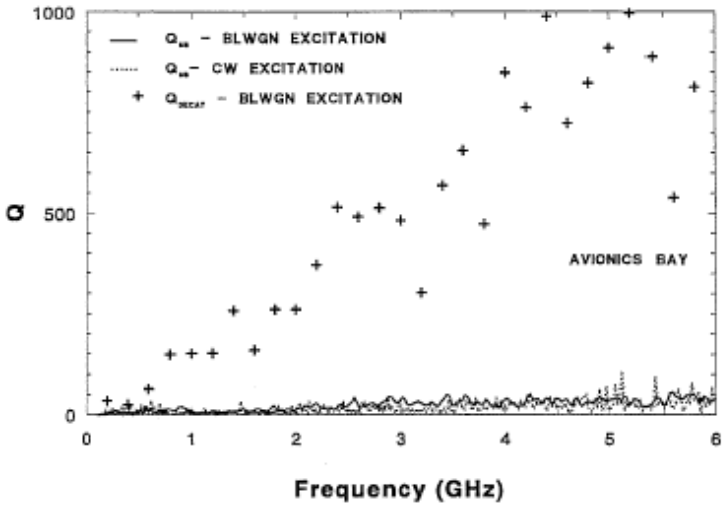

Figure 2. 20 Avionics bay Quality factor comparisons (Figure 4-37. NSWCDD/TR-97/84 [13])

Figures 2.20 and 2.21 are the measured *Q* values in the avionics bay and the passenger cabin of an aircraft. As the aircraft cabin is metallic and reflective, its operation can be considered to be similar to that of a reverberation chamber making it potentially feasible to use reverberation chamber methods and statistics for analysis.

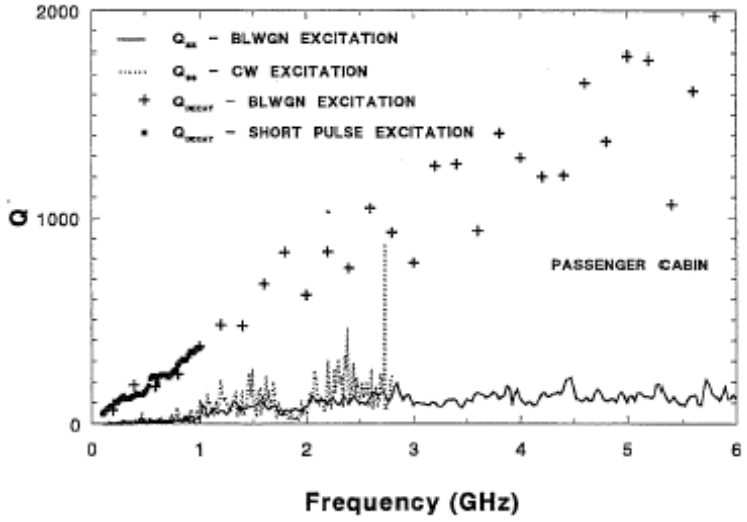

Figure 2. 21 Passenger cabin Quality factor comparisons (Figure 4-38. NSWCDD/TR-97/84 [13])

Received power measurements were performed using mode stirring while the aircraft cabins were exited using different excitation sources. Band limited white Gaussian (BLWGN) noise is used as a source in some cases and constant wave source (CW) in some. Both steady state *Q* (frequency domain) and the decay *Q* (time domain) are calculated when the chamber was operating in a CW mode and frequency swept mode respectively [13]. The differences between the two *Q* values as can be seen in Figure 2.20 and 2.21 are apparent. The time domain measurements seem to predict *Q* values that are larger than the frequency domain measurements.

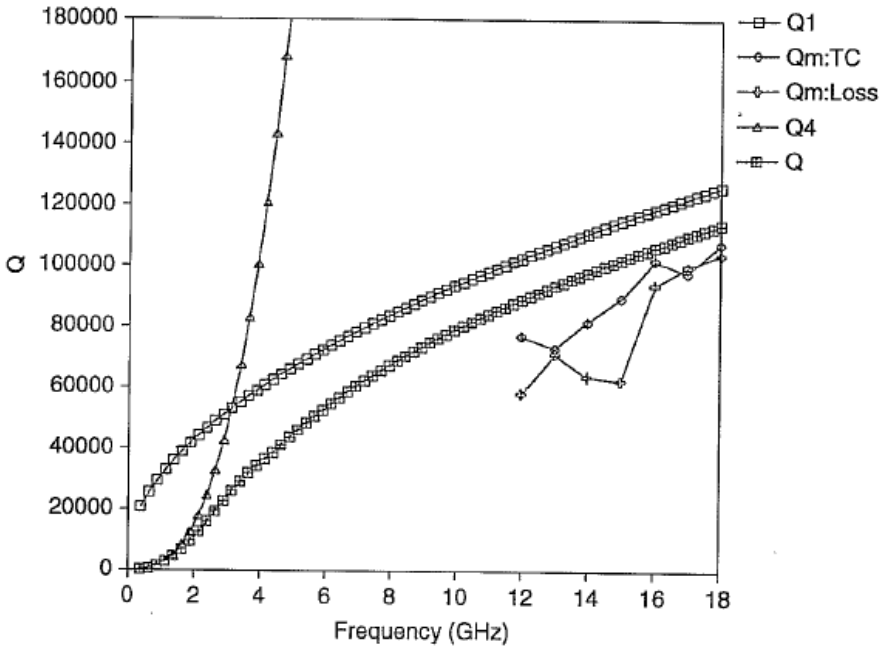

Figure 2. 22 Aluminum cavity Quality factor comparisons (Figure 7.13 [14])

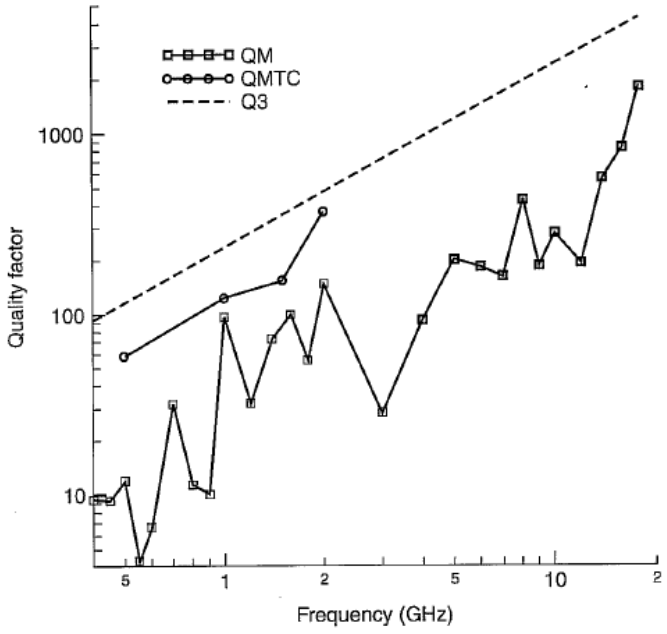

Figure 2. 23 Main cabin of the hangar queen plane Quality factor comparisons (Figure 11.1 [14])

Figures 2.22 and 2.23 are the measured *Q* values from an aluminum cavity and main cabin of the aircraft respectively. Power ratio measurements and decay time measurements were performed with standard gain horns in the frequency range specified [14]. The decay time measurements are closer to the theoretical *Q* values and Hill suggests that decay time measurements are less affected by antenna efficiency and impedance mismatch [14].

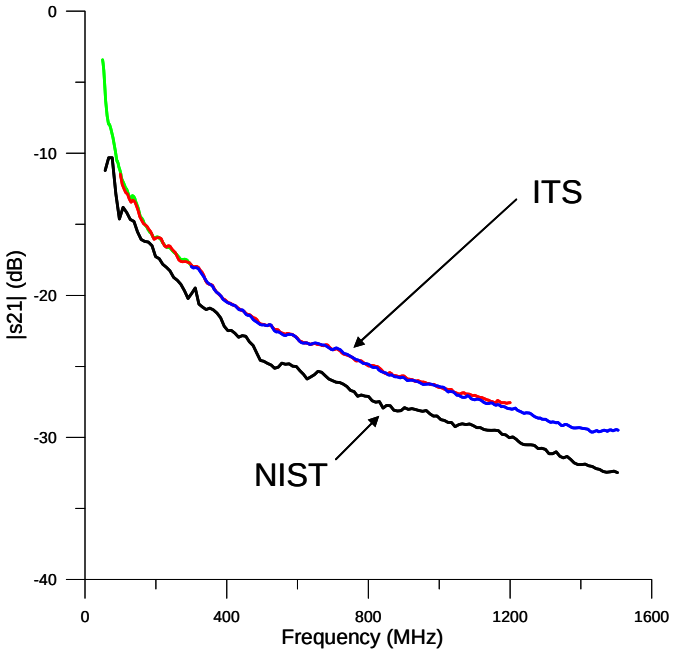

Figure 2. 24 S21 comparisons of the NASA SPF chamber with frequency domain measurements from NIST and time domain measurements from ITS
Courtesy: Bob Johnk, ITS and Galen Koepke, NIST

In Figure 2.24, more recent measurements performed in the NASA SPF chamber by National Institute of Standards and Technology (NIST-Boulder) and Institute for Telecommunication Sciences (ITS) are shown. The time domain measurement by ITS, used joint frequency and time analysis (JFTA) to estimate 1/e power decay rate to estimate *Q* [56]. Frequency domain measurements from NIST are direct S_{21} measurements made with the use of Vector Network Analyzer (VNA). Antenna

mismatch corrections applied to the measured data and S_{21} is used to infer *Q* factor as they are directly proportional. At almost all frequencies there is about a 2 dB difference between the ITS (time domain) and NIST data (frequency domain) with the time domain measurements always higher than the frequency domain measurements.

2.7 Q - Frequency and Time domain

In order to investigate the difference in *Q* that existed in our measurements and the surprising trend found in measurements made by different organizations in different time frames and different cavities, more measurements were performed in the SMART 80 chamber at multiple frequencies using the same experimental setup as explained before in both frequency and time domain. The average *Q* from CW measurements performed for multiple frequencies averaged over multiple antenna positions (at each frequency) is shown in Column 2 of Table 2.3. *Q* increases with frequency as expected and the average *Q* around 1 GHz is calculated to be 44.6 dB.

Table 2. 3 Measured Q values using frequency and time domain

Freq (MHz)	FD Q(dB)	TD Q(dB)	Difference (dB)
400	37.31	40.29	2.98
500	39.74	41.90	2.16
600	41.47	43.06	1.59
700	41.57	43.52	1.95
800	43.08	44.36	1.28
1000	44.63	45.44	0.81
2000	46.40	47.46	1.06

The *Q* values measured at different frequencies through time domain technique is tabulated in Table 2.3. As explained earlier, the frequency domain *Q* values reported at each frequency are the averages of Q values computed from five receive antenna positions inside the chamber. The S_{21} data are corrected for impedance mismatch via the S_{11} and S_{22} data in frequency domain and the antenna efficiency corrections were not applied. The *Q* values reported for time domain are calculated from 'τ' which in turn is obtained from the measured slopes of the average power decay curve at the center frequencies after time gating the initial reflections. The average power decay curves of the SMART 80 chamber at different frequencies measured in time domain are shown in Figure 2.25. The curves could be smoothed via averaging to obtain a more smooth decay curve leading to a better fit of the linear curve but as we are interested, in a quick measure and gross approximation, averaging is not applied to the measured data. The raw data was subjected to a linear fit and slope was calculated from that. The different decay slopes will result in different chamber time constants.

From Table 2.3, the *Q* values that are calculated using time domain method are seen to be higher than the CW method under all conditions. These results corroborate the results presented in [13] and [14]. The interesting questions that arise from this comparison are

- "Why is there a difference between the *Q* values that are measured using frequency and time domain?"
- "Which *Q* value represents the real *Q* of the environment?"
- "Should the frequency and time domain values be is some way "transformable"?
- "In what way are the measurements inherently different?"

- "Do the two different *Q* values represent two different observables of the cavity? And if so how?"

Some measurement parameters that influence the time domain measurements will be discussed in the following sections.

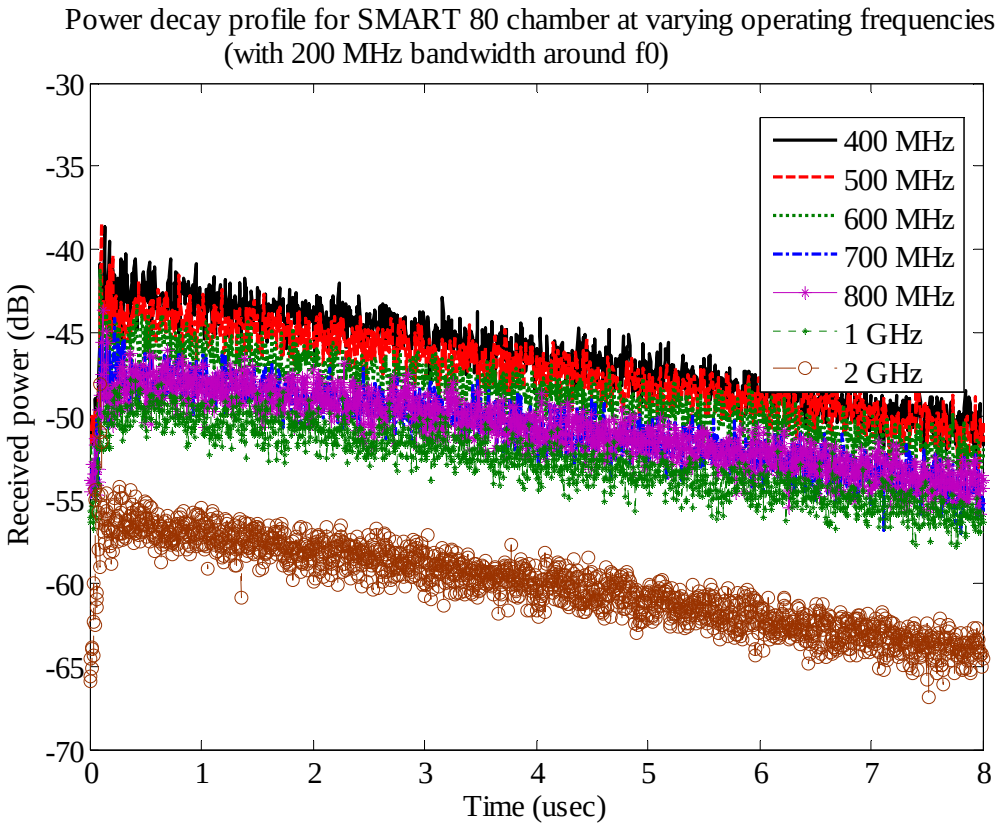

Figure 2. 25 Power decay profiles of SMART 80 Chamber at different operating frequencies

a. Choosing a Bandwidth

The wall scattering time defined as average time it takes for the energy to scatter of the walls [57].

$$T_c = \frac{4V}{Sc}$$

(2.8)

where V is the volume of the chamber, S is the surface area and c, speed of light.

For the SMART 80 chamber used in all the measurements presented here, the wall scattering time was calculated to be approximately 15 nsec. The bandwidth was chosen such that the pulse width was less than the wall scattering time by choosing a bandwidth of at least 150 MHz. The effects of choosing pulse widths larger and smaller than the wall scattering time will be discussed below.

b. Effects of Smaller Bandwidths (Longer pulse widths)

When the pulse widths are larger than the wall scattering time, the energy decay in the chamber is affected leading to a slope that was slightly larger than the slope calculated for pulse widths smaller than the wall scattering time. Measurements have been performed at a center frequency of 500 MHz and 5 GHz with the bandwidths varying from 80 MHz to 300 MHz in 20 MHz steps [58]. As can be seen from Table 2.4, the Q values seem to stabilize above 160 MHz bandwidths around the center frequency. If the pulse widths are larger than the wall scattering time of the chamber, the Q that is predicted seems higher (because of larger 'τ' values) than the Q's predicted when the pulse widths are smaller.

Table 2. 4 Q variation as a function of bandwidth around the center frequency of 500 MHz and 5GHz

BW (MHz)	Pulse width (nsec)	Q_{500} (dB)	Q_{5000} (dB)
80	25	43.71	51.26
100	20	42.78	51.14
120	16.7	43.02	51.10
140	14.3	42.72	51.18
160	12.5	42.48	50.98
180	11.1	42.37	51.02
200	10	42.26	50.94
220	9.09	42.11	50.82
240	8.33	42.16	50.82
260	7.69	42.06	50.90
280	7.14	42.11	50.67
300	6.67	42.06	50.80

The power delay profiles [69] measured for a center frequency of 500 MHz for varying bandwidths around the center frequency are shown in Figure 2.26a and 2.26b. The slope change as the bandwidth increases from 80 MHz can be seen from the graph.

c. Effects on Long Bandwidths: Aliasing time

If the bandwidths chosen are too wide, there could be two disadvantages. One, aliasing occurs due the FFT operation performed within the VNA. With 1600 measurement points, and a bandwidth of 200 MHz, the frequency step size is about 0.125 MHz (Δf) which leads to a 8 μsec alias at $1/\Delta f$. When the bandwidth is extended to1 GHz, aliasing occurs at 1.6 μsec.

In order to find a slope of the power decay curve, the power decay needs to be observed for a few μ seconds and the received power should be above the noise floor of the instrument used. A linear fit to the power decay data will result in a better prediction of

‘τ’ values. If the bandwidth chosen is too wide then the observation time is reduced due to aliasing leading to a poor fit thereby a poor estimation of τ.

Secondly if the chosen bandwidth is too wide, the τ value which is a function of frequency will be varying significantly across the bandwidth which may lead to a poor estimation of τ at the intended center frequency. While using a wide bandwidth, the τ predicted will be a combination of different delay spreads and may not be representative of the delay spread at the intended center frequency.

It can then be suggested that a bandwidth that is not too wide or too short needs to be chosen. The lower bound on the frequency bandwidth is provided by the pulse widths smaller than the characteristic wall scattering time (which is a function of the operational space) and the upper bound is provided by the non aliasing time and variation of τ across wider bandwidths.

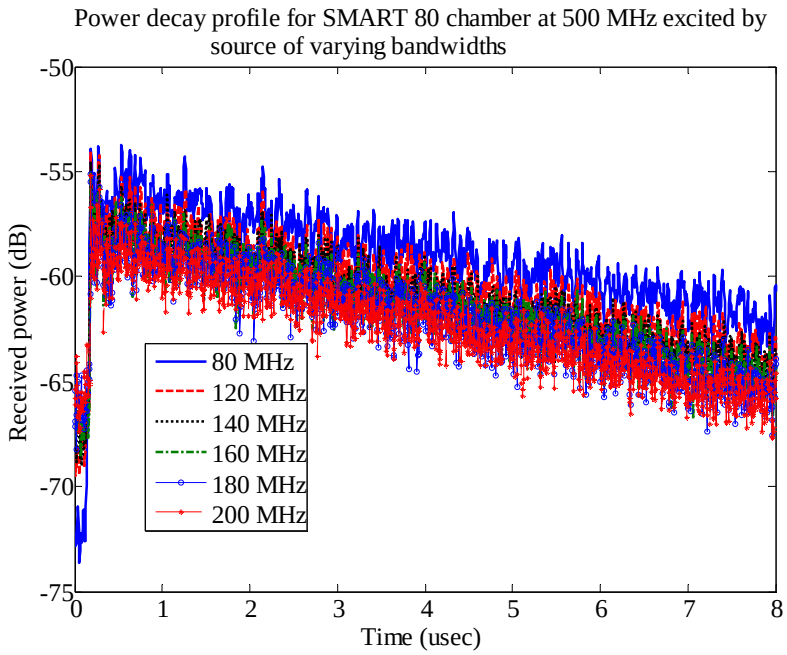

Figure 2. 26 a. Power decay profile of SMART 80 Chamber at 500 MHz and varying bandwidths (80-200 MHz)

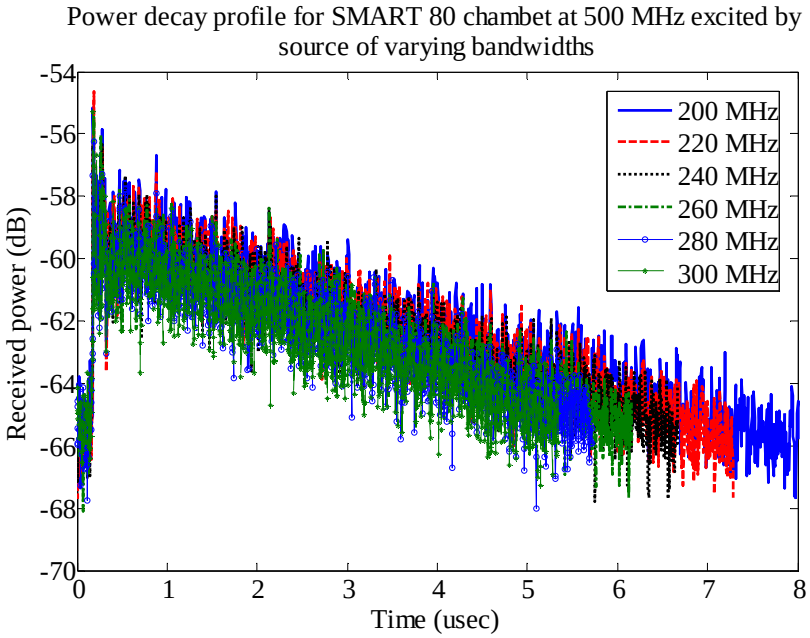

Figure 2.26 b. Power decay profile of SMART 80 Chamber at 500 MHz and varying bandwidths (200-300 MHz)

d. Effect of Efficiency

When insertion loss measurements are performed in a reverberation chamber, the physical construction of the antennas contributes to the complexity inside the chamber. The antenna mismatch and the efficiency of the antenna to couple power into the cavity (we will call this coupling efficiency) must be considered in the calculation of gain of the chamber. The efficiency that is defined here is different from the radiation efficiency of the antenna as there is power reflected back from the chamber to the antenna which is unique to antennas operating inside high *Q* cavities. In the frequency domain when measurements are performed at single frequency, the measured reflection coefficient consists of energy that is reflected due to the antenna mismatch and energy that is reflected from the chamber back through the transmit antenna [59]. These two exist together in a CW measurement and cannot be separated while in a time domain measurement, these two effects can be separated out.

In a CW measurement, *Q* is calculated from the power ratio measured with the antennas. A better estimation of *Q* of the chamber is possible when the data is corrected for impedance mismatch and coupling efficiency. In the time domain measurement, *Q* is calculated from the slope of the energy decay curve. As no absolute powers are considered in the time domain calculation, the coupling efficiency and mismatch seems insignificant. To verify this claim, time domain measurements have been performed at 1 and 2 GHz with a pair of LP antennas used as Tx and Rx and one LP antenna and a piece of wire used as Tx and Rx respectively.

The *Q* values from the measurements are reported in Table 2.5. The raw received power in the CW measurements was corrected for impedance mismatch (from reflection coefficients) and not for initial reflections from the chamber. At 1 GHz the difference between the *Q* values (frequency domain) calculated with two different receiver antennas is ~2dB. The *Q* values calculated with the wire as the receiver were lower than the *Q* calculated with LP as the receiver. This is an expected result as the coupling efficiency of the wire antenna might be different compared to the coupling efficiency of the LP antenna. The agreement between the *Q* values (time domain) obtained using two different receive antennas at both frequencies is noticeable.

Table 2. 5 Measured Q values using two different receive antennas

Freq (MHz)	Rx- LP		Rx - Wire	
	FD Q(dB)	TD Q(dB)	FD Q(dB)	TD Q(dB)
1000	44.63	45.44	42.8	45.61
2000	46.4	47.46	47.08	47.88

The above results shows a possibility of using any available antenna (in-band or out of band) or easily fabricated from a piece of wire could be used in time domain measurements for the estimation of quality factor of rooms and cavities provided the antennas used are able to couple energy into the cavity and the receiver can sense power levels above the noise floor which is to say that the antennas have enough dynamic range.

e. Effect of impedance mismatch

A typical frequency domain measurement is a steady state measurement implying that the signal has been present for a time that is usually greater than the cavity fill time. The

energy is fully coupled from the transmitter into the cavity and steady state has been reached inside the cavity before a measurement was made with the receive antenna. Hence the received power at some position inside the cavity is measured from the steady state response of the cavity.

The measured reflection coefficient consists of energy that is reflected from the antenna mismatch and energy that is reflected from the chamber back through the transmitter antenna. These two effects coexist in frequency domain but could be decoupled in time domain. Hence while performing a time domain measurement the impedance mismatch created by the antennas can be neglected.

In Figure 2.27, the S parameters measured with a LP antenna pair at f = 1 GHz are plotted against time. From the graph the initial reflection from the antennas can be seen both in S_{11} and S_{22} curves. The initial reflections due to the mismatch at the antenna terminal can be seen at the earlier time frame (1^{st} peak) followed by the reflections from the chamber (2^{nd} peak). The initial reflections from the chamber can be considered as the time before the reverberant field is setup inside the cavity (unstirred energy) or the inefficiency of the tuner to stir the fields. At any case, the initial reflections contribute the coupling efficiency of the antenna. S_{21} is a function of the energy coupled into the cavity, interacting with the walls/tuner and being detected back at the receive antenna. The slope of measured power decay will lead to a better estimation of the chamber time constant and a better estimation of the conductivity of the material used in the chamber walls at

operational conditions and will not be affected by the initial reflections from the antennas.

As discussed earlier, the possibility of using any available antennas, even if the antennas are not matched well at the intended frequencies of operation, in time domain measurements for an approximate *Q* measurement is fairly high.

As the time domain measurements measures the τ (from the slope of the energy decay gated after the initial reflections), and not from power ratio, resulting in minimal contribution from the antenna impedance mismatch and coupling efficiency, the time domain methods appears to be efficient in measuring the quality factor compared to frequency domain methods.

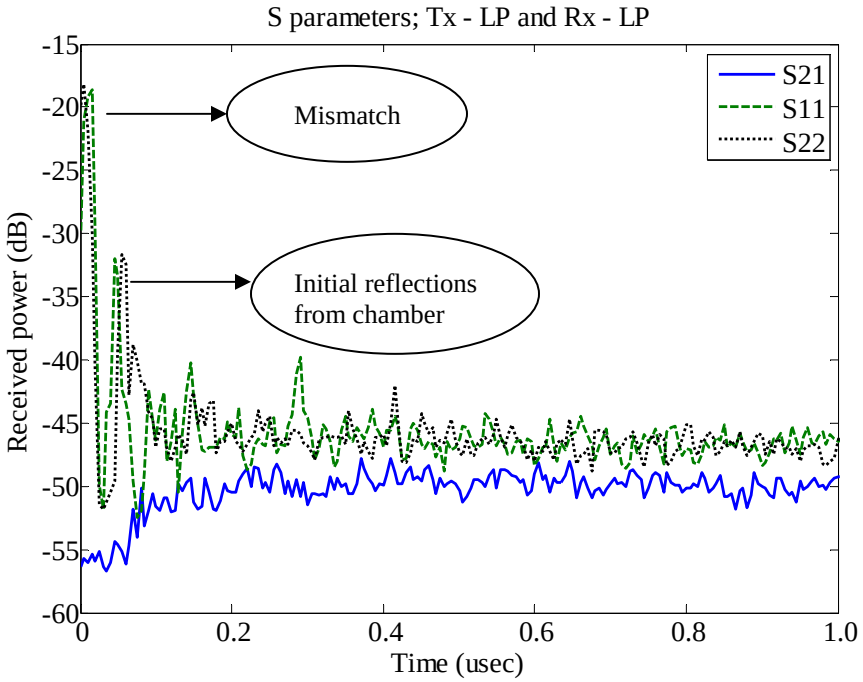

Figure 2. 27 Measured S parameters of the SMART 80 chamber at 1 GHz with LP antennas as Tx and Rx

f. Loading

To simulate loading conditions and to sketch the efficiency of time domain measurements in detecting the energy decay due to loading, measurements were performed at 1 and 2 GHz using a pair of LP antennas and using absorbing cones as load.

The absorbers were placed at a corner of the chamber away from the antennas. The *Q* values calculated using both frequency and time domain measurements at both frequencies and loading conditions are shown in Table 2.6. The absorbing cones provided approximately 4 dB of loading at both frequencies. The energy decay curve (average of 50 distinct tuner positions) for both frequencies, empty and loaded conditions are shown in Figure 2.28. As one would expect when there is a load present in the chamber, energy absorption by the load would result in less energy available in the chamber and the energy decay rate would be much faster which is evident from the larger slopes of the decay curves.

Table 2. 6 Measured Q values for an empty and loaded chamber at 1 and 2 GHz

Freq (MHz)	Empty chamber		Loaded chamber	
	FD Q(dB)	TD Q(dB)	FD Q(dB)	TD Q(dB)
1000	44.63	45.44	40.36	41.41
2000	46.4	47.46	42.19	43.53

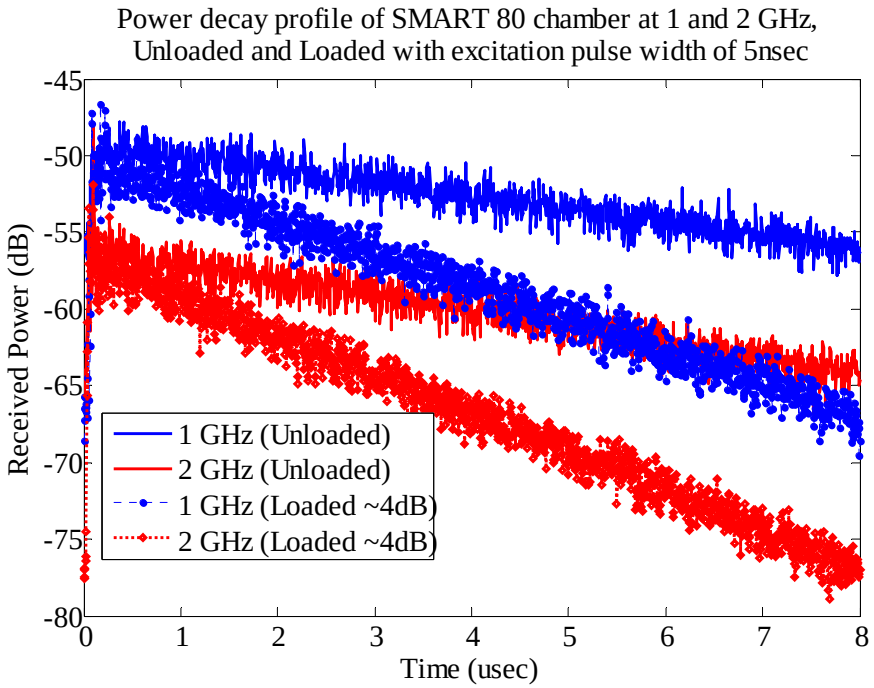

Figure 2. 28 Power decay profile of an empty and loaded SMART 80 chamber at 1 and 2 GHz

The versatility of the time domain measurements in capturing the power decay characteristics of the cavity is clear from the above measurements.

2.8 Difference between Frequency and Time domain Q Factor

The difference in the *Q* values calculated using the frequency and time domain techniques are primarily due to the way the antenna losses are handled in each domain. Though the impedance mismatch that occurs at the antenna terminal can be accounted for in frequency domain, the coupling efficiency cannot be. The antenna efficiency (treated as radiation efficiency) values that are used in most standards (LP – 0.75 and DRG – 0.9 [4]) are rather arbitrary and might vary from antenna to antenna. Though the antenna

efficiency numbers are a good approximation, they can be manipulated to offer a better match to theoretical or simulated values.

The time domain measurements are rather not influenced by the impedance mismatch and efficiency, especially in the measurement of quality factor and decay time constants of cavities.

2.9 Calculating Antenna to Chamber Coupling Efficiency

If the antenna impedance mismatch can be measured precisely using the VNA and if the time domain measure of power decay profile of the chamber provides a good estimation of the chamber characteristics, there exists a possibility to measure the coupling efficiency precisely under operating conditions.

As the coupling efficiency is the one parameter that is different between the frequency and time domain measurements, by comparing the S parameter measurements from the two techniques, the coupling efficiency can be calculated. From the Q calculated using time domain, the chamber gain can be calculated using eqn. 2.3 and comparing those values with the frequency domain measurement, the coupling efficiency is calculated. From the measurements made with this study, coupling efficiency calculated for the Log Periodic antenna used as a receiver (with another LP antenna used as a transmitter), at discrete frequencies are tabulated in Table 2.7.

Table 2. 7 Antenna efficiency calculated from Time domain measurements

Freq (MHz)	S_{21} – FD (measured)	S_{21} – TD (calculated)	Eff.%
400	0.036	0.071	50.2
500	0.032	0.053	60.7
600	0.028	0.040	69.3
700	0.018	0.028	64.0
800	0.017	0.023	74.4
1000	0.012	0.015	82.9
2000	0.002	0.004	66.2

A method of calculating coupling efficiency in reverberation chambers is presented which differs from all previous efforts to measure the antenna efficiency using a reverberation chamber [60 61 62 63]. The major advantage of this method is that, efficiency is measured under operational conditions of the antenna. There is no need for a second or reference antenna (with a known gain) to calculate the efficiency of the antenna in use. It also eliminates performing measurements inside and outside the chamber to calculate efficiency.

The coupling efficiency calculated using this measurement procedure again ascertains that the suggested antenna efficiency of 0.75 for a Log Periodic antenna might not be always true. The efficiency as expected will vary across frequency as high as 20% as in this case. Time domain technique has an advantage of neglecting the efficiency of the antenna to estimate *Q*.

2.10 Summary

The advantage of a time domain method in the estimation of time decay constant of the chamber is that the direct path components can be windowed out so that only the multipath effects are considered. The parameters that need attention in performing an efficient time domain measurement is brought out in this paper. The difference in the quality factor measured with frequency and time domain has been of interest and has received some attention in a number of reports, and this work has attempted to address the possible reasons for the discrepancy. The effects of antennas that are used in these measurements can be separated in time domain measurements which enable the measurement of antenna properties while in the frequency domain approach the antenna affects are inseparable.

The effective wall conductivity and absorption coefficient for rooms/cavities can be quickly determined from measured time domain data which is more practical as the effective conductivity is measured in a more realistic operational environment. This knowledge can be further used in the estimation of max field levels inside the cavity for a known input power level and reverberation distance.

Coupling efficiency could be calculated under operational conditions of the antenna by comparing the frequency and time domain measurements. There is no need for multiple measurements or using a reference antenna to calculate the efficiency of the antenna in

operation. Time domain measurements could be highly useful and efficient in the gross estimation of quality factor of spaces under operating conditions.

The time domain method may be the fastest way to calculate the reverberation distance as any direct coupling between the antennas if exists can be eliminated using windowing and also the separation distance between the antennas need not be varied. The insertion loss calculated using the received power data for both *Q* and *K* type of measurements seem to follow the pattern as expected above and below the reverberation distance. This provides extra confidence in the calculated reverberation distance. Determination of this distance could be important while placing wireless systems into enclosed cavities where an estimate of the maximum field can be quickly established depending on the distance of separation between the victim and the aggressor.

In the next chapter, the importance of independent samples for arriving at statistical distributions will be discussed. The influence of loading on independent samples and also uniformity will be discussed in detail with some experimental data. Some methods to increase the number of independent samples using a second tuner will be presented along with discussion about the size and the location of the second tuner.

Chapter 3

3.0 EFFECT OF LOADING ON INDEPENDENT SAMPLES

Independence is a key parameter in any statistical analysis. If two events are said to be independent, then by probability theory it means that the occurrence of one event, makes it neither more nor less probable for other events to occur. When fitting a probability distribution for the measured data set (set of random variables), all data points need to be independent. Use of correlated or dependent data, impacts the attempt to hypothesize a particular distribution. As the statistics are skewed with correlated data, any distribution to fit the measured data could be acceptable.

Of more importance is to determine how many independent samples are required to determine an electric field or power density distribution of a room or cavity. For a cavity, the number of IS provides information regarding the reflectivity of the cavity and also the number of statistically independent field configurations that could exist inside the cavity. In order to characterize a cavity, all the independent samples available should be utilized to reduce the uncertainty. IS can also be interpreted as the number of measurement points inside the cavity that should be utilized to produce an estimate of received power or a prediction of the maximum field with minimum uncertainty.

An important question that this work will address is “What happens to the number of independent samples when the cavity gets populated with either personnel or equipments or furniture (in an office space)?” Will the established probability distribution for the empty case still be valid? To explore this, some measurements have been performed inside a reverberation chamber where the number of independent samples has been estimated with reasonable accuracy through standard procedures. Then the chamber was loaded with some absorber materials and the effect of loading on IS is monitored. The statistical variation in the estimation of IS and the limitations are shown to be present. Methods to increase the number of independent samples which might help to compensate for the loading and improve the measurement accuracy are also investigated.

3.1 Independent samples (IS)

For a typical reverberation chamber the number of independent samples can be defined as the number of statistically independent field configurations that can exist in the chamber at a particular frequency over one complete rotation of the tuner (or variation over a set of boundary conditions). The number of independent samples is a function of frequency and the number of measured samples at each frequency.

The estimation of independent samples is possible using autocorrelation which measures the relative correlation between a sequence of ‘N’ samples and an offset of the same sequence. Identifying the number of IS is critical for the estimation of the max fields

during the test and the uncertainty associated with the test. The autocorrelation function that is used to calculate the independence is given below.

$$\rho_j = \frac{\sum_{i=0}^{N-1} (x_i - \mu_x)(x_j - \mu_x)}{\left[\sum_{i=1}^{N} (x_i - \mu_x)^2\right]} \qquad \textbf{(3.1)}$$

$$j = \begin{cases} i-m, & i > m \\ i-m+N, & i \le m \end{cases}$$

Where x_i y_j are linear, mean normalized data from an 'N' sample sequence. The distribution of y_j is same as x_i shifted by a sample offset m. μ_x is mean of original N sample sequence. Since the *y* distribution is same as *x* except for offset, the means and standard deviations are equal ($\mu_y = \mu_x$, $\sigma_x = \sigma_y$)

An operationally common practice assumes that ρ < 1/e = 0.367 implies independence. As the underlying distribution is normal, uncorrelation implies independence. A statistically more robust criterion is given below [15].

$$P_N(|\rho| \ge |\rho_0|) = \left[\frac{2\Gamma\left(\frac{N-1}{2}\right)}{\sqrt{\pi}\Gamma\left(\frac{N-2}{2}\right)}\right] \int_{\rho_0}^{1} \left(1-\rho^2\right)^{\left(\frac{N-4}{2}\right)} d\rho \qquad \textbf{(3.2)}$$

If the probability that N samples of two uncorrelated variables have a correlation coefficient $|\rho| \ge |\rho_0|$. ρ_0 is the strictness factor and can be chosen based on the amount of uncorrelation expected. For true uncorrelation, ρ_0 is chosen to be zero, commonly it is

chosen to be 0.367. If $P_N(|\rho| \geq |\rho_0|) \leq 5\%$, the correlation is called significant and if it is less than 1%, the correlation is called highly significant i.e. the samples are highly correlated. Depending on the procedure that is used to calculate the number of IS there could be as much as a 40% variability [32]. When the max fields are estimated using the number of IS, the error margin in the estimation of IS translates to higher uncertainty in the estimation of test fields hence the over test/under test margin.

In practice, a smaller number of test samples are chosen than the total available IS [4]. Note: The assumption typically made is that all the chosen test samples are independent. The assumption will only be valid if the number of available IS are far greater than the test samples. At higher frequencies the total number of IS are large while at lower frequencies this might not be true. Adding the 40% variability to the estimate of IS complicates the situation.

When the equipment under test is placed inside the usable volume of the chamber for testing, the EUT loads the chamber. What is the influence of loading on the number of IS? If the chamber loading reduces the available number of IS, the impact at the low frequency side is significant because of the lower number of IS available. In order to investigate the variation between repeated measurements just as a function of statistical sampling, the number of measured samples required, criteria used and the effect of loading on the estimation of independent samples, a series of measurements were performed as detailed below.

3.2 Experimental setup

The measurements were performed in the SMART 80 chamber at frequencies 1-5 GHz where the mode density of the chamber is high and all the chamber statistics are good (Ref: Figure 2.2). A pair of dual ridge waveguide horns served as the transmit and receive antennas while the VNA was used to measure the insertion loss of the chamber. Being a statistical procedure, there is an uncertainty with the way the fields are sampled. This uncertainty cannot be neglected. Also the more number of data samples there are, a more complete statistical description is possible. Hence the number of measured samples is always chosen to be maximum available which is 1600 samples per complete rotation of the tuner in our case. To look at the variation in the estimation of IS from a set of repeated experiments, insertion loss measurements were carried out at 10 different positions of the receive antenna for an input frequency of 1GHz.

Autocorrelation analysis was performed on the measured data and the number of IS were estimated from a correlation value of $\rho = 0.367$. The experimental setup is shown in Figure 3.1. Table 3.1 contains the estimated number of IS for every repeated measurement along with the measured and expected max to mean ratios.

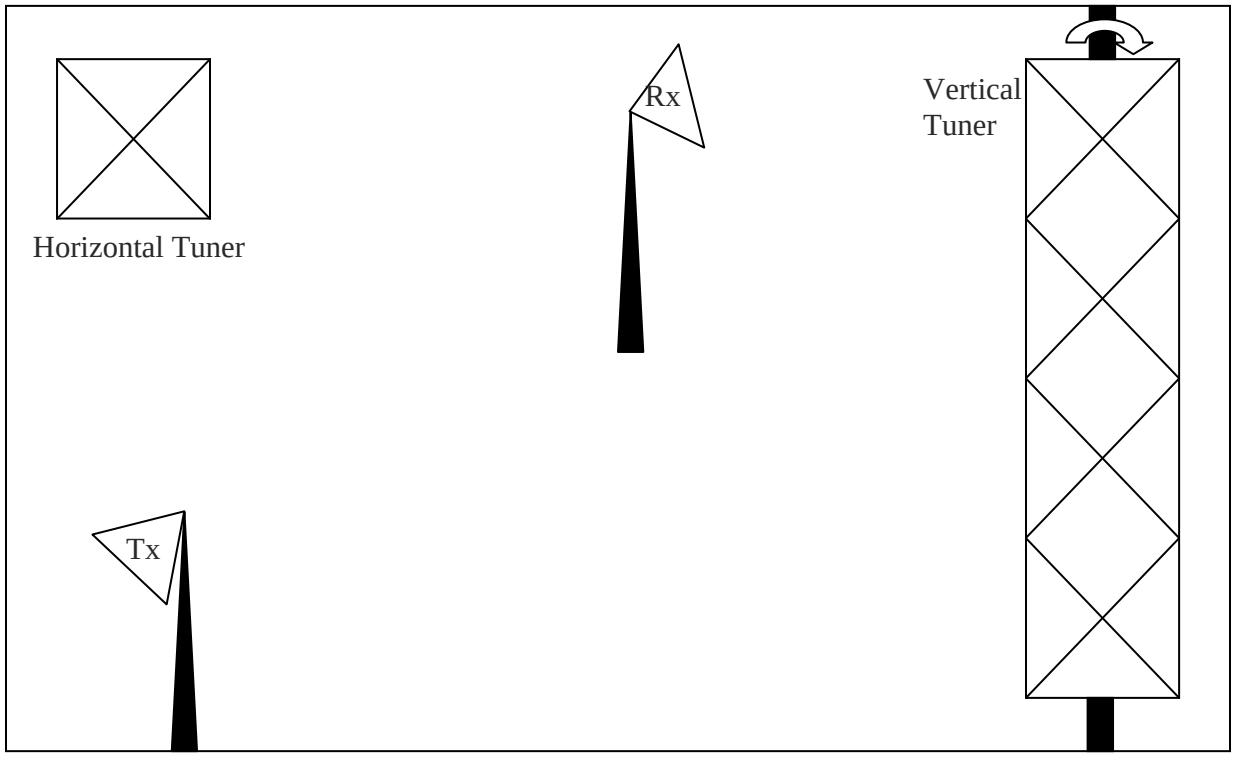

Figure 3. 1 Experimental setup for measuring independent samples in a reverberation chamber

Table 3. 1 Measured Independent samples for 10 repeated measurements

Measurement Position	IS	Measured Max/Mean (dB)	Norm. SD	Expected Max/Mean (dB)	SD
1	**230**	8.25	0.99	7.68	0.93
2	**270**	7.69	0.93	7.8	0.91
3	**270**	8.36	0.98	7.8	0.91
4	**270**	7.24	0.91	7.8	0.91
5	**230**	8.03	1.01	7.68	0.93
6	**270**	8.84	0.98	7.8	0.91
7	**270**	7.05	0.97	7.8	0.91
8	**320**	7.1	0.95	7.92	0.89
9	**270**	7.9	1	7.8	0.91
10	**230**	8	0.97	7.68	0.93

The variability among the estimation due to the sampling and from Table 3.1 it is calculated to be 28.1%.

Table 3.2 shows the ρ values calculated for two different significant values and different number of measured samples using eqn. (3.2). Using an extrapolated coefficient value of 0.24 for 1600 measured samples for correlation at a highly significant level (1%); the number of independent samples for the measured data is estimated to be roughly 200.

Table 3. 2 Correlation values calculated for different measured samples

No. of Samples	P = 5%	P = 1%
12	0.576	0.707
20	0.445	0.562
30	0.361	0.463
50	0.278	0.361
100	0.197	0.255

The variation between the IS calculated using eqn. (3.2) and the 1/e criterion is 23.9 %. In order to characterize the chamber at some frequency of operation, maximum number of data samples need to be captured. To look at the effect of the number of measured samples on the estimate of independent samples, the number of measured samples per rotation of the tuner was increased. 1600 data samples were captured for every 16 degrees rotation of the tuner. The total number of measured samples per rotation was then increased to 32000 samples. This data was parsed down and IS was estimated from the available data. Every second sample or third or so forth sample was considered for autocorrelation analysis and the number of IS was estimated using the 1/e criterion.

Table 3. 3 Independent samples as a function of measured samples

Measured	Independent
32000	440
16000	440
8000	440
4000	400
2000	400
1000	330
500	250
200	200
100	100

From Table 3.3, it can be seen that at 1 GHz the total number of independent samples that the chamber can generate is about 440. The maximum available number can only be seen when the measured samples is at least 8000. Hence to determine the maximum number of IS at any frequency maximum number of measured samples must be captured.

To evaluate the influence of loading on the estimate of IS, absorbing material was used inside the chamber to simulate different loading conditions. The number of measured samples was fixed at 1600 per rotation. At every frequency and every loaded condition, the receive antenna was placed at 5 fixed positions inside the chamber and the average of IS from the different measurement positions is the IS (<IS>) for that frequency and loading condition. By averaging out the IS at every experiment, the only variability that existed was the sampling and the load. For frequencies 1 - 5 GHz in 1 GHz steps, insertion loss was measured for a no load condition and load was added in 4 different steps. The maximum load was at step number 4 (~12 dB; this would be the difference between empty chamber *Q* and loaded *Q*), calculated as the difference between the *Q* of the empty chamber and *Q* of the loaded chamber.

Table 3. 4 Independent samples measured at different frequencies and loading conditions

Freq. (GHz)	No Load	Load 1	Load 2	Load 3	Load 4
1	384	238	213	195	109
2	534	395	368	302	183
3	801	534	464	454	278
4	801	801	587	507	334
5	801	801	747	747	368

As the frequency increased the number of independent samples increased irrespective of the loading (Ref: Table 3.4). When loading increased, invariably at all frequencies, the estimated number of IS reduces. This uncertainty is not addressed in current RC applications.

The quality factor of the chamber also varies with respect to loading and frequency hence at all frequencies, Q was calculated using insertion loss data in eqn (2.3) (Ref Section 2.2.1 in Chapter 2) and is tabulated in Table 3.5.

Table 3. 5 Quality Factor measured at different frequencies and loading conditions

Freq. (GHz)	No Load	Load 1	Load 2	Load 3	Load 4
1	46.33	42.5	41.15	40.29	34.69
2	48.25	44.99	43.42	42.54	37.17
3	48.41	45.4	44.28	43.41	38.32
4	49.22	46.11	44.8	44.35	38.69
5	51.6	49.18	47.98	47.11	41.95

As seen in Table 3.5, Q increased with increase in frequency for each loading configuration. As the load is increased at a particular frequency, Q goes down as expected. At the maximum load, the loading is about 12 dB at 1GHz and about 10 dB at 5 GHz. Loading the chamber reduces the Q as expected but also influences the independent

samples. The estimated IS reduces with loading regardless of frequency. This phenomenon was also reported in [17 18] but the effects at low frequencies was not explored. In [19] it has been reported that the number of IS *increases* with loading. The minimal increase (10 to 14) is within the 40% variability in just the calculation of IS from the 1/e criterion as was shown in Table 3.1.

In our effort to validate our claims, the unpublished work of Greg Tait [16] was brought to bear on this issue. Tait's procedure utilizes the measurement of maximum power inside the chamber and calculates the number of IS from a maximum power measurement. From the multiple maximum measurements, the mean and the standard deviation of the relative maximums will be calculated and the normalized standard deviation which is the ratio of the standard deviation of the maximums and the mean of the maximums will be plotted against the number of IS. The equations used to plot this curve were extracted directly from Taits work and are given below [16].

$$I(N) = \frac{\int_0^\infty w^2 f_N(w)dw}{\left[\int_0^\infty w^2 f_N(w)dw\right]^2} = 1 + S_n{}^2 \qquad \textbf{(3.3)}$$

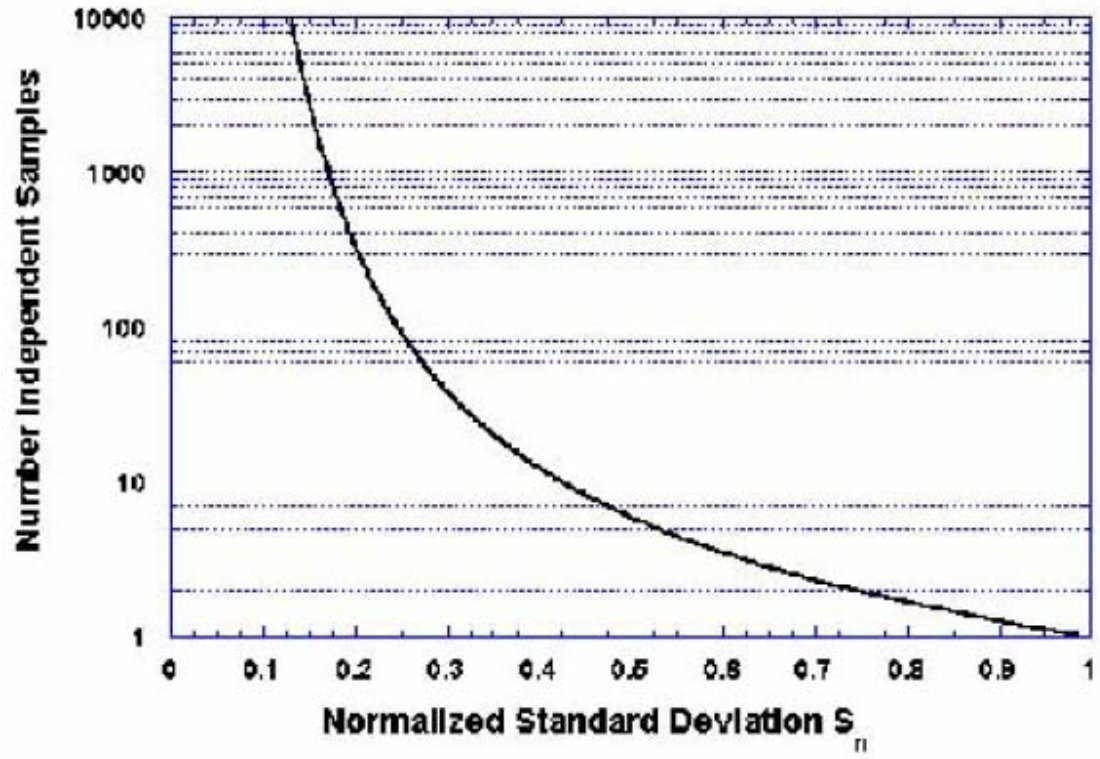

Figure 3. 2 Independent samples versus normalized standard deviation [16]

As the max to mean ratio follows a Chi Square distribution with 2 degrees of freedom [4], a Monte Carlo analysis was performed by randomly selecting data from a Chi Square distribution. Figure 3.2 might be a limiting value for a large number of measurements. Hence the Monte Carlo analysis was performed by varying the number of trials and the results are given in Figure 3.3.

When the number of trials is reduced to 12 or 5, the deviation from the theoretical curve and prediction of fewer IS can be seen in Figure 3.3. Also the statistical noise in the estimation of the normalized standard deviation is large when the number of IS are large and fewer the measurement trials (12 or 5) making it hard to estimate the actual number of IS. This implies that the estimation of IS may be strongly dependent on the number of measured maximums. A closer look of the 12 and 5 measurement trials is shown in

Figure 3.4 where the small difference in the calculated normalized standard deviation resulting in variation of the IS are clearly seen (referred as statistical noise).

A similar approach can be used to estimate the influence of loading on independent samples but there needs to be a large number of measurements of maximums to estimate the number of IS with minimal statistical noise.

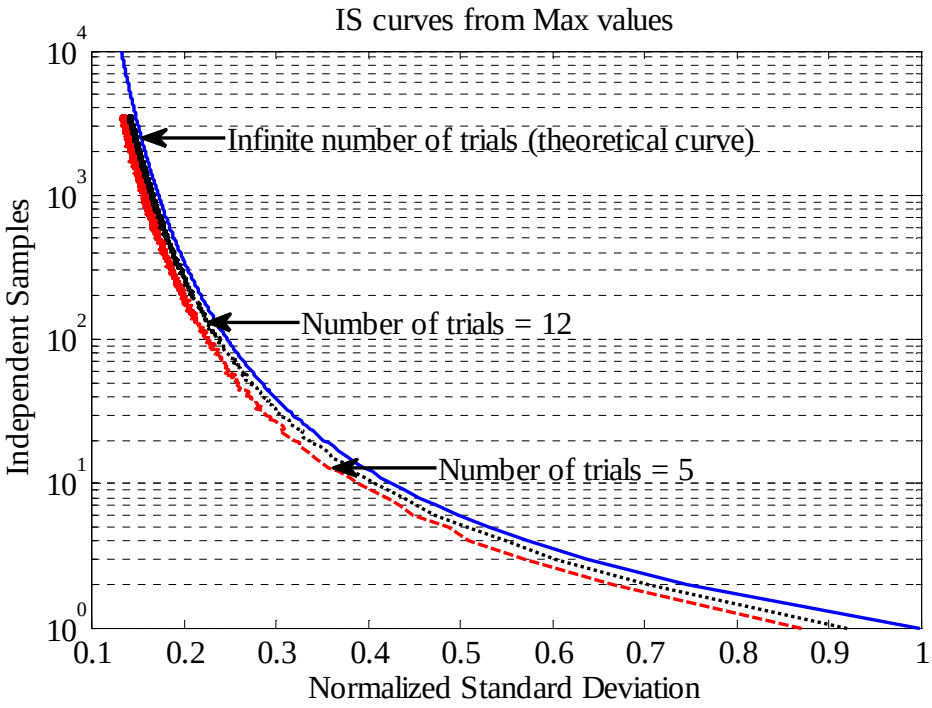

Figure 3. 3 Independent samples versus normalized standard deviation for different number of trials from Monte Carlo Simulation

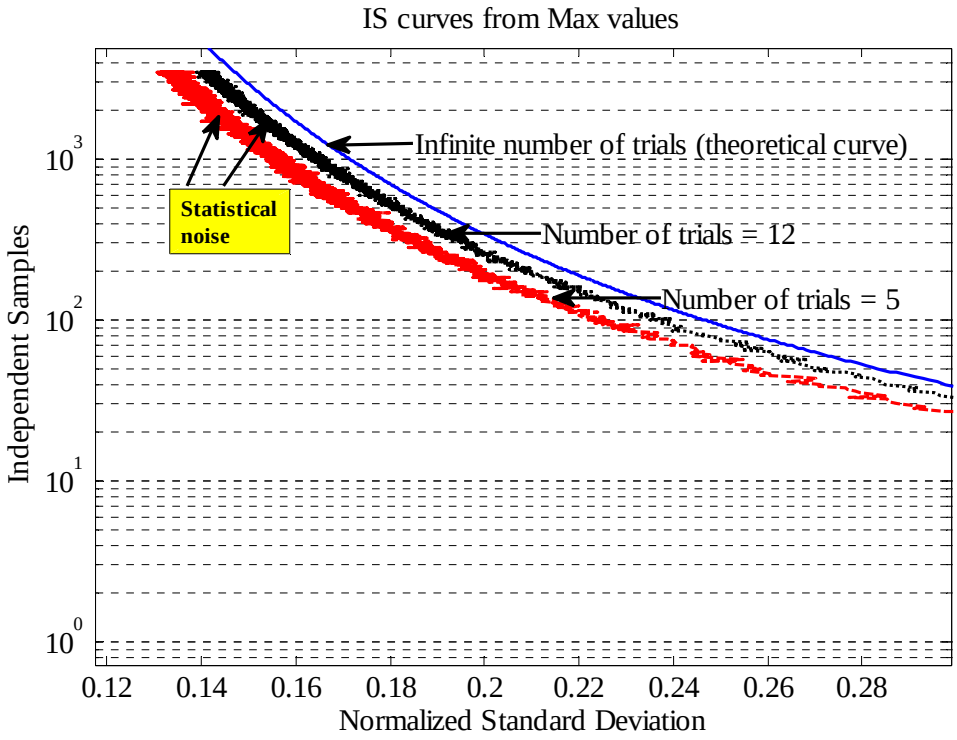

Figure 3. 4 Independent samples versus normalized standard deviation for different number of trials from Monte Carlo Simulation (closer look)

3. 3 Uniformity Independent samples and Loading

Uniform implies all spatial locations within a working volume are equivalent within an acceptable uncertainty. Uniformity is usually measured with multiple monitor antennas and includes variation in location, orientation, polarization of the antenna and 3-axis probe is used to measure the fields with a constant input power. Uniformity is characterized by standard deviation of the data. For a well-stirred chamber, the uniformity is good which implies that the variation from point to point within the usable volume of the chamber is small (different standards have different standard deviation values for acceptable uncertainty for different frequency bands).

For acceptable operation of a reverberation chamber, the independent samples must be fairly large and also the uniformity must be within acceptable uncertainty. It has been implied (without proof) that by increasing the number of IS, the uniformity can be improved [4]. The work in Section 3.2 shows that increasing loading decreases IS within the SMART80 chamber, if the no. of IS is proportional to uniformity of the chamber then uniformity should decrease with loading. For a very high *Q* chamber, it is recommended to add absorbing material to increase the uniformity within the usable volume [4]. This suggestion may be contradictory to what has found in this work.

The relationship between uniformity, independent samples and loading will be discussed to address the apparently contradictory implications. The 3 major observations/ rules of thumb are as follows,

1. Increasing the tuner steps (independent samples) increases uniformity
2. Increasing the loading increases uniformity (at least in initial stages of loading)
3. Increasing the loading decreases the number of independent samples

Observation 1

When the chamber is calibrated at low frequencies the mode density is not high and the chamber may not pass the 3dB uncertainty requirement if 12 tuner steps are used (12 is the suggested minimum number of tuner positions for all standards). In this case, the number of tuner positions may be increased to decrease the standard deviation hence improving the uniformity provided the number of available independent samples is fairly large. If the chamber does not pass the uniformity test with 12 tuner steps and is not

capable of producing any more independent samples, it implies that the chamber cannot be used for testing at that low frequency due to poor mode density.

Observation 2

If the chamber has a very high *Q* (which may occur at high frequencies), the mode density in the chamber is high but the number of modes that are excited within the *Q* bandwidth is very small. This "high selectivity" condition may also lead to a poor uniformity. An example is provided in Figure 3.5.

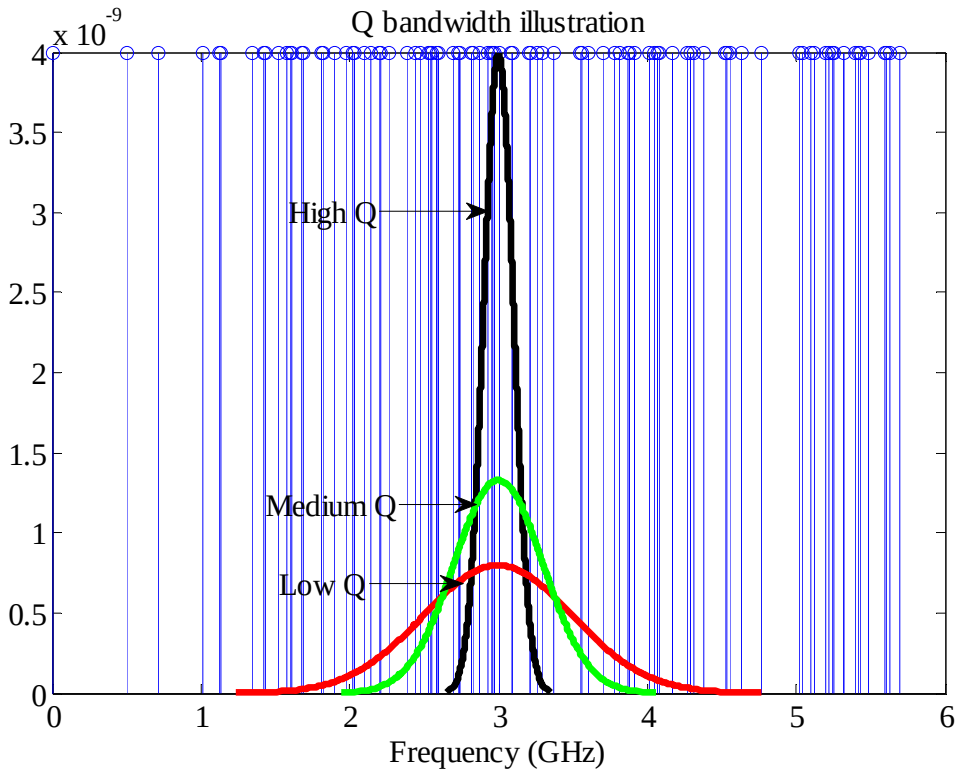

Figure 3. 5 Illustration of Q bandwidth for a rectangular cavity

The black curve represents a high *Q* cavity and the number of modes that are excited within the *Q* bandwidth is small hence the uniformity may be poor. Though the physical

structure of the cavity itself has a high mode density at higher frequencies, the *Q* bandwidth is small.

To increase the *Q* bandwidth, typically, a small amount of loading is added inside the chamber (sometimes this loading can also be provided by the introduction of the EUT inside the chamber). As the load is introduced, the *Q* of the cavity goes down as energy is also being absorbed by the load. This reduction in *Q* can be represented by green response in Figure 3.5. As it can be seen, the number of modes that are excited within the *Q* bandwidth is now more. The energy distribution between the modes is now better (as more number of modes are excited) leading to better uniformity. When the loading is significant, the energy absorbed by the EUT is much more than the energy dissipated by the walls and it might lead to a point where the uniformity is poor.

When the *Q* is reduced due to significant loading, though more modes are excited, the additional modes that are excited due to the increase in *Q* bandwidth may not be significantly different from the previous set of modes hence there is no increase in the number of IS rather there is a decrease in the number of IS.

Significantly different modes lead to independent samples and not just more modes. When the *Q* bandwidth is increased to include more modes in the *Q* bandwidth, the additional modes do not lead to sufficient change in the modal structure to increase the number of IS.

Observation 3

From the experimental results that were shown in this study, it is clear that loading decreases the number of available IS. This initial observation needs more work to understand the relationship between uniformity, loading and IS.

The discussions that are presented here are to be regarded as being plausibility arguments and not proofs. The purpose of the comparison between independent samples, uniformity and loading is to stimulate an interest and lay a background of general understanding upon which the future work may build more carefully [70].

The impact of loading on independent samples and uniformity has not been explored in any other work. The significance of loading without degrading the performance of a reverberation chamber has been addressed in this work. If the cavity has a high modal density (more number of modes per bandwidth) and also high *Q*, the uniformity may still be poor. To improve the uniformity, a small amount of loading can be added to increase the *Q* bandwidth. The increase in *Q* bandwidth permits possible excitation of more modes leading to a better energy distribution among modes. More number of modes does not mean the number of IS has increased. The number of IS actually decreases with loading and if the loading is significant, the number of IS may be too low and also as there is less energy to interact within the chamber leading to poor uniformity.

Further implications towards the impact of loading on IS can also be seen by looking more closely at Tait's approach [16]. Utilizing the measurement of maximum power inside the chamber, the number of IS from the maximum power measurement can be found. From the multiple maximum measurements, the mean and the standard deviation of the maximums will be calculated and the normalized standard deviation (which is the ratio between the standard deviation of the maximums and the mean of the maximums) will be plotted against the number of IS (Ref: Figure 3.2).

$$\text{Normalized SD} = \frac{\text{SD of Max}}{\text{Mean of Max}} \qquad \textbf{(3.4)}$$

When loading is added, the max power received inside the chamber will be reduced as compared to the empty chamber. If the maximum measurement is performed multiple times, the mean of the maximum measurement will also be reduced. As the decrease in power is across all measurement points, we suspect that the impact on SD due to loading will not be significant. Computing the normalized SD from this data, as the mean is reduced, the normalized SD goes up. Following the curve that is plotted in Figure 3.3, it can be seen that the number of IS goes down when loading increases (or with increase in the value of normalized SD). The one draw back of Taits approach is that the maximum value measured inside the chamber is a function of number of measured samples and independent samples. Hence larger the number of measured maximums, the better the estimation will be.

To reduce the uncertainty in measurements, more IS are needed. If loading reduces the number of available IS then it poses a problem at low frequency testing. Methods to increase the number of IS by introducing the second tuner into the chamber are introduced.

3. 4 Analysis with two tuners

This section will examine how to increase the number of independent samples to compensate for the reduction in IS due to loading. To generate more IS, the complexity of the cavity could be increased which may be achieved by introducing corrugations on the wall along with frequency stirring [21] or by increasing the complexity of the present tuner or by introducing a second tuner [22, 15]. This work investigates the option of introducing a second tuner.

The most efficient tuner will be a tuner that is oriented along the largest dimension of the chamber as the low frequency modes will be established in that particular direction [20]. Though establishing a large tuner will be more efficient, it might not always be practically possible to install a tuner along the longest dimensions of the chamber.

When the physical size of a chamber is large, one tuner might not be enough to stir the fields inside the cavity efficiently and a second tuner might be used either parallel or perpendicular to the original tuner [4]. As per the standard, the second tuner must also be electrically large at low frequencies at which the chamber is intended to be operated. The

size of the tuner puts a limitation on the usable volume inside the chamber. Two tuners (one vertical and one horizontal typically) can take up significant portion of the volume inside the chamber which can limit the usable volume. In this study, a small second tuner parallel to the existing vertical tuner and a larger tuner (comparable in size with the vertical tuner) perpendicular to the existing vertical tuner has been introduced in the SMART 80 reverberation chamber at Oklahoma State University and measurements have been performed at various frequencies to analyze the combined performance/influence of the tuners on independent samples.

The small second tuner is made of 3, 2 x 2 feet foam pads covered in aluminum foil, attached in a 'z-fold' fashion and has limited functionality in terms of its operation. The height of the tuner is about 3.5 feet with 2 feet diameter and operated only in the stirred mode and the speed of the motor was not variable (0.8 sec per rotation). The major objective of this study was to check if Tuner 2 was capable of generating more IS when operated along with the vertical tuner. Additionally the location dependence of the second tuner was investigated with the smaller vertical tuner along with its effects on the lowest usable frequency (LUF) of the chamber.

The SMART 80 reverberation chamber was operable at frequencies of 300 MHz and higher with only one tuner present. Measurements were performed for an input frequency 80 MHz to 200 MHz to test the low frequency limit of the chamber. Log periodic antennas were used in these measurements.

Figure 3. 6 Picture of the second tuner

In all further discussions, the existing vertical large tuner will be referred as Tuner 1 or VT and the second small tuner that will be introduced into the chamber will be referred as ST, the bigger second tuner will be referred to as HT. ST was also placed in two different places, one close to the VT (referred as P1) and one away from the (VT referred as P2) to capture the positional dependence of the small tuner if there is any. The first set of measurements was performed to look at the influence of the second tuner on independent samples under different loading conditions. The experimental procedure was same as explained in Section 3.2. Care was taken that the rotational rates of the two tuners were asynchronous. Received power data was collected for one rotation of the vertical tuner (29 sec) while the small tuner rotates at a rate of 0.8 sec per rotation.

Table 3. 6 Independent samples as a function of load and different tuner combinations; f0 = 1 GHz

Frequency = 1 GHz				
Load	**VT**	**VT and ST P1**	**VT and ST P2**	**VT and HT**
No Load	384	533	533	1600
Load 1	238	267	229	1600
Load 2	213	267	267	1600
Load 3	195	200	229	800
Load 4	109	123	145	800

Table 3. 7 Independent samples as a function of load and different tuner combinations; f0 = 2 GHz

Frequency = 2 GHz				
Load	**VT**	**VT and ST P1**	**VT and ST P2**	**VT and HT**
No Load	534	533	800	1600
Load 1	395	400	533	1600
Load 2	368	400	400	1600
Load 3	302	400	533	1600
Load 4	183	229	267	1600

Table 3. 8 Independent samples as a function of load and different tuner combinations; f0 = 3 GHz

Frequency = 3 GHz				
Load	**VT**	**VT and ST P1**	**VT and ST P2**	**VT and HT**
No Load	801	800	800	1600
Load 1	534	533	533	1600
Load 2	464	533	533	1600
Load 3	454	533	533	1600
Load 4	278	400	267	1600

Table 3. 9 Independent samples as a function of load and different tuner combinations; f0 = 4 GHz

Frequency = 4 GHz				
Load	**VT**	**VT and ST P1**	**VT and ST P2**	**VT and HT**
No Load	801	800	800	1600
Load 1	801	800	800	1600
Load 2	587	533	800	1600
Load 3	507	533	800	1600
Load 4	334	400	400	1600

Table 3. 10 Independent samples as a function of load and different tuner combinations; f0 = 5 GHz

Frequency = 5 GHz				
Load	**VT**	**VT and ST P1**	**VT and ST P2**	**VT and HT**
No Load	801	1600	800	1600
Load 1	801	800	800	1600
Load 2	747	800	800	1600
Load 3	747	800	800	1600
Load 4	368	533	533	1600

The measurements were performed with two log periodic in band antennas and the receive antenna was placed at 5 different positions inside the usable volume of the chamber. Maximum number of measured samples (1600) was captured in every run and the independent samples were calculated using the 1/e criterion. The number of IS reported in the Tables 3.6 – 3.10, is the average of IS calculated from 5 different receive antenna positions.

It can be seen that the number of IS goes up with frequency as expected. Introduction of the second tuner seems to improve the complexity of the EME resulting in increase in IS as expected. Irrespective of the position of the small tuner with respect to the vertical tuner, there is an increase in IS. When the large second tuner, HT is operated along with the vertical tuner, with 1600 measured samples, it appears that loading has no effect but that is only because of the sampling limitation in our measurement setup.

With independent samples being a function of measured samples, the number of measured samples needs to be far more than 1600 when both the tuners are operational to effectively capture all the independent samples. In essence, there is an effect of loading on IS. This is critical during testing at low frequencies. A second tuner could be introduced to subdue the effects of loading.

When the chamber is operated in the low frequency regime (below 300 MHz), and only Tuner 1 is operating the modes in the chamber are not stirred efficiently and the measured powers will have positional dependence. The non-complex fields may be due to the inefficiency of the tuner (the small tuner is not sufficiently electrically large or complex) or due to low mode density. If low mode density is the cause then not much could be done as the physical structure of the chamber does not support any more modes. Therefore making the tuner any more efficient may not provide sufficient increase in IS.

When both the tuners are operational, the modes are stirred more efficiently and the energy distribution among the modes should lead to better uniformity. Also the number

of independent samples increases as the number of statistically different mode configurations goes up. By increasing the number of IS at low frequencies, the uniformity might be improved and the chamber might be considered operational (well-stirred). In this study when the IS are reduced due to loading, a second tuner (Tuner 2) was introduced far from the usable volume. The combined operation of the tuners increased the number of available IS compensating for the reduction due to loading.

To investigate if the second tuner pushes the low frequency limit of the chamber further down, measurements were performed for an input frequency of 200 MHz and below. The SMART 80 chamber is capable of performing down to 80 MHz provided both the vertical tuner and the horizontal tuner are operational. In this set of measurements, the low frequency limit of the chamber was tested with only the vertical tuner and when the chamber performance becomes questionable, the second small tuner or the horizontal tuner was brought in and the chamber low frequency limit was tested.

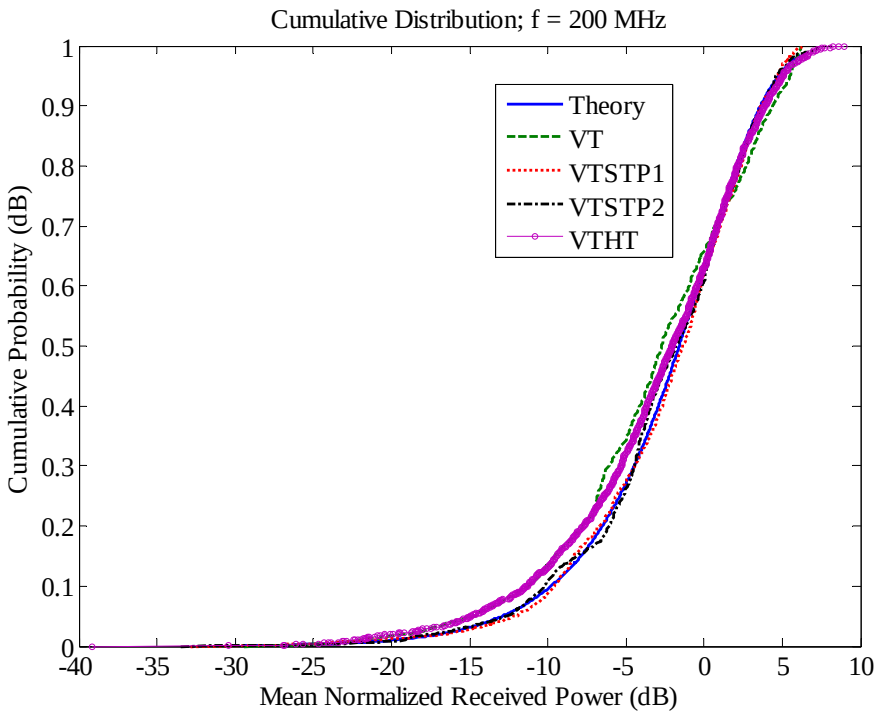

Figure 3. 7 Cumulative distribution plot of SMART 80 at 200 MHz with different operational tuners

The mean normalized received power cumulative distribution plot for the SMART 80 reverberation chamber operating at different frequencies with different tuner combinations are shown in Figures 3.7, 3.8, 3.9 and 3.10. From Figure 3.7 it can be seen that all tuner combinations are reasonably close to the theoretical curve. When the chamber was tested at 150 MHz, the mean normalized received power curve from the operation of the vertical tuner (VT) and the combination of the vertical tuner along with the small tuner placed at position 1 or 2 (VTSTP1 or VTSTP2) seems not to follow the theoretical curve.

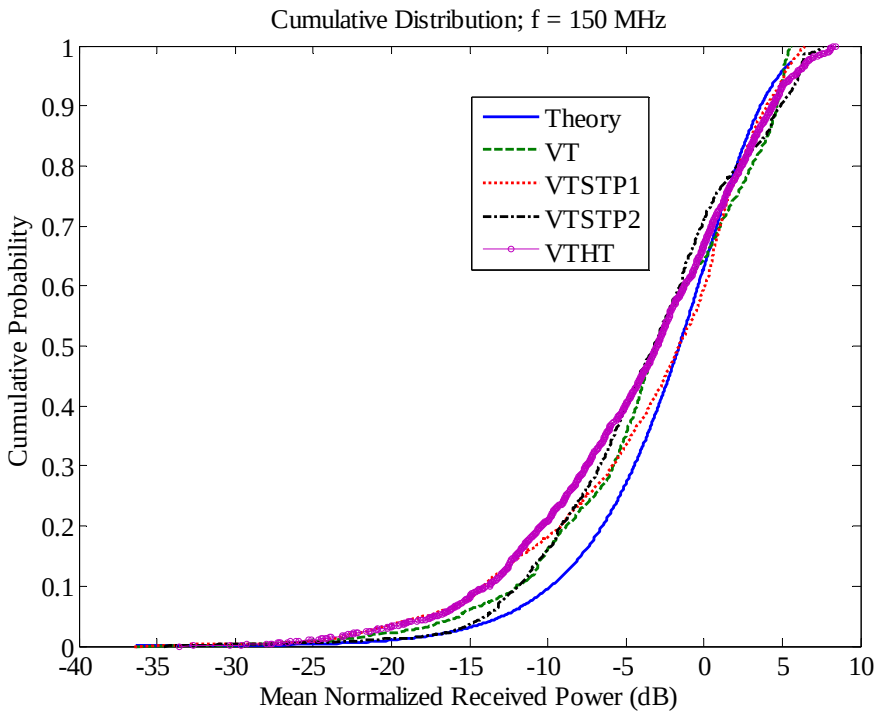

Figure 3. 8 Cumulative distribution plot of SMART 80 at 150 MHz with different operational tuners

When the input frequency is lowered to 100 MHz, the difference is even more apparent. Only the vertical tuner operating along with the horizontal tuner (VTHT) seems to be close to the theoretical curve. This difference is even clearer when the chamber was tested at 80 MHz. The analysis performed in this study clearly indicates that the size of the secondary tuner should be electrically large and possibly comparable to the primary tuner to efficiently stir the fields at lower frequencies.

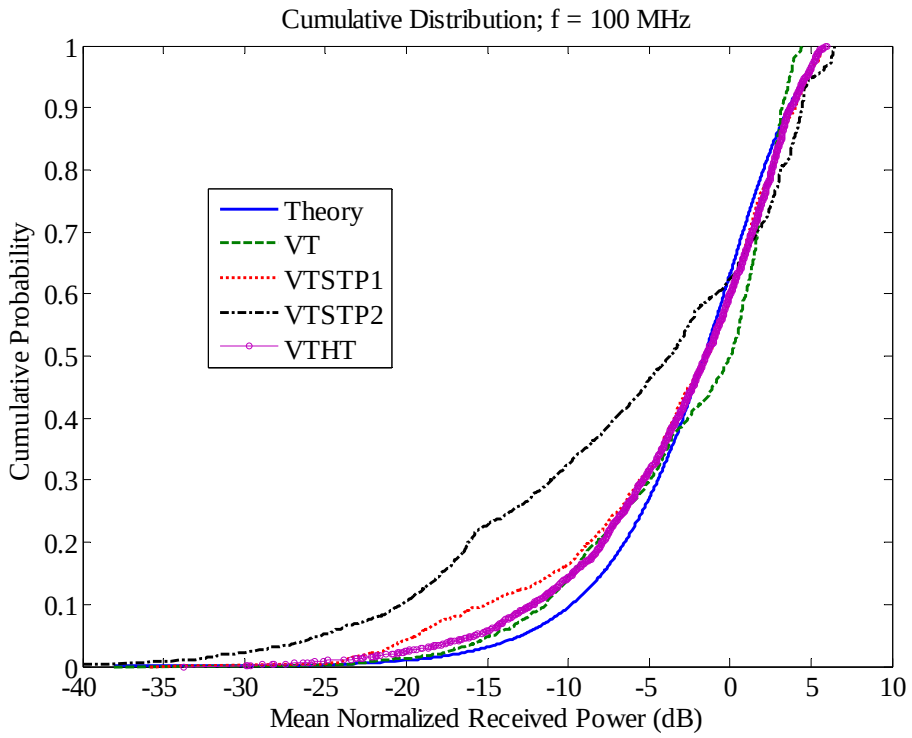

Figure 3. 9 Cumulative distribution plot of SMART 80 at 100 MHz with different operational tuners

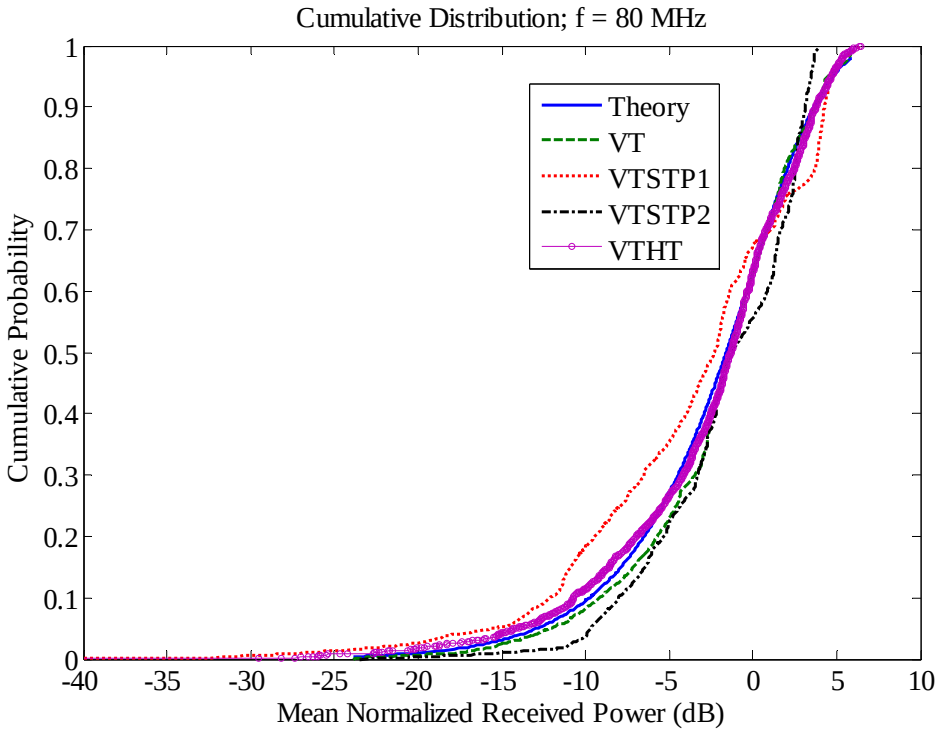

Figure 3. 10 Cumulative distribution plot of SMART 80 at 80 MHz with different operational tuners

In this chapter, the influence of loading on independent samples has been investigated. The uniformity of the chamber might increase with loading provided the cavity has a large *Q*. There is always not a one to one correlation between uniformity, independent samples and loading. We also investigated methods to increase the number of independent samples by introducing a second tuner. The size of the second tuner and its location with respect to the first tuner was also investigated.

In the next chapter, the problem of computing the current induced on a wire located inside a cavity will be introduced. The impact of the wire on the cavity field behavior and the variation of the induced current due to the change in position will be discussed. A method to calculate the measured current from a simple S parameter measurement will be discussed. Measurement and simulation results for the induced current due to the variation in the aperture fields exciting the cavity will be shown.

Chapter 4

4.0 PREDICTION OF INDUCED CURRENT ON A CABLE OPERATING INSIDE A CAVITY AND VALIDATION OF MODEL FIDELITY

There is a need for innovative methods of assessing electromagnetic damage and upset on electronic equipment when the details of the equipment, its enclosure, interconnecting cabling and surrounding geometrical configuration are not well known. Classical methods of electromagnetic analysis are not well suited, because they require geometrical detail which may not be known and probably cannot be known to the precision required by those methods.

Figure 4. 1 Example of cable bundles inside aircraft cockpit

Figure 4.1 is a typical example illustrating the issues to be examined. A complex wiring harness interconnecting a large number of components inside an enclosure susceptible to external EMI is of interest. Even if a particular problem could be modeled in enough detail to support computational electromagnetic simulations, there is not a “particular problem” to simulate! Cable routings will vary, and locations of individual wires within cable bundles are unknown. Further complicating the task is that an understanding of individual component damage/upset levels in such a cluttered environment is not well known. An effort towards modeling failures due to upset and other EMI/C phenomenon will be presented in Chapter 5.

Statistical electromagnetic methods have found applicability to EMI/C and HERO problems in highly reverberant spaces, because rather than being thwarted by the “irreducible uncertainty” of the problem, they use that uncertainty to advantage [33]. In this work the possibility to use the statistical methods to cavities under different mode regimes by deriving new distribution functions is explored.

When the cavity in which complex electronics are located is highly overmoded and electrically large, the RC statistics can be used to determine the extent of the EMI/C problem. Rather than having to find which wire has what current/power in what bundle connected to what components, the detailed geometrical information is disregarded (which cannot be known with certainty anyway) and the focus is on the wire responses as a group via a cumulative distribution function.

Methodologies that will be used to determine how problems can be handled deterministically (using analytical or computational techniques), statistically, or via some hybrid method by splitting them into classes of problems by some quick measurements or estimations, as suggested in Chapter 2 and understanding the limits/issues raised in chapter 3 will be proposed. Deterministic methods will be employed if the problem at hand is simple and statistical methods will be highlighted when the problem is complex as seen in Figure 4.1.

The other challenge that needs to be answered is what details in the problem should be modeled when using computational methods. If every minor detail needs to be modeled then sufficient model fidelity requirements need to be satisfied in order to reduce the overall uncertainty in the problem. When computational methods are used, the modeling should be established in such a fashion that the modeling is general and is not particular about the fine details.

The focus of this work will be on developing the guidelines that will be used to *optimize* the decision-making process regarding the application of deterministic and/or statistical methods as well as assist in making intelligent decisions with respect to the required model fidelity, thus providing an answer to the questions: How much detail is necessary to assure accurate predictions and reduce problem uncertainty? What methods are best suited to predicting the probability of failure? A statistical approach will further help establish trends and bounds that will be used to guide the generation and analysis of the models.

For the development of the guidelines resulting in a well-defined process for predicting bounds on random EMI/C effects for avionics compartments, bays or cavities containing equipments and interconnect cables, a simple and small 30x12x30 cm cavity out of aluminum was built and measurements and simulations were performed at different frequency ranges. The methodology based on these guidelines will ultimately dictate model fidelity requirements for the appropriate application regime. Statistical methods, in conjunction with numerical techniques, will dictate what detail is dominant or has the most impact. Statistical methods will be used to determine trends and obtain bounds on the solution in view of the random variables inherent in the problem. This includes variability due to probe placement or orientation with respect to the cavity geometry, including proximity to other probes, surfaces, internal cavity structures.

The study also investigates how the distributions change as a function of excitation frequency, cavity mode, and more complex aperture models. Following this initial discussion, more complicated overmoded cavities will be analyzed while closely examining the EM phenomena occurring at/near interior metallic walls and surfaces representing cables for example. Ultimately, the complications and complexities will arise due to the variability of cavity fill, existence of multiple apertures of various types, EM source characteristics, near-field proximity effects, and so forth. Though all these variations will not be implemented in this work, a methodology will be developed to address the changes that might occur due to the variation of the random variables.

It will be determined that for a large class of problems, whether it will be safe to use statistical methods in particular, for problems that are electrically large, highly complex and overmoded. For problems that are not electrically large, not geometrically complex and not overmoded, whether numerical tools may be suitable and statistical methods may be applied to bound any computational or statistical uncertainty due to system-to-system variations. Though this work will not completely address all these issues, emphasis will be laid on utilizing the statistical methods for a large class of problems.

The first task that was undertaken was to examine the probability distribution of fields/power close to the walls, corners, and other surfaces of cavities both experimentally and through computer simulations [3]. The relatively simple cases that were modeled show that the expected chi-squared behavior for the power distributions was preserved. Some of the measurements and simulations also suggest that the EM phenomenology and effects as we approach the interior surfaces get complex and may involve complex statistics for analysis. A thin wire was placed inside the cavity and then measurement and simulations were performed to examine the impact of the victim wire on the cavity field distribution.

The underlying issue to be addressed in this research effort is related to determining when and under what conditions one would apply a deterministic approach versus a statistical approach in order to solve certain avionics enclosure EMI/C problems. Fundamentally, the goal is to develop support for a methodology that will guide an engineer towards the selection of the appropriate modeling method or measurement method and then to

determine how much model detail will be necessary to reduce uncertainty and bound the range of confidence using simple measurements.

4. 1 Distribution of power close to the wall

The statistical distribution for power and fields are well established when the measurement point is located inside the usable volume of the chamber i.e. away from the cavity walls and any other metal contacts. What is of interest in our effort is to look at the distribution of power or fields or current close to the walls. Lehman's work [3] indicates that a monopole on a ground plane continues to satisfy a mean normalized received power distribution that can be considered Chi-squared with two degrees of freedom. Some measurements and simulations were performed to verify the claims in [3]. The details of the measurements and simulations are discussed below.

4. 1. 1 Measurements

A monopole resonant at 1.4 GHz with a ground plane as shown in Figure 4.2 is used as the receive antenna (S_{11} of the monopole antenna is shown in Figure 4.3) inside a reverberation chamber and the chamber is excited using a CW signal at the resonant frequency. A dual ridge waveguide horn antenna with a wide bandwidth is used as the transmit antenna. Received power as a function of tuner position was measured using the VNA (S_{21}). The vertical tuner was rotating at a speed of 29 sec/rotation hence the sweep

time was maintained to be 29 sec. A maximum number of available measurement points (1601) are collected in every experiment.

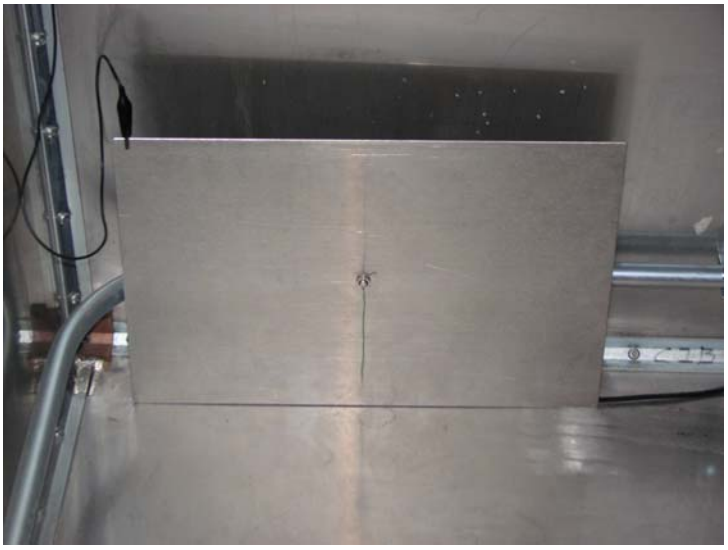

Figure 4. 2 Picture of a monopole on a ground plane located at a corner of the reverberation chamber

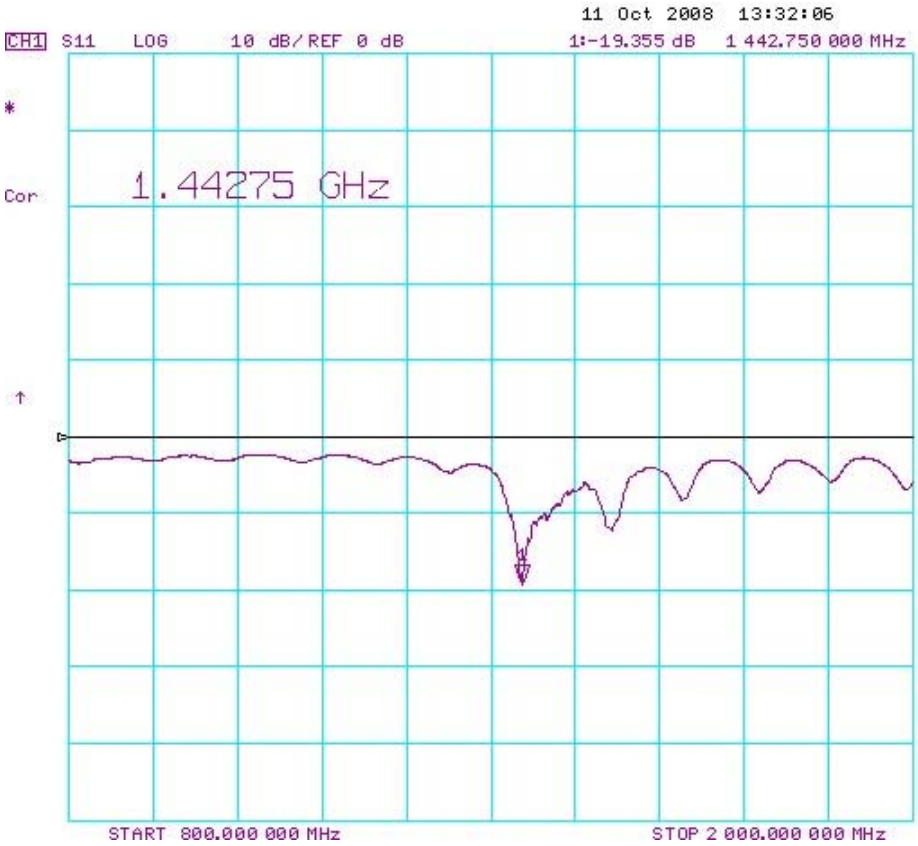

Figure 4. 3 Measured S11 of the monopole resonant at 1.4 GHz

Initially, another dual ridge waveguide horn antenna was used as a receive antenna to provide a baseline for comparison. The transmitter was placed at one of the corners of the chamber and the receiver was placed at the center of the chamber and at least a meter away from the floor. S_{21} was measured as a function of tuner position. The 1601 measured samples were analyzed by Expert Fit (Version 7.0), a statistical distribution fitting software. The software automatically specified and ranked probability distributions, and then described whether the "best" candidate distribution was actually a good representation of the data. In the case for an overmoded cavity it is well known that the received power should follow a Chi-Square distribution with 2 degrees of freedom [4]. This distribution is also represented by a Weibull distribution with a shape factor of 1.

In the Appendix 1, the first three distributions that expert fit fits the data to for all cases has been presented. As can be seen with the horn antenna the Rank 1 distribution is a Weibull with a shape factor of 1 indicating the data follows as Chi-Square with 2 D.O.F distribution as expected.

A quantile-quantile (Q-Q) plot is used to see if a given set of data follows some specified distribution. The Q-Q plot should be approximately linear if the specified distribution is the correct model. The Q-Q plot is constructed using the theoretical cumulative distribution function, F(x), of the specified model and is helpful in bringing out the comparison between the distributions at the tail which is critical when working with overmoded cavities (esp. Reverberation chambers).

MATLAB was used to generate the parent distribution data from the statistical parameters calculated using expert fit for the power (Chi-Sq) and field distributions (Chi). An example of the Q-Q plot is provided in Figure 4.4. The line represents the parent distribution and the '+' represents the measured data as compared to the parent distribution. It can be observed from the QQ plot that the comparison is quite good.

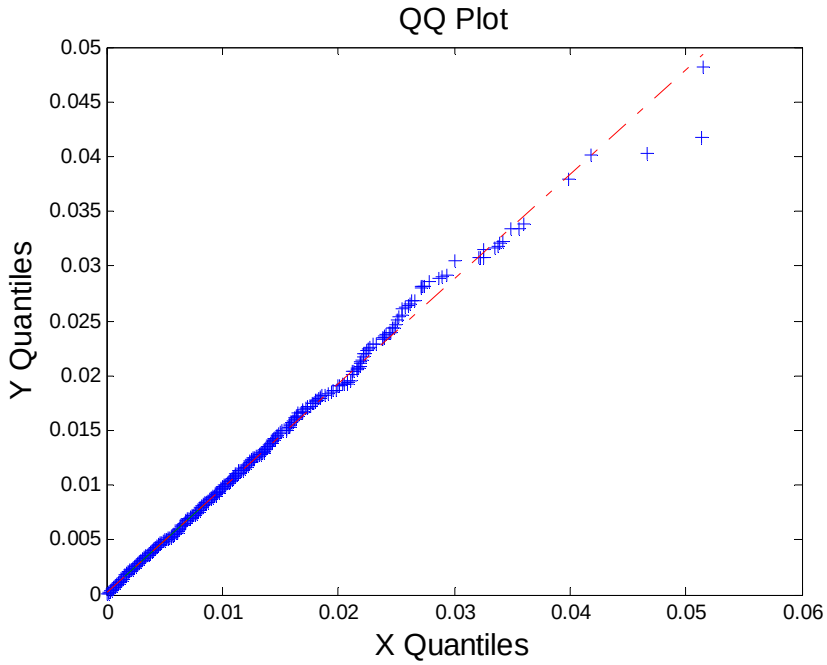

Figure 4. 4 QQ plot for a Chi Square with 2 D. O. F distribution

This procedure was repeated for the monopole receiver antenna when the antenna was placed at the geometric center of the wall (similar to Lehman's work). Then the antenna was placed such that the antenna was close to one of the walls and then finally moved to the corner of the cavity. Note: the ground plane of the antenna is connected to the chamber walls (represents the antenna just protruding from the wall while the wall serves as a ground plane). The results for various antenna configurations are shown in Figure 4.5.

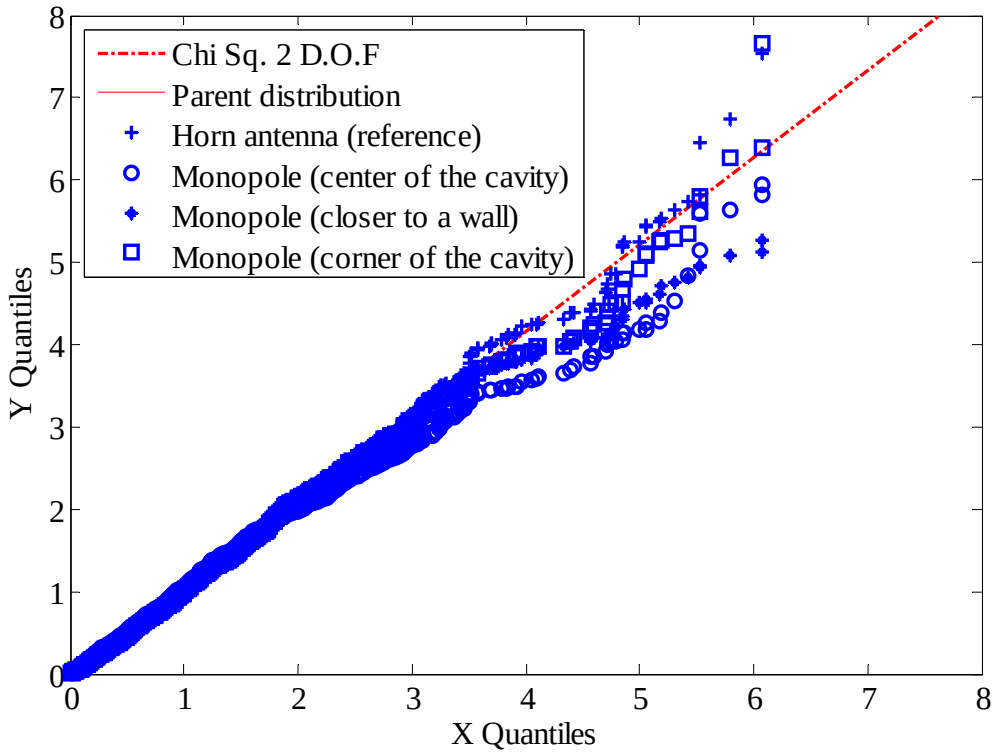

Figure 4. 5 QQ plot for a measured vs. theoretical distribution of power

Figure 4.5 suggests that the Chi-Square behavior of received power is maintained even when placed close to the walls. From the power measured, E field can be calculated using eqn (4.1) [23]. The statistics of E field when the antenna is placed close to the wall is verified in this analysis.

$$< E_Z{}^2 >= \frac{640\pi^2}{\lambda^2} < P_r > \qquad \textbf{(4.1)}$$

From reverberation chamber theory, it is known that the component of the E field will follow a Chi distribution with 2 D.O.F. A Chi distribution with 2 D.O.F can be represented by a Weibull distribution with a shape factor of 2. The calculated E field data were analyzed using Expert Fit as like the measured power. A similar QQ plot is generated using the same procedure explained before with a parent distribution of Chi

with 2 D.O.F. E field Q-Q plot for various antenna configurations are shown in Figure 4.6

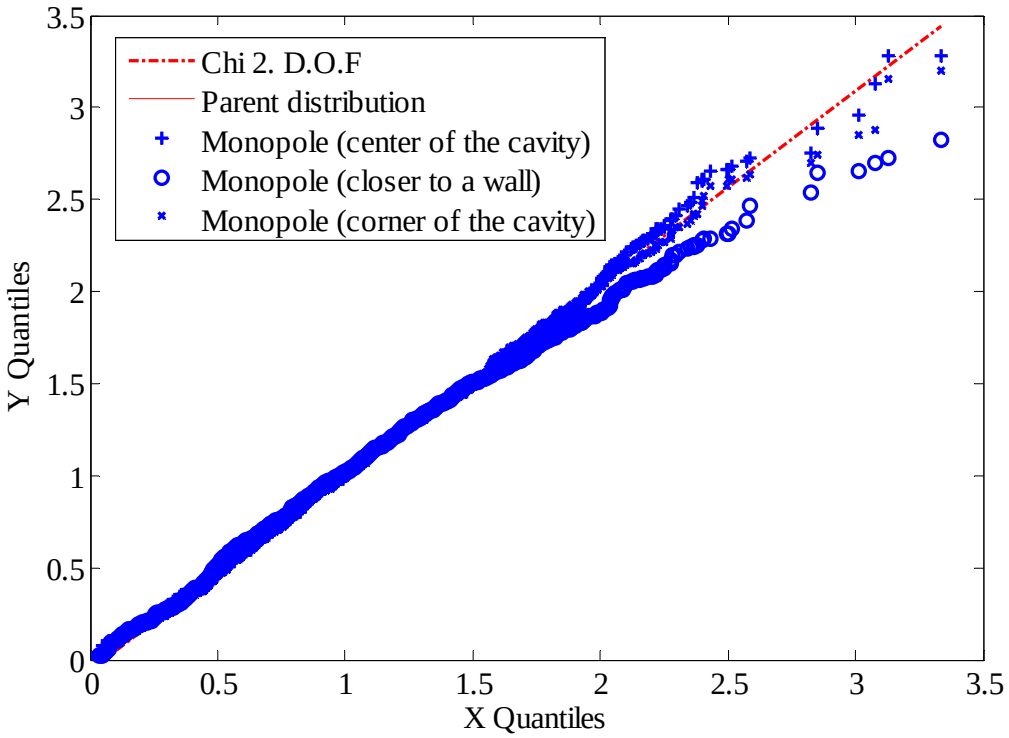

Figure 4. 6 QQ plot for a measured vs. theoretical distribution of E field

Figure 4.6 shows that for different antenna configurations inside the overmoded cavity, the measured E field follows a Weibull distribution with a shape factor of 2. It can be concluded from the above mentioned analysis that the Chi-Square behavior of the received power and Chi behavior of the E field is retained even when the antennas are placed close to the walls of an overmoded cavity. Though the agreement between the parent distribution and the measured data were good at the smaller quantiles, the deviation at the higher quantiles was apparent. Simulations were performed in MATLAB to address the issue.

4. 1. 2 Simulations

MATLAB was used in generating random data to fit to the parent distributions. Though the power followed a Chi-Square distribution and E field followed a Chi- distribution, the underlying distribution of magnitude and phase (in case of power), real and imaginary (in case of E field) follows a normal distribution. Hence random samples of a normal distribution were generated using MATLAB and the E field and power were calculated from that data for statistical analysis.

Three sets of random data were generated to examine the variance just between the random sets. These are represented as 1-power, 2-power, 3-power, 1-efield, 2-e field and 3-efield in Appendix 2. The generated data was analyzed using Expert Fit and as expected, the power follows a Weibull distribution with a shape factor of 1 and the E field data follows a Weibull distribution with a shape factor of 2. From the QQ plots it can be seen that the same amount of deviation between the simulated and theoretical data exist at the higher quantiles as seen in the comparison of measured and theoretical data. The deviation could be because of the statistical sampling uncertainty.

To summarize, the Chi-Square behavior of received power and Chi behavior of E field seems to be preserved when the antenna is moved close to the walls for an overmoded cavity. An examination of undermoded cavities will be explored in the following sections.

4. 2 Modal structure study

To investigate the effect of mode density on the distribution of current coupled to the cable and field and power measurements inside the cavity, more simulations and measurements were performed on a smaller cavity. An aluminum cavity of internal dimensions 30x12x29.5 cm was manufactured with an aperture (15x6 cm) on the front wall of the cavity. In both simulations and measurements, a plane wave was incident at the front wall of the cavity and the field at the center of the cavity was measured. Then a probe of known dimensions was introduced into the cavity. The probe was connected to the bottom wall through a feed through SMA connector which provided access to connect measuring equipments to the probe.

Firstly a modal structure study of the cavity was performed. The modes that are supported by the physical structure of the cavity and mode density (which could be defined as the number of modes per bandwidth) are of importance to analyze the electromagnetic environment that could possibly exist in the rectangular space. Coupling into and out of the cavity occurs through probes or holes. The coupling probes and holes (of any shape) can be located on any of the walls of the cavity. The resonant modes of the rectangular cavity can be derived by solving for the modes that the transverse electric or transverse magnetic to one of the three axes. The cut off frequency for a rectangular cavity is given by eqn. (4.2).

$$f_{mnp} = \frac{1}{2\pi\sqrt{\mu\varepsilon}}\sqrt{\left(\frac{m\pi}{a}\right)^2 + \left(\frac{n\pi}{b}\right)^2 + \left(\frac{p\pi}{c}\right)^2} \qquad \textbf{(4.2)}$$

Where *m*, *n* and *p* are the mode indices and *a*, *b* and *c* are the length width and height of the cavity respectively. The apertures and probes are not considered when calculating the modal structure of the cavity.

The modal structure for an empty cavity (dimensions: 30x12x30 cm) is shown in Figure 4.7. Each line represents a mode that is present at that particular frequency. The Y axis is left empty as amplitude for a mode would not mean anything.

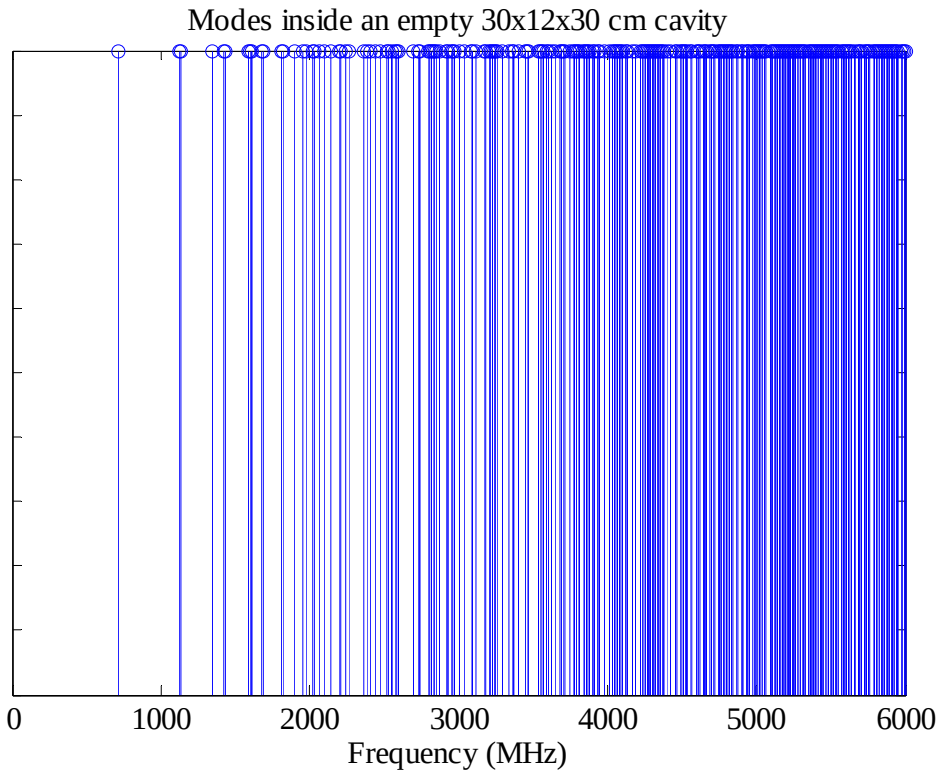

Figure 4. 7 A plot of modes inside a regular rectangular cavity (30 x 12 x 30 cm)

The first mode for the empty cavity occurs around 700MHz. As expected, the modal structure for the low frequencies is sparse but that quickly changes as the frequency increases leading to a complex cavity at high frequencies. As two dimensions of the cavity are the same (Length and Height = 30 cm), there exists some degenerate modes

(modes that have the same resonant frequencies) and also gaps in modal structure which can be seen in the Figure 4.7.

Some assumptions are made to classify the mode regimes. The assumptions are as follows, the first mode inside the cavity is excited around 700 MHz. The frequency window between 0 and 700 MHz will be called a no mode condition as the physical structure of the cavity itself does not support any modes. In the window between 700 MHz and 1.4 GHz, the structure supports about 5 modes and this could be called as an undermoded regime. In the window between 1.4 and 1.5 GHz, more modes are excited. Along with the previously excited modes, the cavity transitions to an moderately moded regime. Above 1.6 GHz there exists more modes are excited and this will be referred to as the overmoded regime.

The cavity is considered to be reverberant if the number of modes that are excited at any particular frequency is large and there exists a high mode density i.e. there is not a significant gap between adjacent modes. There are several rules of thumb in the reverberation chamber community to determine at what frequency the cavity starts to be reverberant which varies any where from 10 modes to 100 modes (in mode count) and $3f_0$ to $6f_0$, in terms of frequency with f_0 being the cutoff frequency (resonant frequency of the first mode). The cavity of Figure 4.7 could be reverberant from 1.6 GHz. If the cavity is established to be reverberant, then RC statistics could be used to analyze the field structure. By separating the problem into three parts as undermoded, moderately moded and overmoded, separate statistical distributions can be discussed.

For a regular three dimensional cavity, field strength on the modes excited in the cavity and the measured field depends the spatial location of the antenna or probe. Interesting tasks here are to determine the perturbation the field structure inside the cavity by a small wire used for measurements. The impact of the wire for different modal environment will be studied in detail. The impact of the physical location of the wire with respect to the modal structure existing inside the cavity will be discussed. Also by varying the excitation frequency of the cavity, the mode density can be varied from an undermoded cavity to a overmoded cavity which will be convenient in both measurements and simulations.

The aperture size was initially chosen to be 15x6 cm and a '*y*' polarized plane wave source was incident on the front face of the cavity. An illustration of the cavity with an aperture and a plane wave source is shown in Figure 4.8. The field at the center of the cavity was calculated using different simulation packages such as FEKO and an OSU code based on moment method code with multi level fast multipole algorithm (MLFMA). The shielding effectiveness (SE) of the box was calculated from the field measured at the center of the cavity. The SE of the cavity for a frequency range of 100-1000 MHz computed using FEKO and MLFMA are compared as shown in Figure 4.9. The SE of the cavity is least at a frequency 620 MHz. The self resonance of the cavity aids in better coupling of the fields from the outside through the aperture.

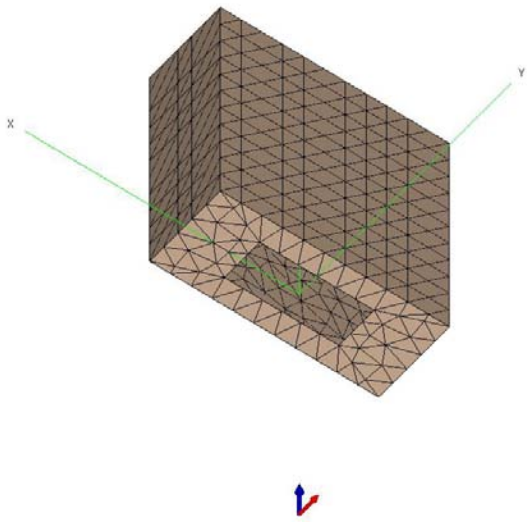

Figure 4. 8 Illustration of rectangular cavity with rectangular aperture incident by a plane wave

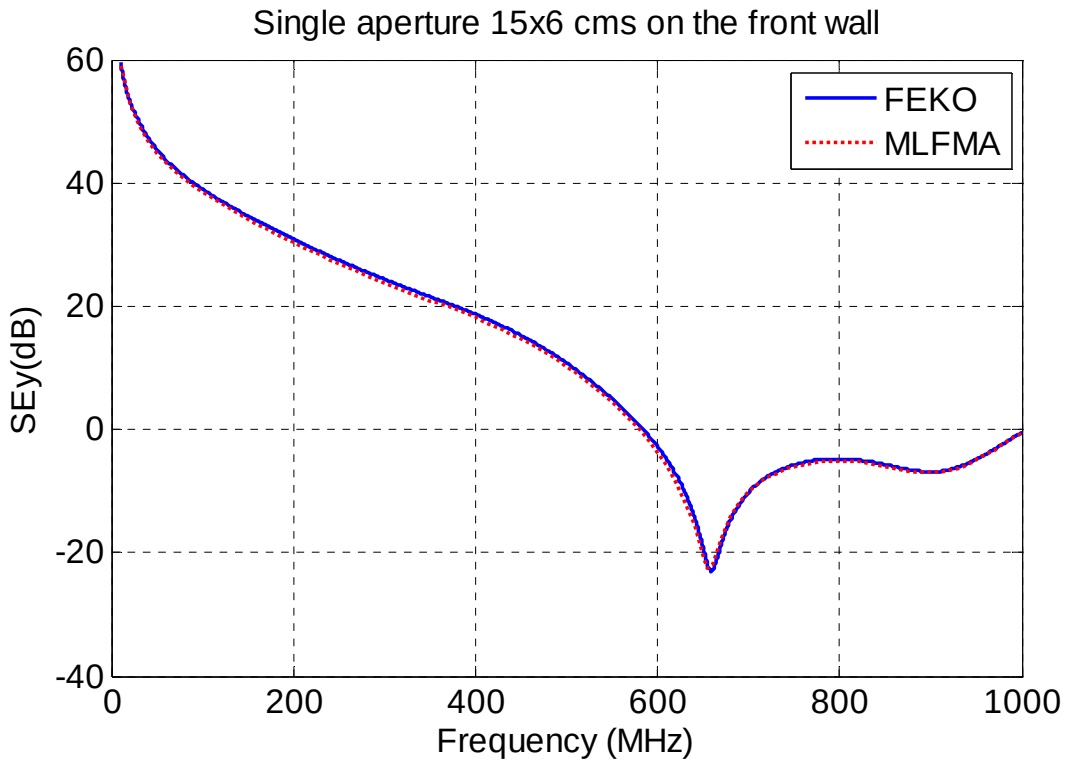

Figure 4. 9 Shielding effectiveness of the (30 x 12 x 30) cavity with (15 x 6) aperture

From the comparison it is clear that the codes available will be suitable for analyzing these problems at least in the frequency ranges specified above. To validate the simulation results, measurements need to be performed on the cavity. Measuring the fields at the center of the cavity is problematic. An E field probe can be used to measure

the field but the physical structure of the probe was sufficiently so significantly affects the EME of the cavity. Hence the analysis was refocused on simulating an observable that is also measurable.

In order to do this, a wire of length 10.5 cm was introduced into the cavity as explained before and the impact of the wire on the field distribution inside the cavity was calculated using simulations. The wire was placed at 16 different positions inside the cavity. As the source was *y*-polarized, the longest dimension of the wire was along the width of the cavity to enhance maximum coupling. The 16 different positions of the wire are intersection of grid points on the bottom plate of the cavity as shown in the Figure 4.10. The field was calculated at a point away from the bottom plate of the cavity as shown in Figure 4.10.

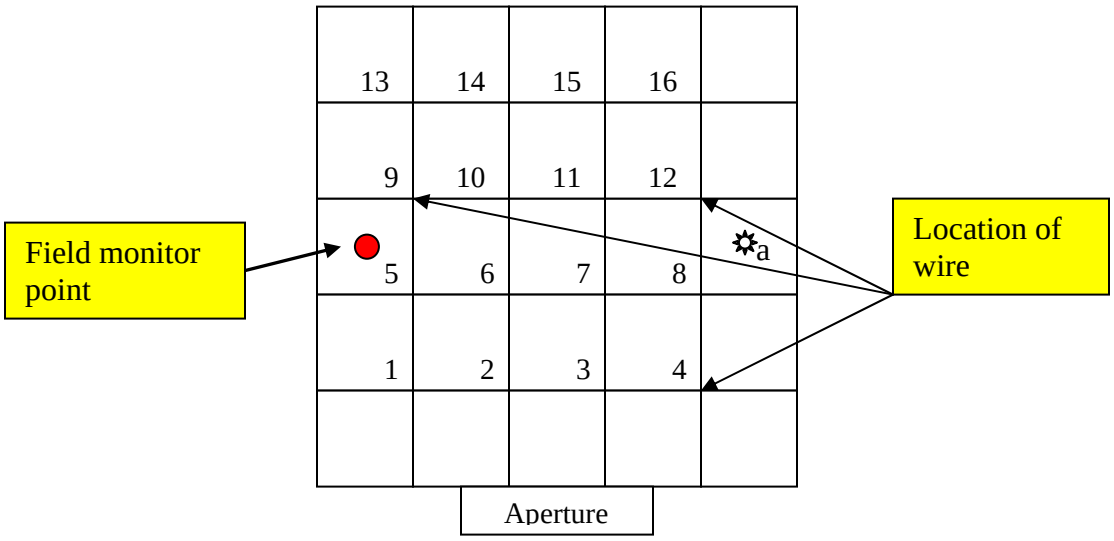

Figure 4. 10 Sketch of the locations of the probe on the bottom plate of the cavity and field monitor point

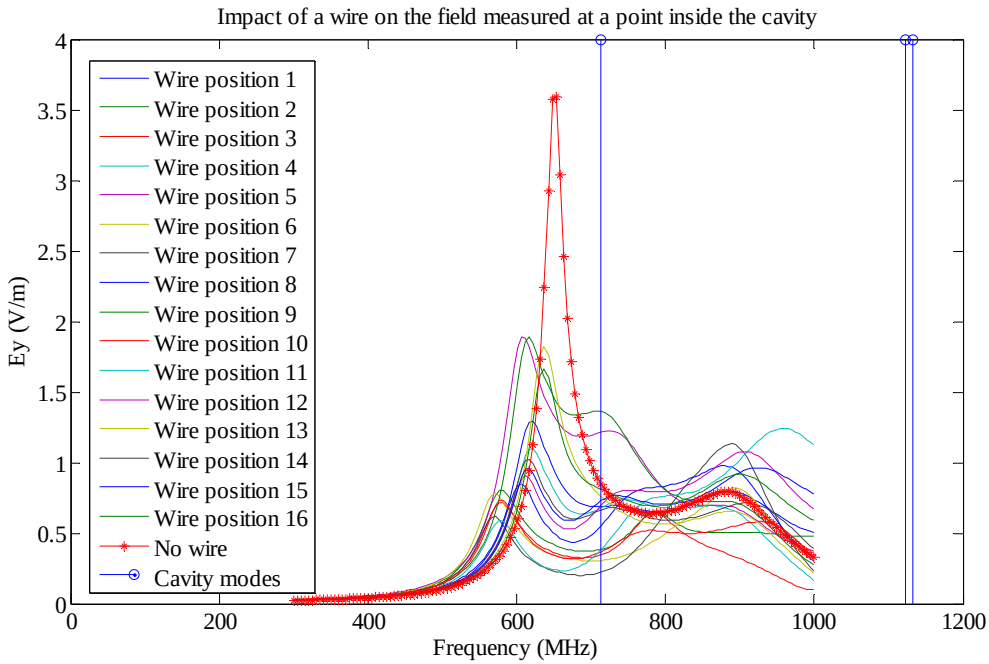

Figure 4. 11 Impact of the wire on the field computed inside the rectangular cavity

From Figure 4.11, it can be seen that the presence of the wire does affect the field measured at a point inside the cavity irrespective of the position of the wire. The reduction in amplitude of the field measured when the wire is present is a strong indication that the wire absorbs energy present in the cavity. The empty cavity modes (with no inclusion of apertures and wires) are also plotted on the same graph to see how the field varies as the modal structure improves. The variation of the field for different locations of the wire is somewhat predictable when the mode density of the cavity is low but soon the variations are significant as the mode density becomes complex. Though the field values calculated at a point is useful in analyzing the field structure inside the cavity, measuring the field without any perturbation is impossible hence some measurable like the current on the wire that can also be simulated was chosen for further analysis,

To measure the current on a cable bundle, typically a current probe is placed around the cable bundle. If this procedure is followed in the measurements, the physical structure of the current probe is large enough that it will affect the modal structure of the cavity. One must measure the current on the wire without altering the EME that exists inside the cavity with a wire and a plane wave incidence. Hence alternative methods need to be used to measure the current. In this work, the current at the end of the wire where it is attached to the bottom plate of the cavity is measured using a simple S parameter measurement closely following work by Breakall [24]. This measurement and simulation procedure is explained below.

4. 3 Current induced on the wire located inside the cavity due to an excitation outside

4. 3. 1 Simulation

The source is a plane wave incident upon the front face of the 30x12x29.5 cm cavity with a 15x6 cm aperture. A wire of length 10.5 cm is placed at one position inside the cavity such that direct illumination from the source is avoided (x=-11.25, y=-0.06 and z=.12 – Point ‘a’ in Figure 4.10). The wire is connected to the bottom plate directly (imitating a short circuit). The plane wave is incident at normal angle of incidence and the input frequency is varied from 300 MHz to 1 GHz in 5 MHz steps. The wire is divided into 8 segments and the current at the bottom most segment where it is connected to the plate is of computed as this would be the quantity that can be measured without the use of a current probe around the wire.

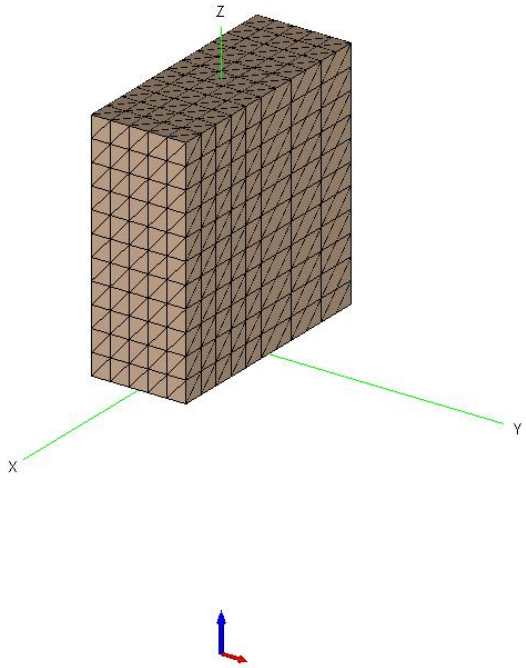

Figure 4. 12 Simulation setup to compute the current on the wire located inside the cavity

4. 3. 2 Measurements (Open air)

The measurements are performed on the 30x12x29.5 cavity with a 15x6 aperture made of aluminum. The source was a log periodic antenna (250 MHz to 2 GHz). A hole was drilled at the bottom plate of the cavity (Point 'a' on Figure 4.10) where the probe was present and the 10.5 cm probe was attached through a SMA connector. The measurements were performed with an 8753ES vector network analyzer (VNA) for the frequency ranges of 300 MHz to 1 GHz. The box and the transmitter antenna were separated by a distance of 1 m (tip of the transmitter antenna to the front face of the box). The transmit antenna was connected to port 1 of the VNA and the probe inside the box was connected to the port 2 of the VNA using low loss cables. Calibration was performed from the end of the low loss cables connected to the VNA. All the scattering parameters

(S parameters) were recorded when the source was swept from 300 MHz to 1 GHz. The number of points recorded in the span was 201 (VNA limitation).

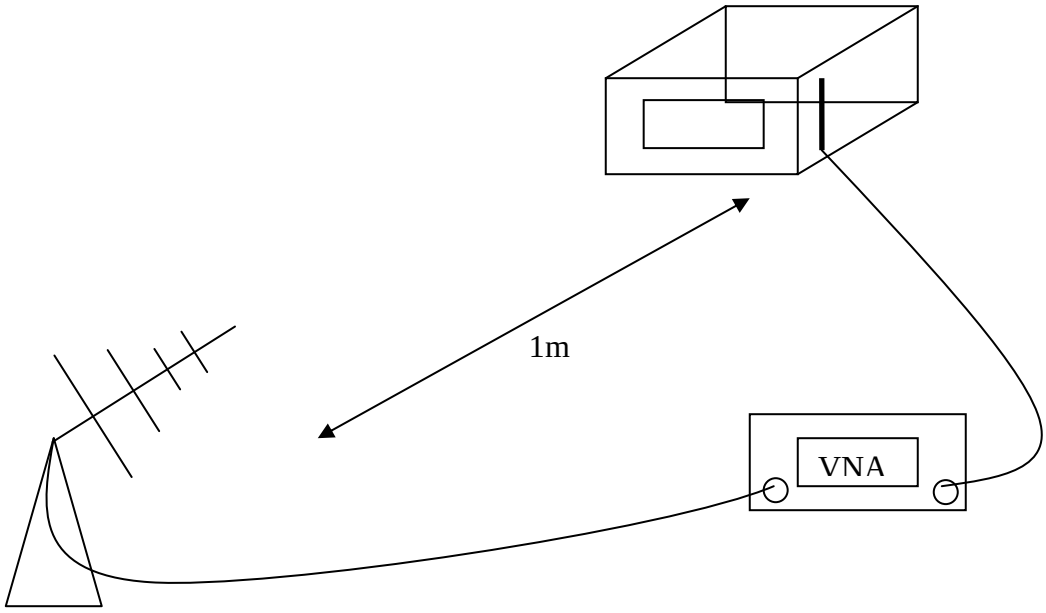

Figure 4. 13 Measurement setup to compute the current on the wire located inside the cavity

The measured reflection coefficients of the source antenna (log periodic) and the wire located inside the cavity for the frequency band of interest is shown in Figures 4.14 and 4.15 respectively. Figure 4.16 is the measured transfer function between the source and the wire antenna. Lower reflection coefficient values at multiple frequencies shown in Figure 4.14 ensure that the source antenna is a broad band antenna suitable for the measurements. The wire antenna present inside the cavity is not broad band and has lower reflection coefficient values at the box resonances implying that the wire antenna is better matched at the resonance frequencies of the box as shown in Figure 4.15. Figure

4.16 shows that the maximum coupling occurs at the box resonances (where the wire antenna is also better matched).

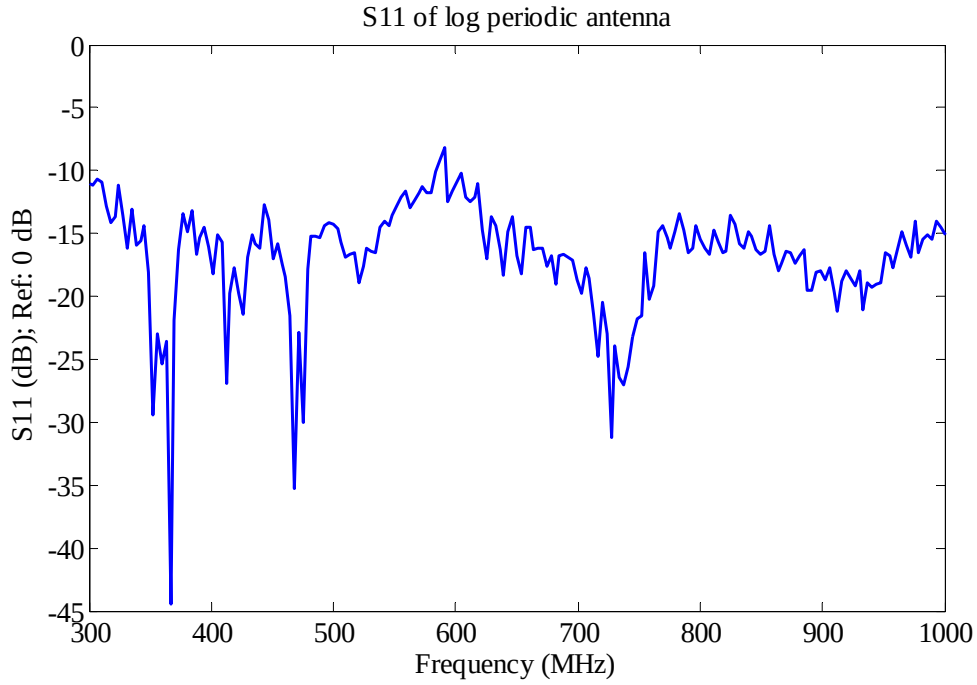

Figure 4. 14 Measured reflection co-efficient of the source antenna

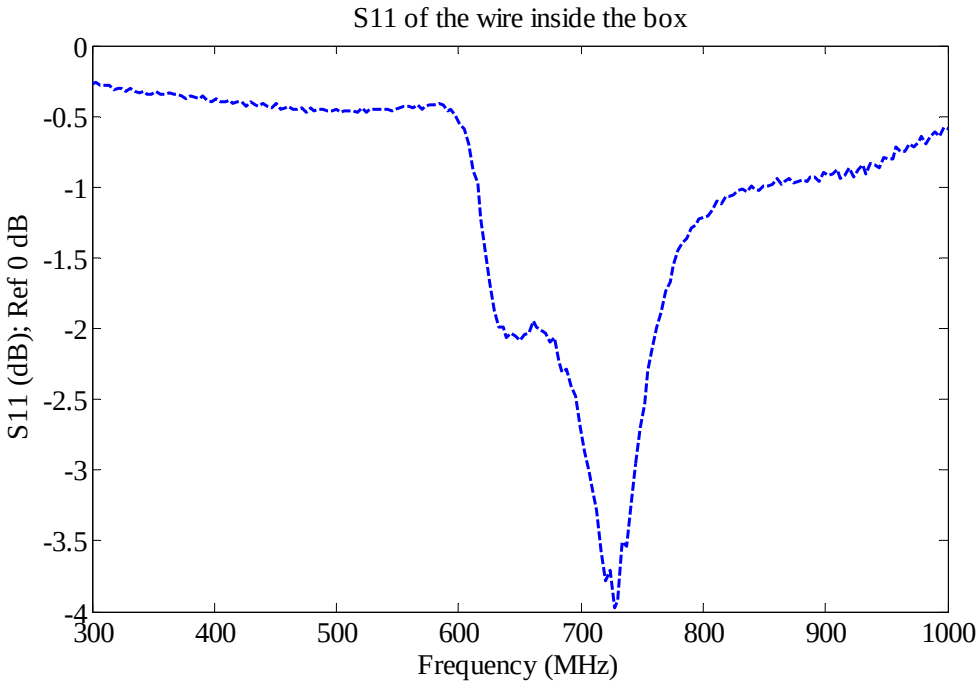

Figure 4. 15 Measured reflection co-efficient of the wire located inside the cavity

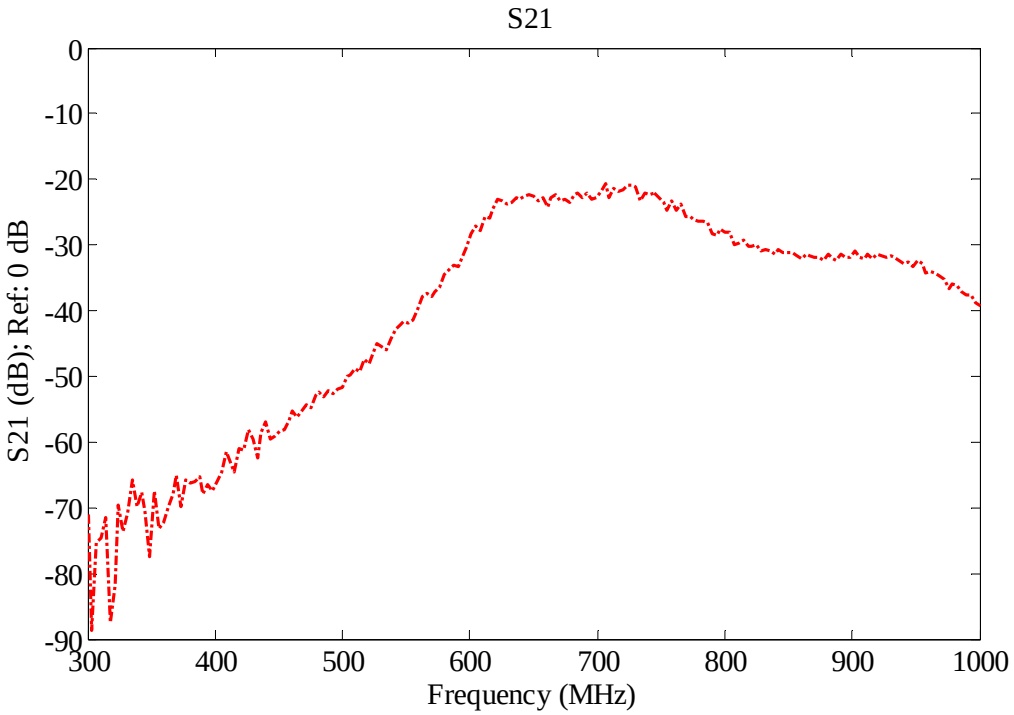

Figure 4. 16 Measured transfer function between the source antenna and the wire located inside the cavity

The current at the bottom segment is calculated using the procedure detailed in [24]. The self impedance of the wire that is connected to the bottom plate of the box is calculated using

$$Z_w(f) = \frac{1+\Gamma_w(f)}{1-\Gamma_w(f)} \cdot Z_0 \qquad \textbf{(4.3)}$$

Where Z_w is the self impedance of the wire, Γ_w is the reflection coefficient of the wire measured while it is present inside the box and Z_0 is the characteristic impedance (50 ohms). A plot of the computed impedance is shown in Figure 4.17.

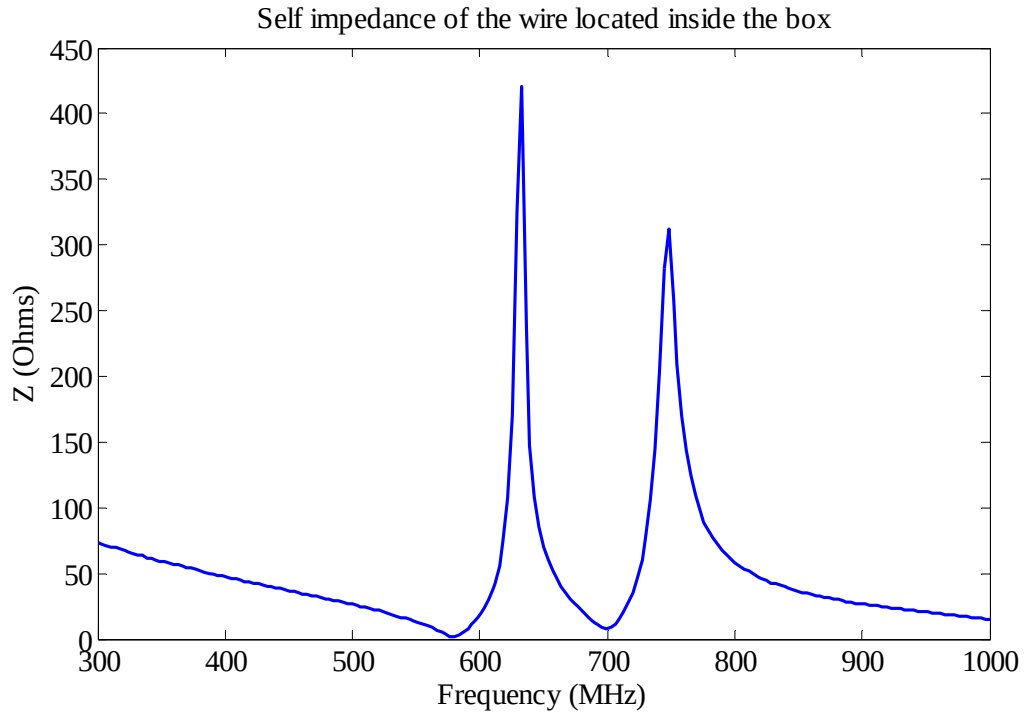

Figure 4. 17 Self impedance (calculated) of the wire located inside the cavity

From the self impedance of the probe and the voltage that is developed at the gap, the current at the bottom of the wire can be calculated. This can be represented by realizing an equivalent antenna circuit model shown in Figure 4.18.

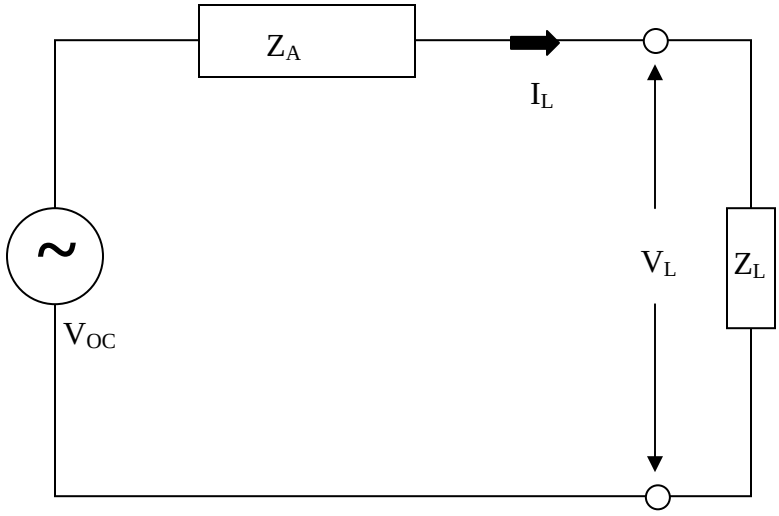

Figure 4. 18 Circuit model for the wire antenna to calculate current

V_{OC} is the open circuit voltage that is developed at the bottom of the wire due to the incident field. I_L is the load current that is developed while Z_L is the load impedance (50 Ohms) and Z_A is the self impedance of the wire. The short circuit current is calculated by

$$I_L = \frac{V_L}{Z_L} = \frac{V_{OC}}{Z_A + Z_L}$$

$$V_{OC} = \frac{Z_A + Z_L}{Z_L} \cdot V_L \quad \textbf{(4.4)}$$

$$I_L = \frac{V_{OC}}{Z_A + Z_L^{'}} = \frac{Z_A + Z_L}{Z_A + Z_L^{'}} \cdot \frac{V_L}{Z_L} \quad \textbf{(4.5)}$$

$$Z_L^{'} = 0 \; ; \; Z_L = 50$$

$$I_{SC} = \frac{Z_A + 50}{Z_A \cdot 50} \cdot V_L \quad \textbf{(4.6)}$$

V_L (load voltage) is the measured S_{21}. A comparison of the measured and simulated current at the bottom segment of the wire is shown in Figure 4.19. From the comparison, of the measured and simulated short circuit currents, it can be seen that both the resonant peaks are captured. The first resonant mode of the empty cavity (with no apertures and wires) is around 650 MHz and the lambda/4 resonance (harmonics of the resonant frequency) of the 10.5 cm monopole occurs around 715 MHz. Both the trends have been captured in our simulations and measurement.

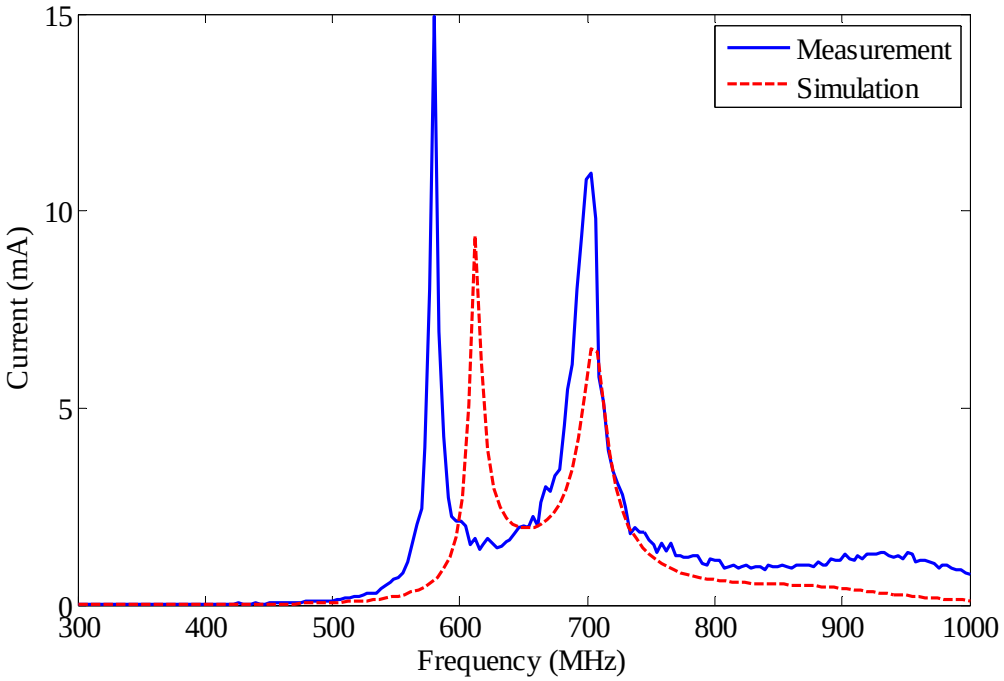

Figure 4. 19 Measured and simulated short circuit current on the wire located inside the cavity

From the short circuit current eqn. (4.6), the impact of the self impedance of the probe on the current that is induced on the probe can be seen. The small variation between the measured and simulated results can be attributed to the limitation of the construction of the box and the length of the wire that is being simulated.

In the calculations, the gain of the transmitter has been assumed to be 1 across the frequency band. The difference in amplitude could be reduced gain of the transmitter antenna is taken into account.

4. 3. 3 Adding arbitrary impedance to the wire

If the wire is terminated not by the VNA port but some other impedance $Z_L^{'}$, then the load current can be calculated using eqn. (4.7)

$$I_L = \frac{V_{OC}}{Z_A + Z_L^{'}} = \frac{Z_A + Z_L}{Z_A + Z_L^{'}} \cdot \frac{V_L}{Z_L} \tag{4.7}$$

The short circuit current is a special case eqn. (4.7) when $Z_L^{'}$ is zero. Hence from the measured S_{21} values, the current at the bottom of the wire when it is terminated by any arbitrary impedance value can be calculated using eqn. (4.7). As an example, currents predicted for 5 different impedances are plotted in Figure 4.20.

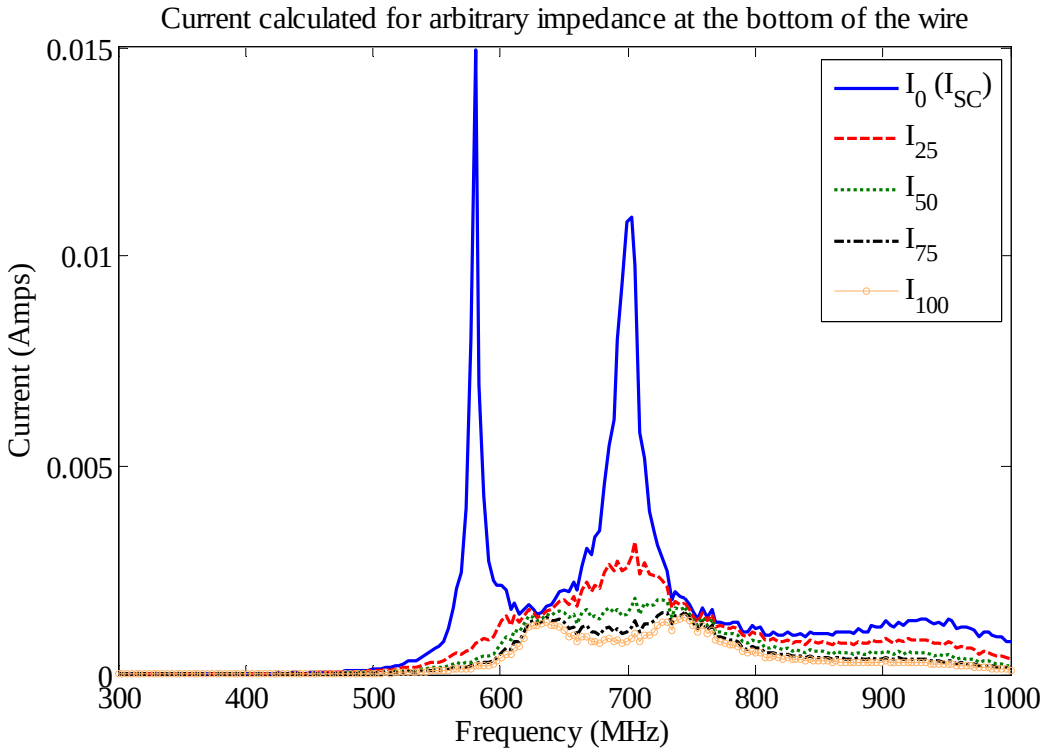

Figure 4. 20 Measured (Isc) and calculated current on the wire terminated by arbitrary impedance located inside the cavity

Observing Figure 4.20, it can be seen that, when an additional load is attached to the bottom of the wire, strong resonances that can be seen in the short circuit case is not seen anymore. The first resonance is not seen at all while the second resonance is decreasing in its amplitude as expected. The same situation was simulated with a 50 Ohm load at the bottom of the wire and a plane wave incidence source. The current that is computed from simulation using Breakall's approach is compared with the current predicted from a short circuit measurement in Figure 4.21.

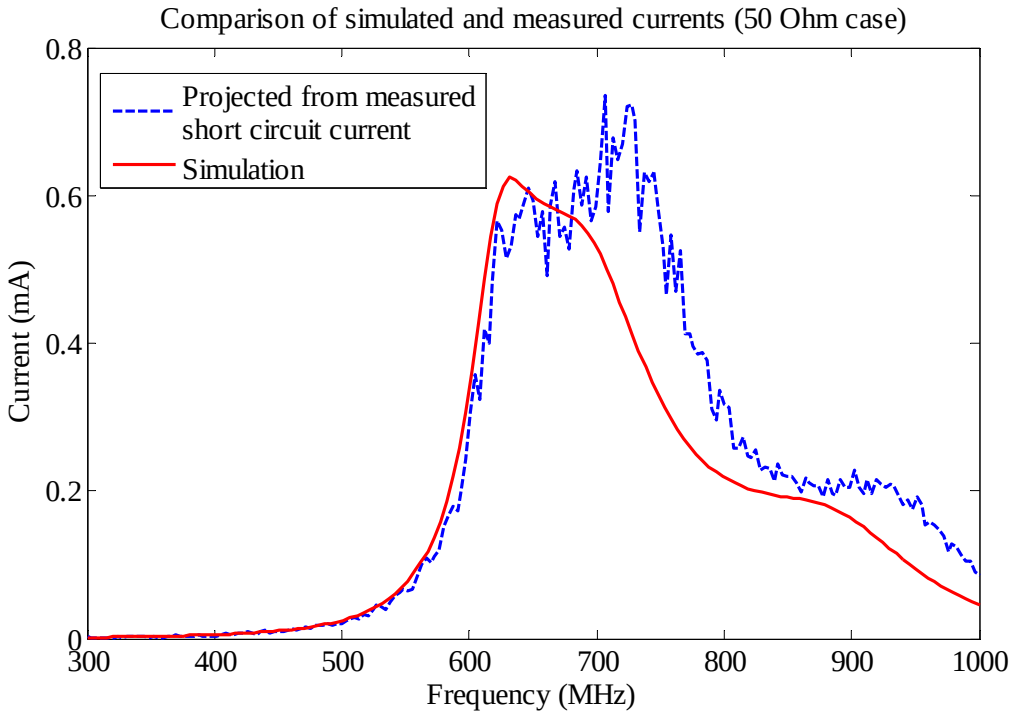

Figure 4. 21 Measured and simulated current on the wire terminated by a 50 Ohm impedance located inside the cavity

4. 4 Current induced on the wire located on a ground plane due to an excitation outside (without box)

The same analysis was performed without the box surrounding the wire. The 10.5 cm monopole was connected to a ground plane using a SMA connector and the same setup was used to measure all the S parameters. The reflection coefficient of the wire and the transfer functions are plotted in Figures 4.22 and 4.23 respectively. The resonances that were seen earlier in Figure 4.15 are not seen in Figure 4.22 because of the absence of the box. As expected the reflection coefficient graph has a sharp null around 700 MHz where the quarter wavelength of the wire occurs.

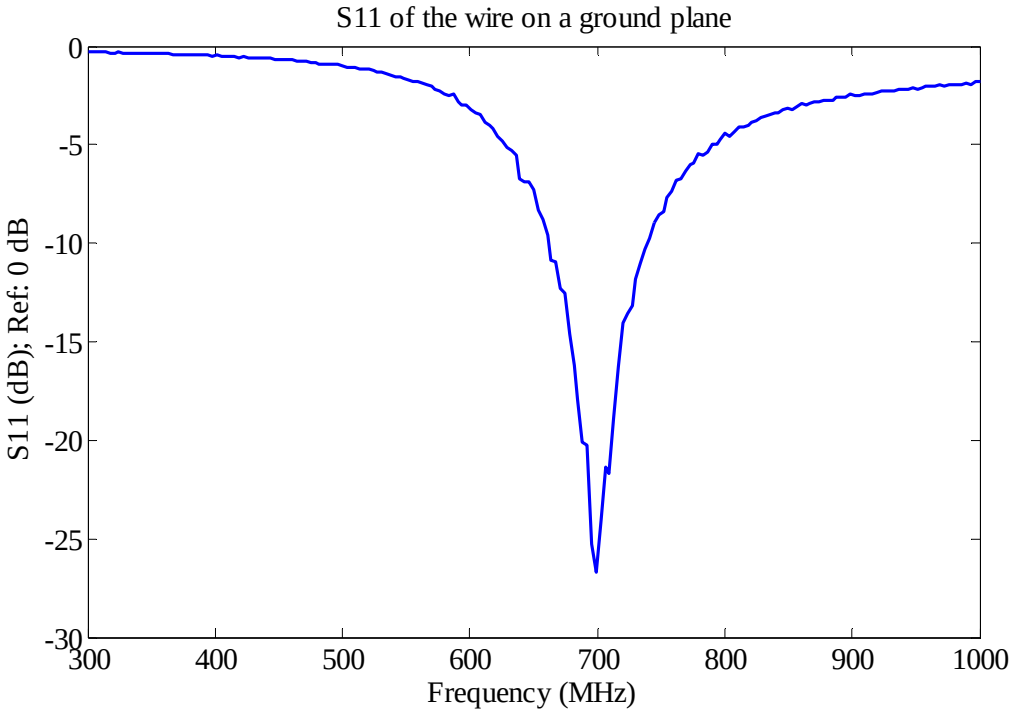

Figure 4. 22 Measured reflection co-efficient of the wire located on a ground plane (Open air measurement)

The transfer function shown in Figure 4.23 differs from Figure 4.16 in both amplitude and structure as the wire antenna is now not shielded by the box. Maximum coupling to

the wire antenna occurs where the reflection coefficient of the wire antenna is minimum (700 MHz).

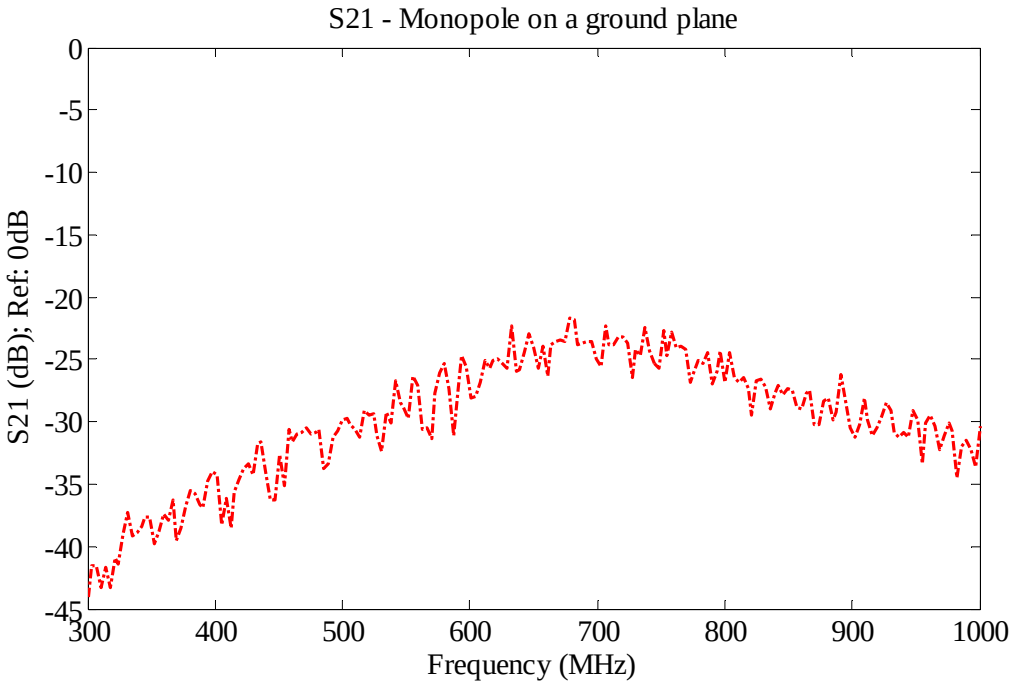

Figure 4. 23 Measured transfer function between the source antenna and the wire located on a ground plane

From the measured S21, the short circuit current is calculated using the formulation mentioned previously and compared with a simulation of a 10.5 cm monopole on a ground plane excited by a plane wave source at normal angle of incidence as shown in Figure 4.24.

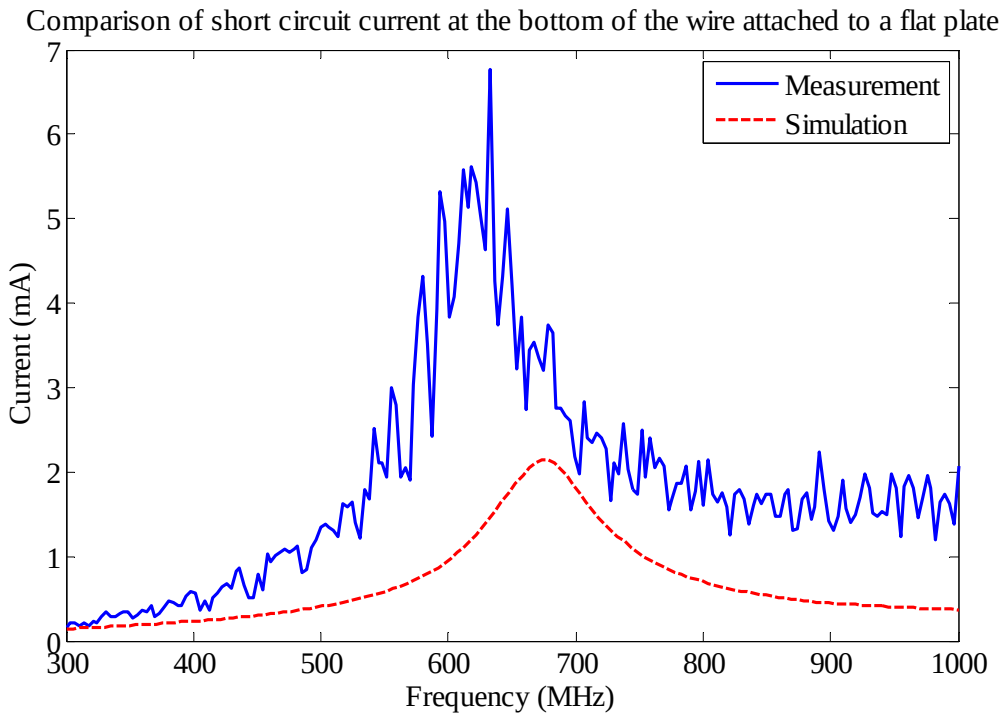

Figure 4. 24 Measured and simulated short circuit current on the wire located on a ground plane

The amplitudes of the measured and simulated short circuit current at the bottom of the wire were different but the trend of the graph seems to follow one another. The current at the bottom of the wire when it is terminated by any arbitrary impedance value was calculated using eqn. (4.7) and the current graphs for 5 different impedances are given in Figure 4.25. When the impedance that is attached to the bottom of the wire increases, the magnitude of current decreases. The strong resonance that is seen in the short circuit case is not seen when the impedance is increased.

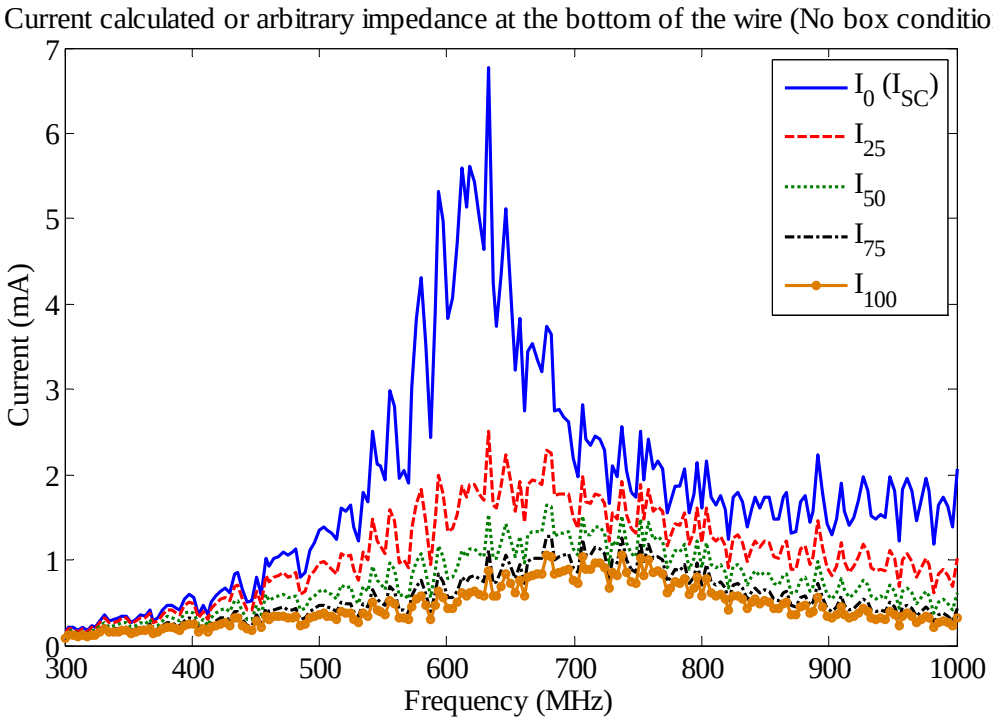

Figure 4. 25 Measured and simulated current on the wire terminated by arbitrary impedance located on a ground plane (not in the cavity)

The current that is computed from simulation is compared with the current predicted from a short circuit measurement for a 50 ohm termination in the Figure 4.26.

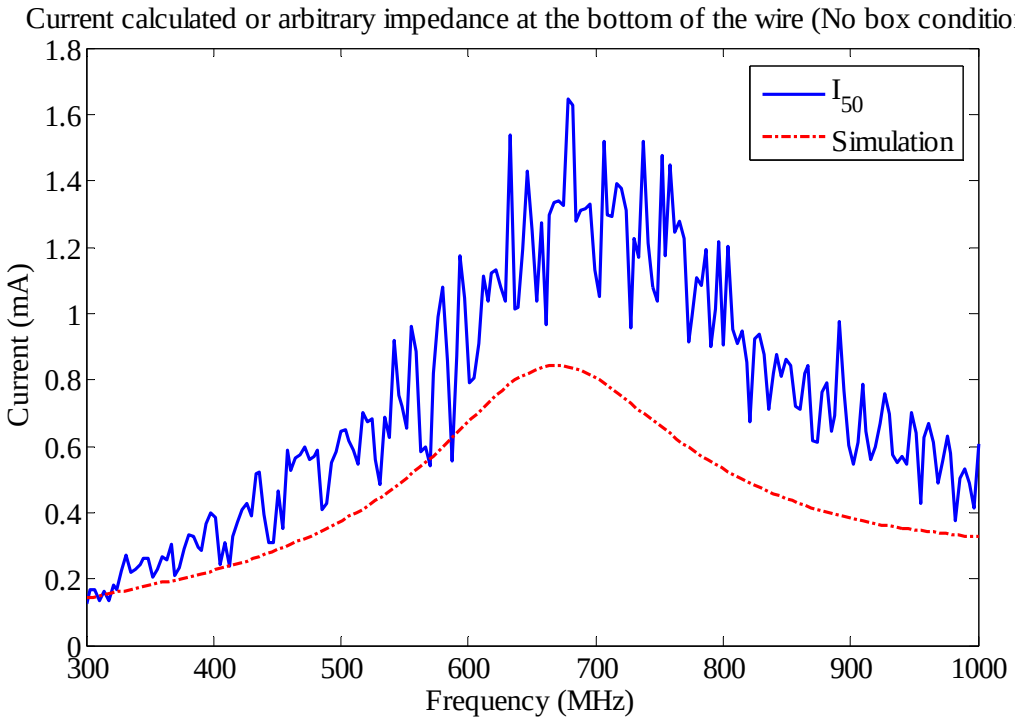

Figure 4. 26 Measured and simulated current on the wire terminated by a 50 Ohm impedance located on a ground plane

The trends of the short circuit current over the frequency bandwidth were captured in both simulations and measurements. The short circuit current at the end of the wire (end that is connected to the bottom wall) has been measured with reasonable accuracy.

In order to examine the distribution the current induced on the wire, the current has to be monitored for a variety of scenarios. Varying the random variables such as cavity size, volume, fill, size and/or position of the wire and/or the size of the aperture and/or coupling mechanism as mentioned before, results in a change of current induced on the wire. Initially the angle of incidence of the incoming plane wave is varied while the wire length, cavity size and aperture dimensions are unchanged.

4.5 Change in angle of incidence

The angle of incidence of the incoming plane wave was varied and the short circuit current for all the incidence angles was computed. The position and location of the wire, size of the aperture, size of the cavity, frequency of interest and polarization of the incoming plane wave were not changed. Both simulations and measurements were performed for a sweep along two principal axes of the box. The sweep angle was varied from 0 to 180 degrees and with a step size of 5 degrees. The two major sweep axes are denoted as sweep along Phi (along x) and sweep along Theta (along y). The measurements were firstly performed inside an anechoic chamber and the distance between the front face of the box and the tip of the log periodic antenna used as a source is maintained to be 1 m. The source antenna was moved in 5 degree steps and S parameter measurements were made with the network analyzer. From the S parameter data, the short circuit current was calculated using the procedure in Section 4. 3. 2. A screen shot of the simulation setup is provided in Figure 4.27.

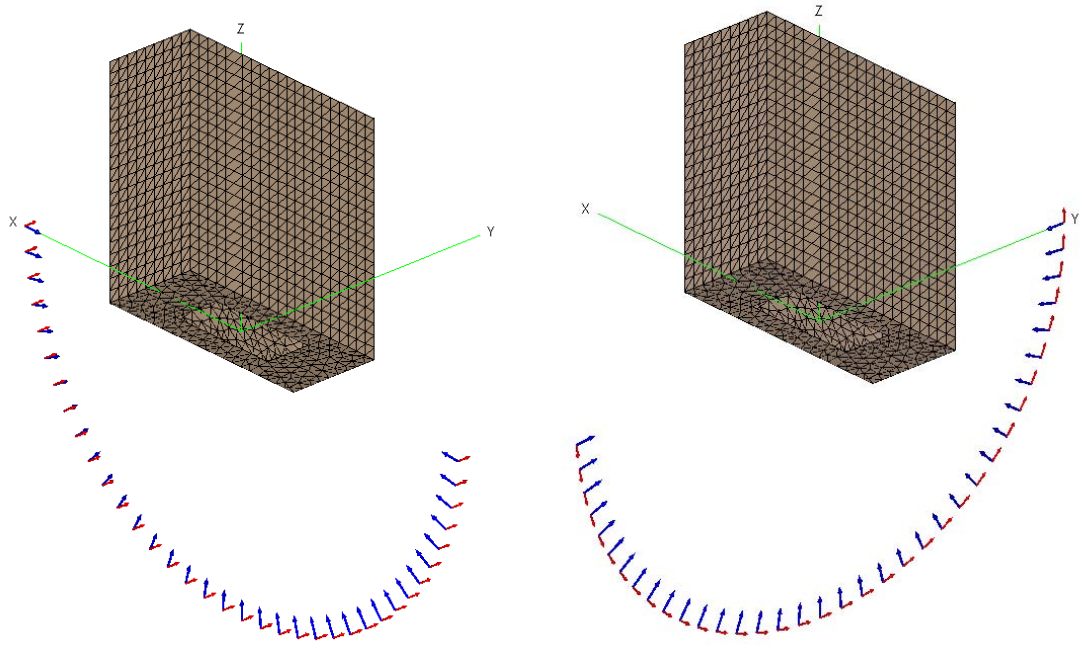

Figure 4. 27 Simulation setup for angle of incidence sweep along Phi and Theta axis

The plots of measured short circuit current for the multiple angles of incidence along Phi and Theta axis are shown in Figures 4.25 and 4.26 respectively. The plots of the simulated short circuit current for the multiple angles of incidence along Phi and Theta axis are shown in Figures 4.27 and 4.28 respectively. The self resonances of the box have been clearly captured in both the simulations and measurements. The normal angle of incidence has the maximum coupling into the box which can also be noticed in both the measured and simulated data i.e. the current induced on the wire is a maximum when the angle of incidence of the incoming plane wave is normal to the face of the box.

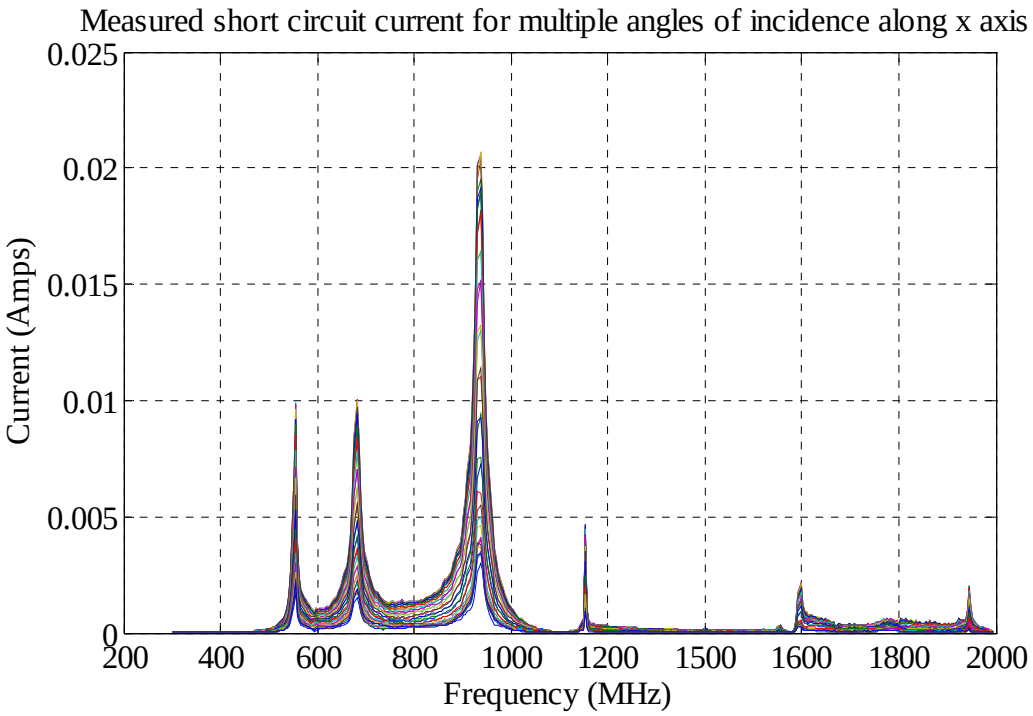

Figure 4. 28 Measured short circuit current for sweep along Phi

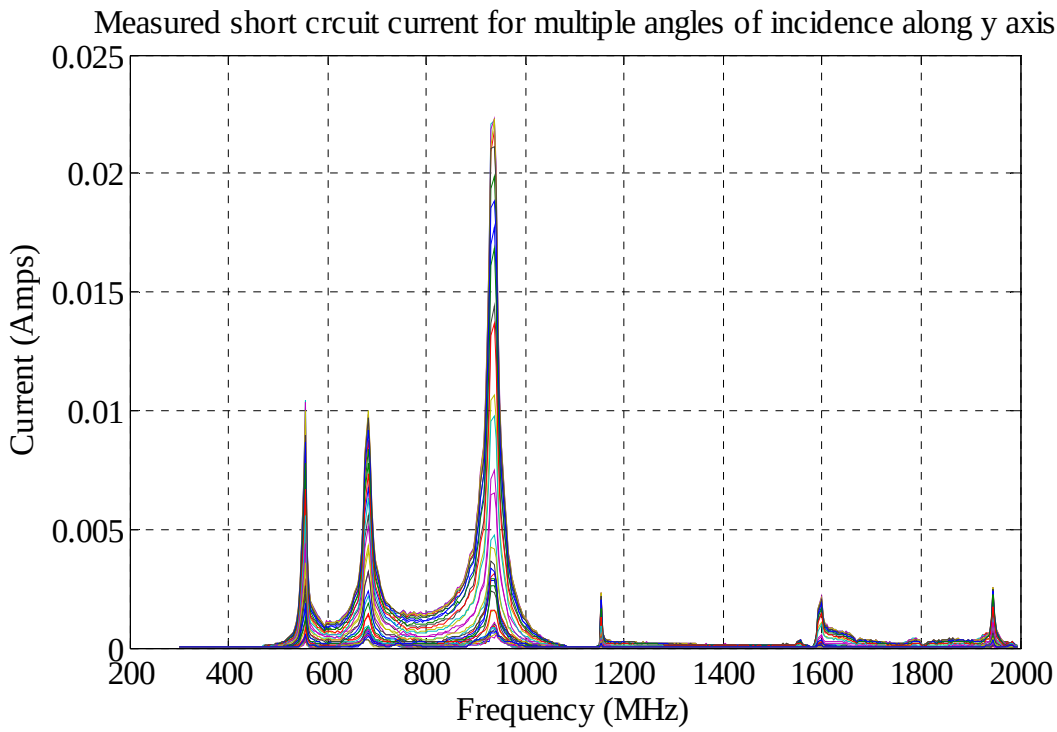

Figure 4. 29 Measured short circuit current for sweep along Theta

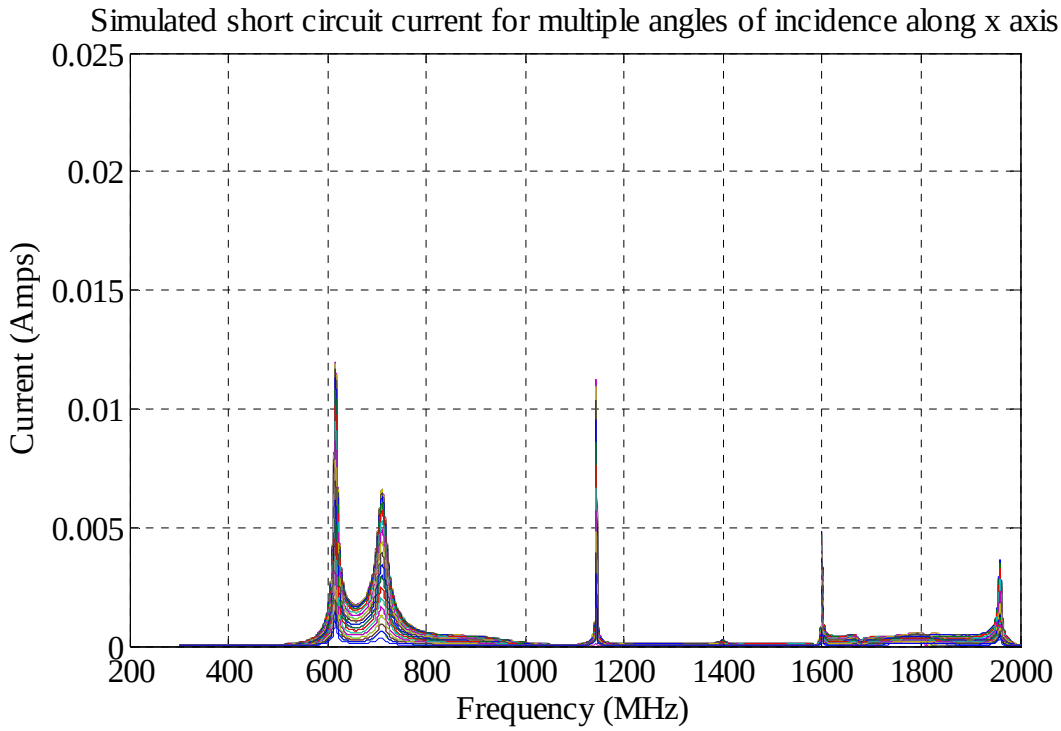

Figure 4. 30 Simulated short circuit current for sweep along Phi

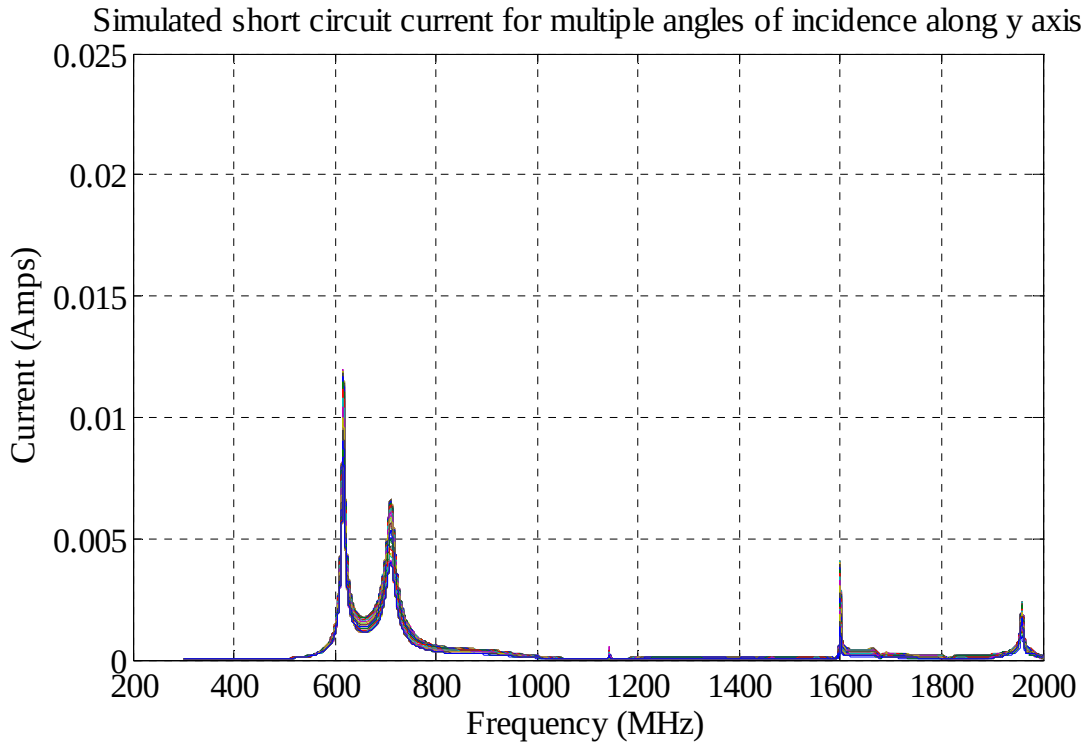

Figure 4. 31 Simulated short circuit current for sweep along Theta

A plot of the measured and simulated short circuit current for normal angle of incidence when the source is along the Phi and Theta axis is shown in Figure 4.32. Comparison between the measured and simulated current shows the peak around 923 MHz is seen only in the measurement. It is suspected that the cause of this peak is some external noise coupling onto the long length of cables running outside the chamber.

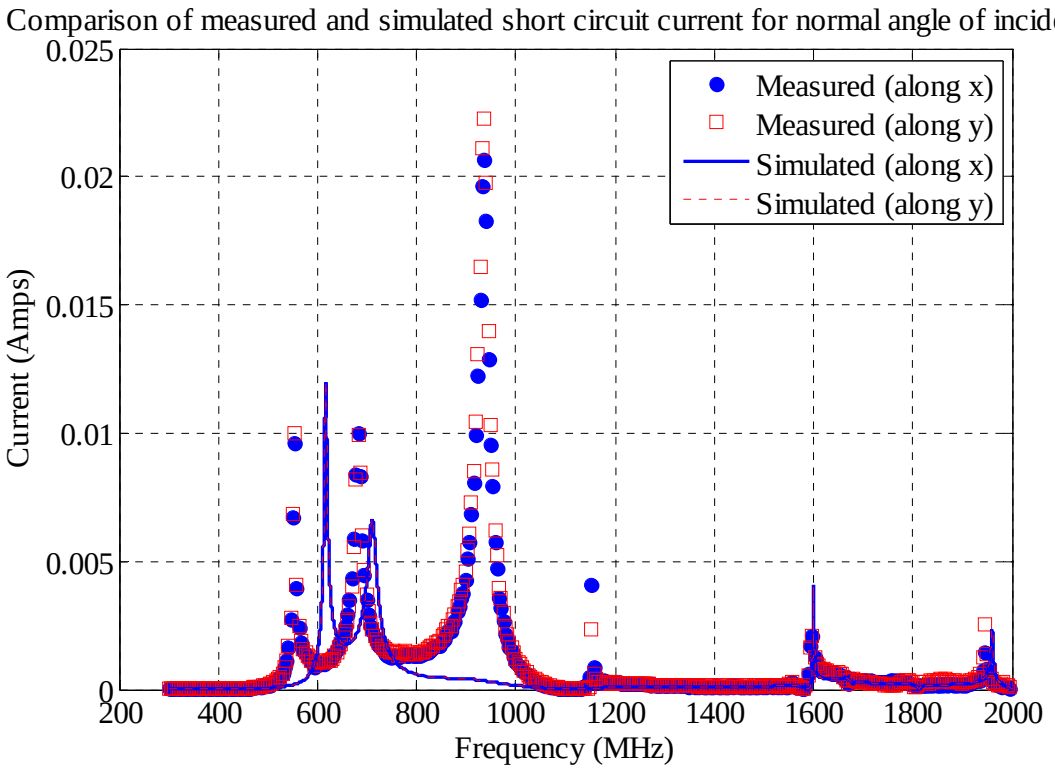

Figure 4. 32 Measured and simulated short circuit current at normal angle of incidence

In order to clarify the coupling around 923 MHz which was seen in anechoic chamber measurements, the same measurement was performed outside the chamber (referred as OATS measurement here) and also inside the reverberation chamber. Because of the versatility of reverberation chamber, the box was radiated from multiple angles of incidence and polarizations at the same time and any hidden resonances of the box will

be exposed. If the peak around 923 MHz was due to the box resonance, it will be visible in reverberation chamber measurements.

A comparison of measured current using multiple measurement techniques for normal angle of incidence of a co polarized source is presented in the Figure 4.33. In addition to the anechoic chamber measurements, open space measurements of the current induced on the wire located inside the cavity due to the plane wave source outside are presented. The major difference between the anechoic chamber measurement and the free space measurement will be some ground bounce. The measurement setup was maintained to be the same and the S parameters were measured to calculate the short circuit current. The next set of measurements was performed in a reverberation chamber where the direct illumination of the front face of the box is prevented. The transmit antenna was placed away from the cavity and focused to a corner of the chamber. The reverberation chamber used in this measurement is operable with good statistics from 80 MHz and above. Only the vertical tuner is used in this measurement as the frequency of interest was from 300 MHz. 100 discrete tuner positions (3.6 degree separation) were used and at every tuner step, all the S parameters were measured for a frequency sweep of 300 MHz to 2 GHz. From the mean of all the 100 tuner positions the final S parameter set is calculated and used to calculate the short circuit current.

The reverberation chamber measurements simulate a real world situation where a box will be operating in a cavity and where the details of the angle of incidence or polarization with respect to the box are not precisely known. By the very nature of

reverberation chamber testing, the field outside the small box are stirred hence the energy that impinges on the front face of the box is from random directions and random polarizations. Depending upon the aperture coupling at that particular frequency, the fields inside the box could be complex or simple. For this particular measurement, the complexity inside the box was not considered. To completely consider the complexity inside the small box, fields inside the box also needs to be stirred [25].

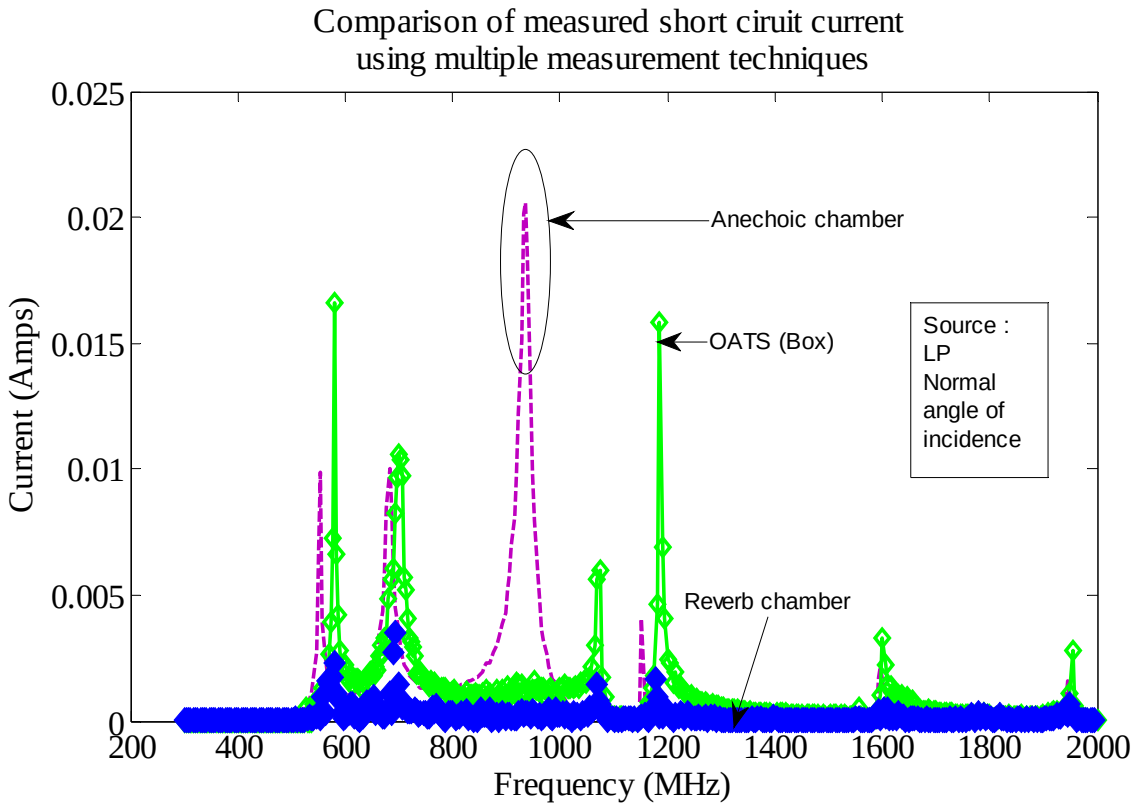

Figure 4. 33 Measured short circuit current using multiple measurement techniques

From the comparison shown in Figure 4.33, it can be seen that there is a good correlation between all the different measurement techniques. The amplitudes of the measured short circuit current are different especially because the gain of the source antenna is treated very differently in different test methods. Also the anomaly in the anechoic chamber

measurements around 923 MHz cannot be seen in any other test. This again asserts the fact that the external noise in the anechoic chamber measurements could be the reason for the peak.

4.6 Distributions for the short circuit current considering angles of incidence

The motivation behind this exercise was to develop a probability distribution model for the current on the wire due to change in random variables listed before. By fitting a distribution model, the question of "What is the probability that the current induced on the wire will exceed some value?" can be easily assessed without requiring much details of the wire or the box in which this wire is located. The procedure to calculate that probability is detailed in the next chapter.

In order to develop the probability distribution model for the current induced on the wire, the reverberation chamber measurements seem to be optimal. Due to the reflective walls of the chamber, the incident fields on the aperture are truly random. Hence more measurements were performed by moving the probe to positions 7 and 13 (Refer Figure 4.10) for the same aperture size. Then the aperture size was varied from 15x6 cm to 15x1 cm and the measurements were repeated for wire positions a, 7 and 13. Measured currents on the wire for the two cases are shown in Figures 4.34 and 4.35. From the current calculated from the S parameter measurement is each case, a methodology was developed to access the distribution of current on the wire.

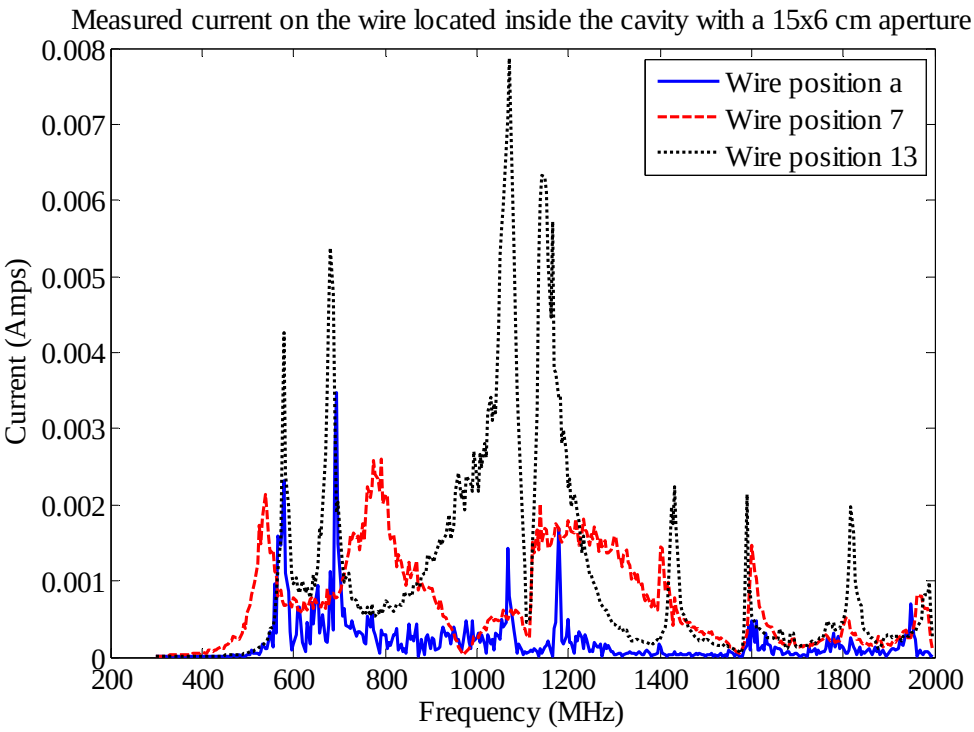

Figure 4. 34 Measured short circuit current for wire positions a, 7 and 13; aperture 15x6 cm

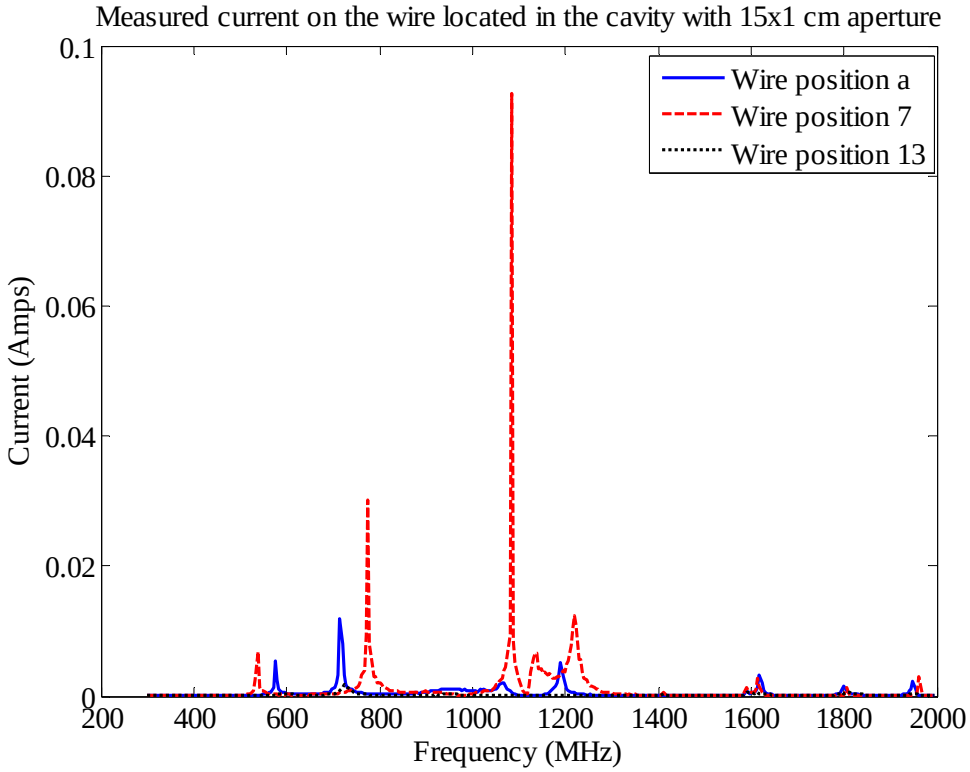

Figure 4. 35 Measured short circuit current for wire positions a, 7 and 13; aperture 15x1 cm

In the work thus far, a presentation of a variation of angle of incidence of the source while clearly defining all the other parameters like the size and fill of the box, coupling mechanism into the box, size of the aperture, length and location of the victim wire inside the box and frequency of interest. A procedure was developed to calculate the current on the wire from a simple S parameter measurement. The simulation and measurements were carried out with multiple techniques and now a probability model will be attempted for the calculated current. The distribution for the current and also a probability model of failure will be discussed in the next chapter.

Chapter 5

5.0 STATISTICS OF THE INDUCED CURRENT, EMI THREAT MODEL AND PROBABILTIY OF FAILURE

Any device operating amid other electronic devices or co-located in an environment where other electronic devices are also operating at the same time may be susceptible to an environmental disturbance such as electromagnetic interference inducing external faults without any visible damage to internal components. These errors can be ranked anywhere from a minor glitch to fatal error depending upon the seriousness of the issue. Most external faults are transient and can cause system upsets or errors. The system could revert back to its original state (functioning state with no error) based on the availability of redundant systems or process routines which would respond to the failure and issue a system reset. The typical error modes in digital data transmission can be bit state changes in the data stream, logic changes in controllers, registers, etc.

System stability will be affected if the disturbance (EMI) crosses a threshold or lasts for a long time (after crossing the threshold) or if the crossover above the threshold occurs too frequently. Threshold could be defined as the point that must be exceeded to produce a

particular (yet undefined) effect and based on the application it could be the amount of current coupled onto a wire, amount of noise in a channel or field strength at a distance.

In this work, the threshold values are rather arbitrary, and a certain value of current induced onto the wire due to EMI is considered as the threshold. Based on the system upsets, we can classify the failure modes to be: 1. Peak power failure: the threshold above which system stability deteriorates is crossed causing a failure; 2. Average power failure: the threshold above which system stability deteriorates is crossed and stays there for some period of time; 3. Change of state failure: the threshold above which system stability deteriorates is crossed many a times causing a failure (system reset is issued immediately when the values are below threshold). From [26] it is clear that all these types of failures can be initiated by EMI. From the data available, models could be developed for each type of failure and then appropriate test methodology can be chosen in the laboratories to asses the EMI effects and also improve the system stability.

By choosing an appropriate statistical model, the probability of failure of a system can be calculated. In this study a methodology to calculate the probability of threat is derived based on the presence of EMI and EMI presence in a certain fashion such as peak or average EMI above the threshold. A Markov chain (discrete state, discrete time) model is chosen to represent the occurrence of upset due to EMI. The advantage of using a Markov chain is that the present state contains, in a probabilistic sense, information about future states and thereby facilitating the calculation of possibility of being in a state. The change of system state from one to another is called transition and the probability

associated with it is called transition probability. The probability of the system being in a state is called the stationary probability of that state.

Probability of the observable is the probability that the observable is above or below a certain threshold. In this case, the observable is the current coupled onto the wire due to external EMI hence the probability of the observable is the conditional probability that the current induced on the wire either exceeding or not exceeding a certain value for a given input power which might lead to a system failure. The probability is conditional because failure is restricted to happen only in the presence of EMI. The probability of failure of the system is calculated by multiplying the conditional probability of the observable leading to system failure with the probability of the EMI threat or presence. In other words the system failure would happen if the EMI threat is present and present in a certain fashion and that EMI causes the observable to exceed the threshold as well.

5.1 Statistics of induced current (Conditional probability of the observable)

The conditional probability of the observable is calculated from the current measured on the wire. As the current measured varies widely with the position of the wire and the cavity and aperture size and shape and also the physical length of the wire, the statistics of the measured current can provide more information than the specific values of the current measured. A model to calculate the probability of the induced current is proposed below.

Weibull model

$$f(x) = \frac{k}{\lambda}\left(\frac{x}{\lambda}\right)^{k-1} e^{-\left(\frac{x}{\lambda}\right)^{k}} \qquad \textbf{(5.1)}$$

The Weibull distribution is a two-parameter distribution (scale-λ and shape-k). The probability density function of the random variable x is given in eqn. (5.1). By adjusting these two parameters, a variety of shapes can be obtained to fit the experimental data. Hence the Weibull distribution is highly adaptable. The major distributions of interest are the exponential and Rayleigh distributions which can be represented by a Weibull model with a shape parameter (k) of 1 and 2 respectively. The exponential and Rayleigh distributions are of interest because the power in RC follows an exponential distribution while the field follows a Rayleigh distribution. To fit a statistical distribution for the current, independent data samples are needed as discussed in Chapter 3.

Due to the change in angles of incidence and polarization of the fields hitting the front face of the box (due to different tuner positions for the test inside a reverberation chamber), the aperture fields are different. Because of different aperture fields, the current induced on the wire at all frequencies of interest will be different. These currents are subjected to statistical analysis to see what model best describes the distribution of the current. The independent data could be best obtained from the measurements performed inside the reverberation chamber. Though angles of incidence are varied in the anechoic chamber setup, it is not truly random while in the reverberation chamber, the box is excited from all directions in a purely random fashion. For the statistical analysis of the current, data from the reverberation chamber measurements will be used henceforth.

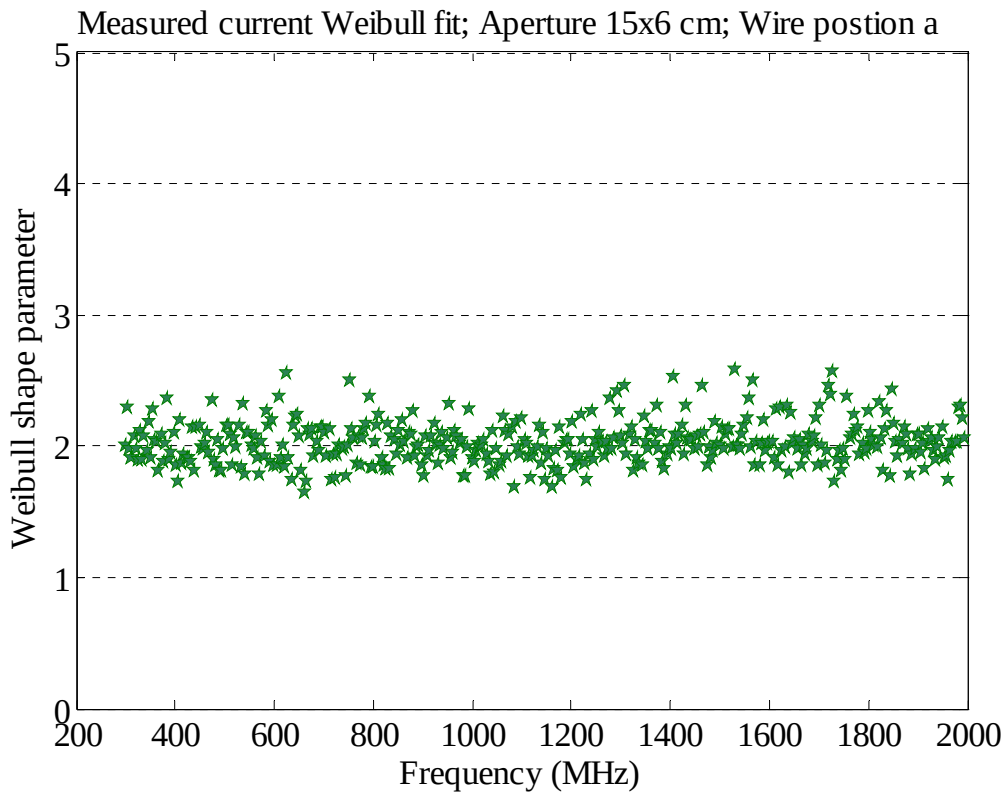

Figure 5. 1 Weibull shape parameter fit for the measured short circuit current at multiple frequencies (15x6 and a)

Performing a Weibull fit on the currents calculated at each frequency at 100 different tuner positions (every data point in Figure 5.1 represents the shape parameter calculated for a Weibull fit from 100 different data points generated by 100 different tuner positions at each frequency), it can be seen from Figure 5.1 that the Weibull shape parameter is close to 2 at almost all frequencies. A shape factor of 2 for a Weibull distribution corresponds to a Rayleigh distribution. This distribution suggests that the current that is induced on the wire at different frequencies with an aperture excitation as it operates in an overmoded cavity follows a Rayleigh or a Chi with 2 D.O.F (degrees of freedom) distribution.

From the distribution of the field measured at any point inside an overmoded cavity, from RC theory [4], one would expect the current also to have the same distribution as the fields because of the distribution of power inside a well-stirred reverberation chamber. The power follows an exponential or Chi Square with 2 D.O.F distribution. If power is the product of current and field at a point (P=VI), then if voltage follows a Chi with 2 D.O.F then the current should also follow a Chi with 2 D.O.F distribution (Rayleigh) to give power which follows a Chi square with 2 D.O.F distribution.

What is of interest here is that irrespective of the mode regime (under, over etc...), the current follows a Rayleigh distribution like an overmoded cavity. This is equivalent to placing the wire on the wall of the RC and calculating the distribution of current for different frequencies/different tuner positions. The same analysis was repeated by moving the wire inside the box to two other positions (7 and 13: Refer Figure 4.10) and the same shape factors were obtained for all cases. The size of the aperture (15x6 cm aperture on a 30x12 cm wall; 50% of the surface area of the wall is the aperture) could be the reason for the transition of the overmoded behavior from the overmoded RC to the cavity. To investigate the influence of the size of the aperture on the distribution of the current on the wire, the current induced for an aperture size of 15x1 cm was measured for three different wire positions and interestingly all the cases at all frequencies followed a Weibull shape factor of 2 representing a Rayleigh distribution (Refer Figures 5.2 and 5.3). Given that the current follows a Rayleigh distribution at all frequencies of interest, the cumulative distribution plot for the mean normalized current measured at f=300 MHz for wire position ‘a’ and aperture size of 15x6 cm is given in Figure 5.4.

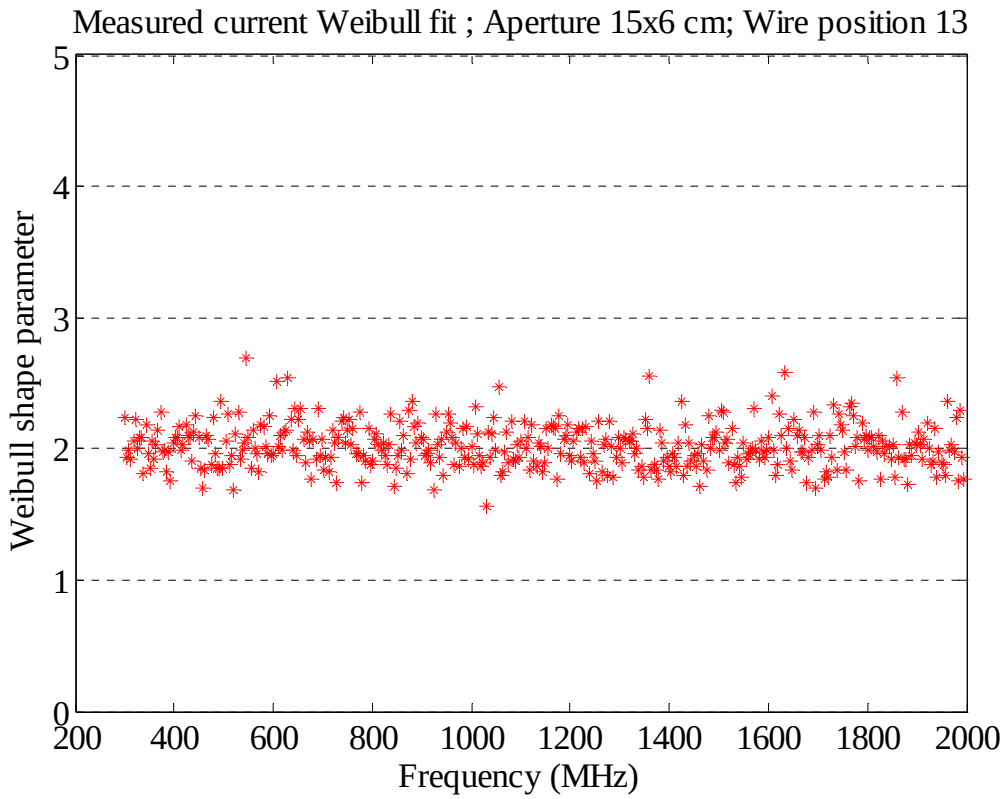

Figure 5. 2 Weibull shape parameter fit for the measured short circuit current at multiple frequencies (15x6 and 13)

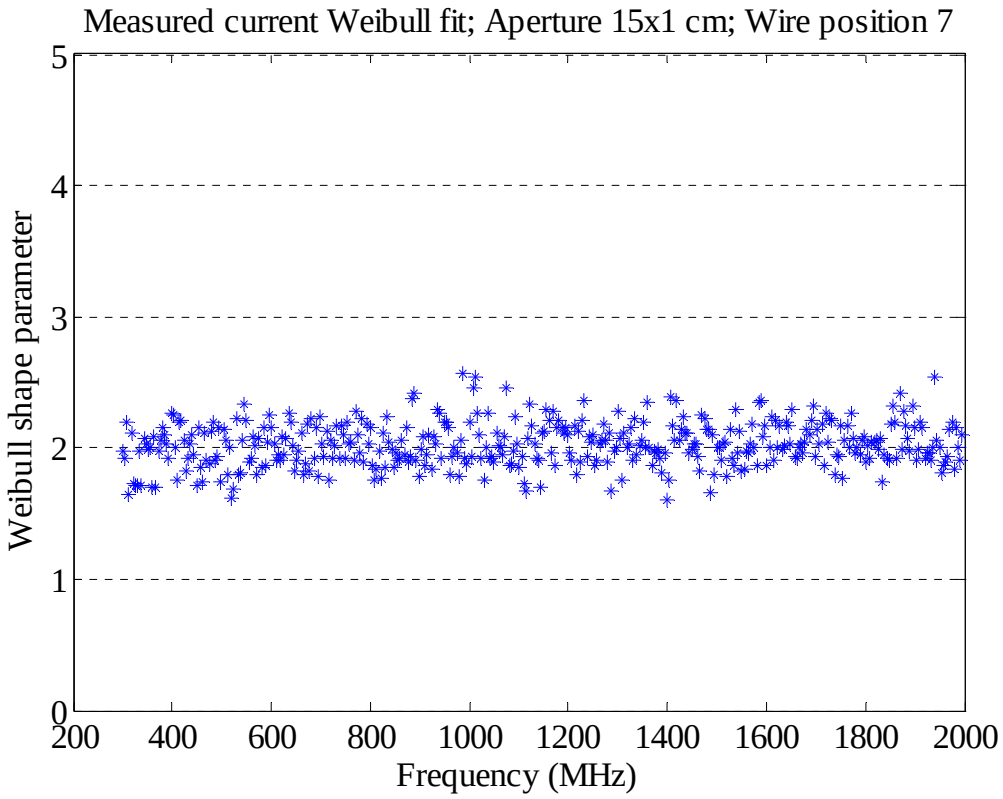

Figure 5. 3 Weibull shape parameter fit for the measured short circuit current at multiple frequencies (15x1 and 7)

As at all intended frequencies/aperture sizes and wire positions, the induced current distribution was Rayleigh, the same cumulative plot will hold true. The cumulative distribution plot can be used to calculate the conditional probability that the current induced on the wire either exceeding or not exceeding a certain value for a given input power which in turn causes a EMI presence. For example the probability that the normalized induced current will exceed 0.42 is about 88% at all frequencies. In a similar way the probability that the normalized induced current will not exceed 1.27 or 2.12 can be calculated to be ~71% and ~97% respectively.

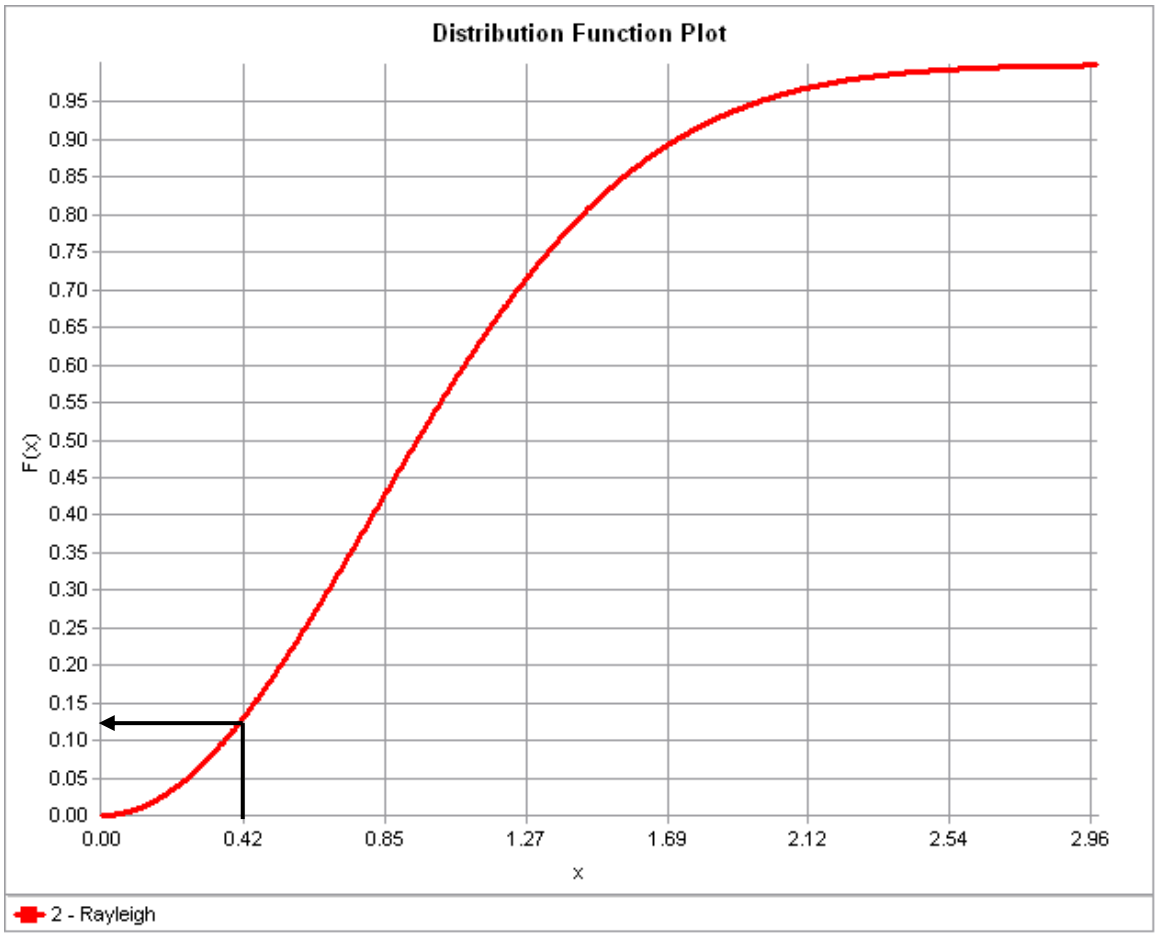

Figure 5. 4 Distribution plot of Rayleigh distribution obtained from the mean normalized measured short circuit current

5. 2 Poisson process to model electromagnetic interference

The major problem in representing the EM disturbance is finding a model that accurately describes the way EM disturbances interfere with the normal operation of the system and cause a failure. The general nature of the EM induced failures are machine independent [27]. An effective way of expressing the EM disturbance and the failure caused due to it is through a Markov-chain (discrete state and discrete time) derived by assuming that the

arrival process of the interference follows a Poisson process and the duration of each disturbance has an exponential distribution [28].

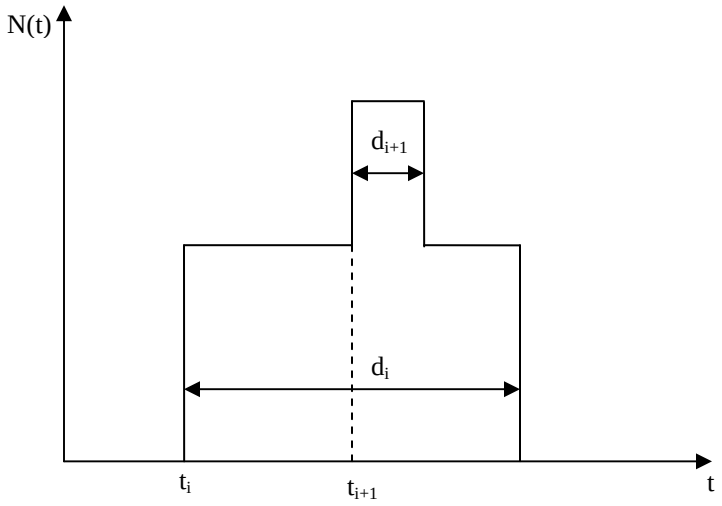

Figure 5. 5 Example for EMI arrival and duration

An EM disturbance can be viewed as in Figure 5.5 where, N(t) denotes the number of active EM disturbances that occur during the time *t*, t_i denotes the arrival time i^{th} disturbance and the duration of that disturbance is given by d_i. The Markovian assumption describes the statistics of t_i and d_i and also assumes that the radiation sources are not correlated or coordinated in any long term fashion [27].

The Markovian assumption is also supported [29], where the impulse amplitude is assumed to follow a Rayleigh distribution while the occurrence of pulses follows a Poisson process. Similar assumptions have been used in all of Gray and Gonzalez [27] work where stability analysis was performed on flight controllers due to the influence of EM disturbances. The occurrence rates of EMI have been investigated in [30] and been characterized with relatively short period of presence followed by a long latency period.

The assumption of EMI following a Poisson process appears to be valid for burst upsets that occur due to short presence of EMI. A more detailed approach of calculating the probability of failure due to the three types of failures explained in Section 5.0 is proposed in the following sections. The Poisson model will be used to calculate the long term probabilities.

5. 3 Poisson process

A random process refers to a physical process that is fully or in part controlled by some sort of chance mechanism. Some examples of processes like these would be noise in a communication channel, the measurement of quality of manufactured products coming out of an assembly line, etc. These processes are characterized by their time dependence, the fact that certain events take place or do not take place at regular intervals of time or throughout a continuous interval of time.

For processes taking place over a continuous interval of time, the mathematical model that can be used to describe situations like this is that of a Poisson process. To find the probability of x successes i.e. values exceeding threshold during a time interval of length T, the interval is divided into n equal parts of length Δt such that $T = n \bullet \Delta t$. Some of the assumptions for the model to be valid are given below

1. The probability of success during a very small interval of time Δt is given by $\alpha \bullet \Delta t$

2. The probability of more than one success in such a small time interval Δt is negligible
3. The probability of success in such a small time interval Δt is completely independent i.e. the success rate does not depend on what happened prior to that time

With these assumptions being satisfied, the probability of x successes during a time T with $n = T/\Delta t$, $p = \alpha \bullet \Delta t$ and $n \to \infty$ is given by a Poisson probability with mean $\lambda = n \bullet p = \alpha T$, α being the average (mean) number of successes per unit time.

$$p(x, \lambda) = \frac{e^{-\lambda} \lambda^{x}}{x!} \qquad \textbf{(5.2)}$$

5. 4 EMI

EMI is usually characterized by long latent periods followed by short periods of presence [26]. In order to understand the fault behavior of the system, it is necessary to understand the nature of the faults. Although it is impossible to model all the faults in a particular domain, the fault model should aim at describing the general effect of faults. The user of the model needs to understand the limitations behind how accurate and realistic the fault model is.

It has been reported in the literature that EMI faults may be regarded as sporadic single-bit faults [27, 31] essentially indicating that there is a minimum separation between

faults. A fault can occur due to EMI events occurring with minimum inter-arrival time or single burst (burst with maximum length). EMI faults can be treated as sporadic faults that would occur in digital communication systems, resulting in a single misinterpreted bit (called a “bit flip”) when there is a disturbance. An example of a digital signal under the influence of EMI resulting in bit flips is provided in Figure 5.6.

The frequently used model to describe faults due to EMI, is to model faults as a random pulse train with the inter-arrival times following an exponential distribution, leading to a Poisson process [27, 28, 29, 31]. The foundation behind this argument is that, there is no bound on the number of failures or individual faults due to EMI that can occur within any time interval. Faults that occur due to EMI are hard to predict. The times and nature of faults in the system are not known in advance.

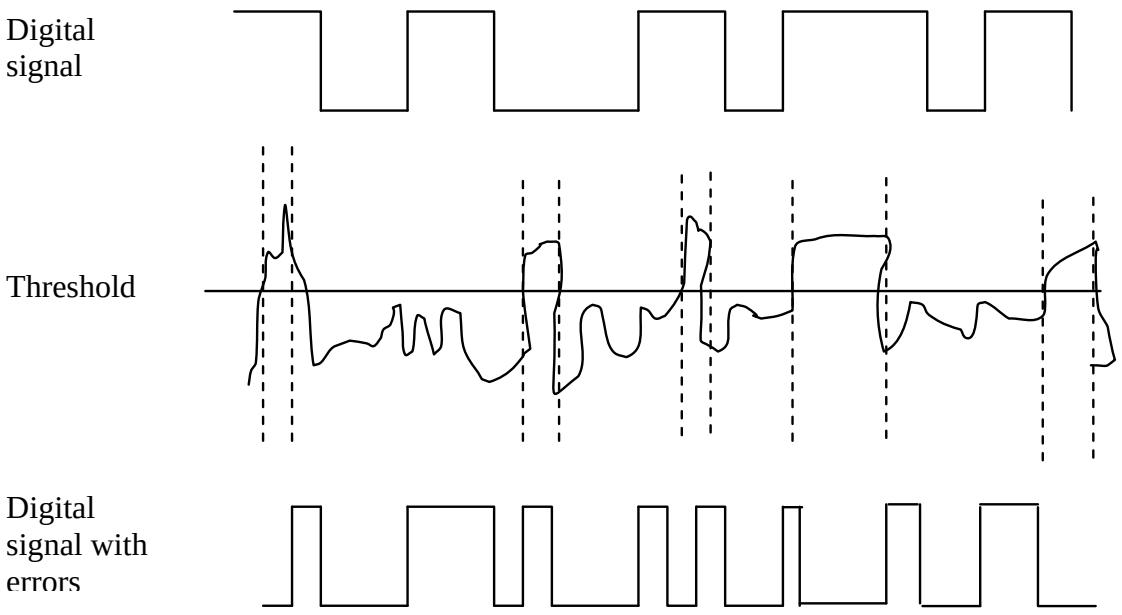

Figure 5. 6 Example for influence of EMI on a digital signal

The occurrence of fault in a communication channel follows a random distribution. The number of errors suffered by the system due to EMI in a given interval of time is not bounded, so the probability that the message in the communication channel is completely lost is always nonzero [31].

The random arrivals of EMI are well modeled using a Poisson process provided that the arrivals are considered over a long period of time. However, for short periods of time the faults are still considered to be randomly arriving but during the interval, the mean arrival rate may be higher than the mean obtained from longer observations.

It can be insisted that modeling the faults accurately is not possible and so understanding the failure rate (frequency of failure) is important than the exact probability of failure. With such an argument, the Poisson model has a tremendous range and can be used to model the faults occurring due to EMI.

5.5 Probability of threat due to peak, average and change of state EMI

Probability of threat refers to the probability that a threshold is crossed due to EMI of particular fashion. The probability of threat multiplied with the conditional probability of the observable going over the threshold will result in the overall conditional probability of the system. When the probability of EMI presence is multiplied with the overall conditional probability, the probability of failure can be calculated. The probability of threat due to peak, average or change of state EMI was calculated based on the

measurements performed in the previous chapter. The measurement setup is explained as follows. A 10.5 cm wire is placed inside a rectangular cavity made of aluminum with a rectangular aperture at the front face. The cavity is enclosed on all sides so the only mechanism for the energy to get into the cavity is through the aperture. The dimensions of the cavity and aperture are given in section 4.3. The setup is placed inside a reverberation chamber and S_{21} data is collected as a function of frequency for 100 different tuner positions. The wire placed inside the cavity is the receiver antenna while the log periodic antenna placed inside the reverberation chamber focused on a corner serves as the transmit antenna. From the raw S_{21} data, the short circuit current is calculated as mentioned in chapter 4 following Breakall [24]. The probability of threat that the current induced on that wire exceeds a certain threshold due to the EMI threat will be discussed in the following paragraphs.

To calculate the probability of different types of EMI threat, the maximum induced current values (mean normalized) recorded at all frequencies at the 100 tuner positions were considered as shown in Figure 5.7. Arbitrary thresholds were chosen and the different probabilities of threats were calculated. The same thresholds were used to calculate the conditional probability from the Rayleigh distribution. Every point in that frequency interval is considered to be independent as the system response is different at all frequencies. In some systems, the relationship between the EMI threshold and the observable threshold needs to be determined and appropriate conversions have to be applied to calculate the conditional probability. In our study both the thresholds are considered to be the same.

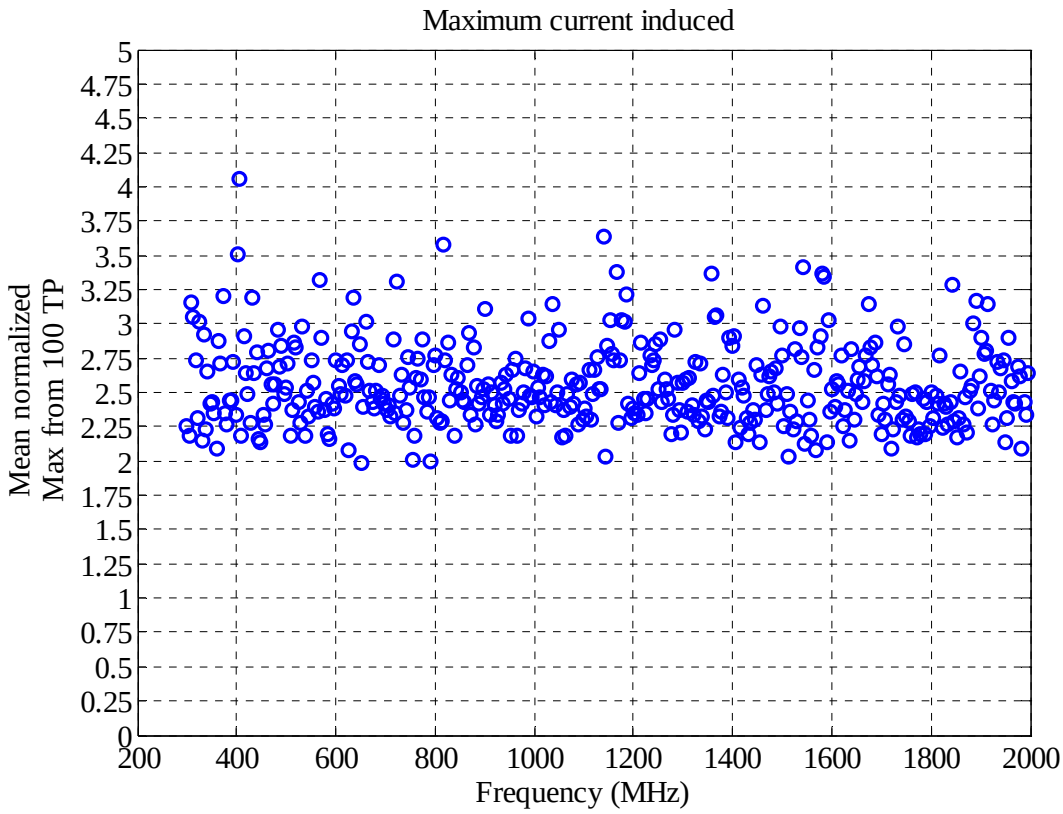

Figure 5. 7 Mean normalized Maximum induced current measured on the wire over the 100 different tuner positions. Aperture: 15 x 6 cm. Wire position 'a'.

A simple staircase figure can be used to represent the frequencies or time frames above the threshold (represented by a value 1) and below the threshold (represented by a value 0). Figures for different thresholds are shown below as examples.

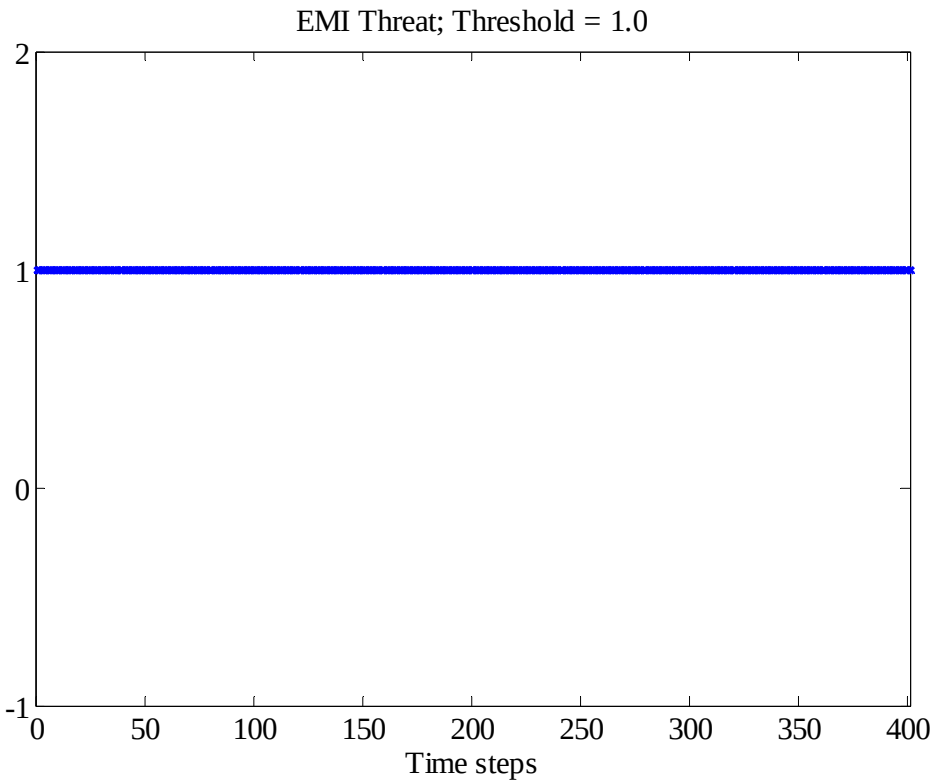

Figure 5. 8 Staircase function representing EMI threat for threshold 1.0 vs. time frame

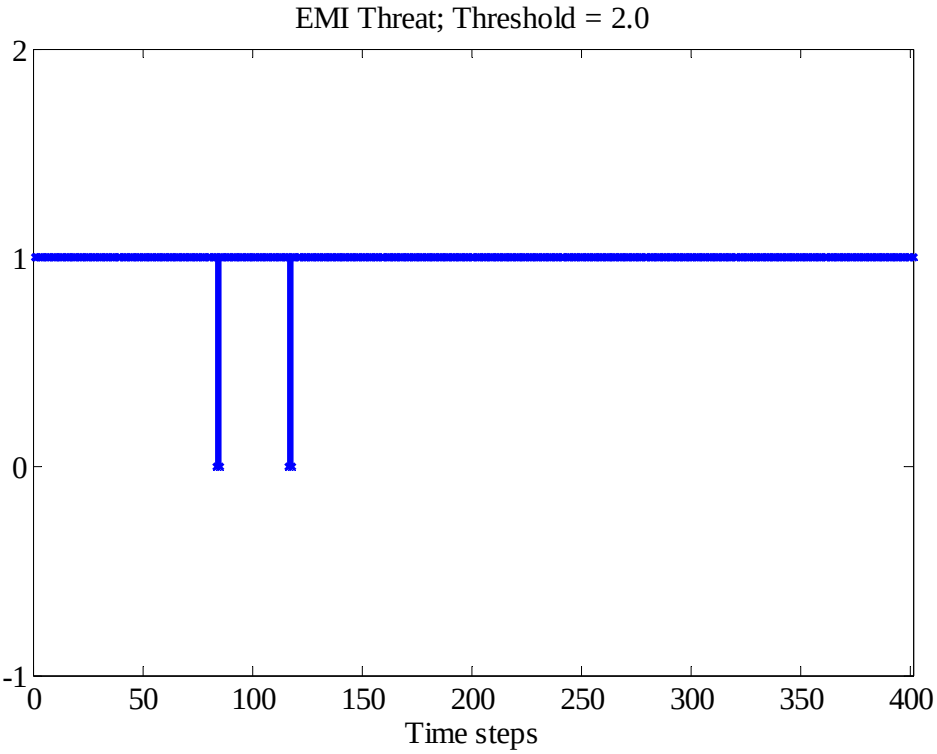

Figure 5. 9 Staircase function representing EMI threat for threshold 2.0 vs. time frame

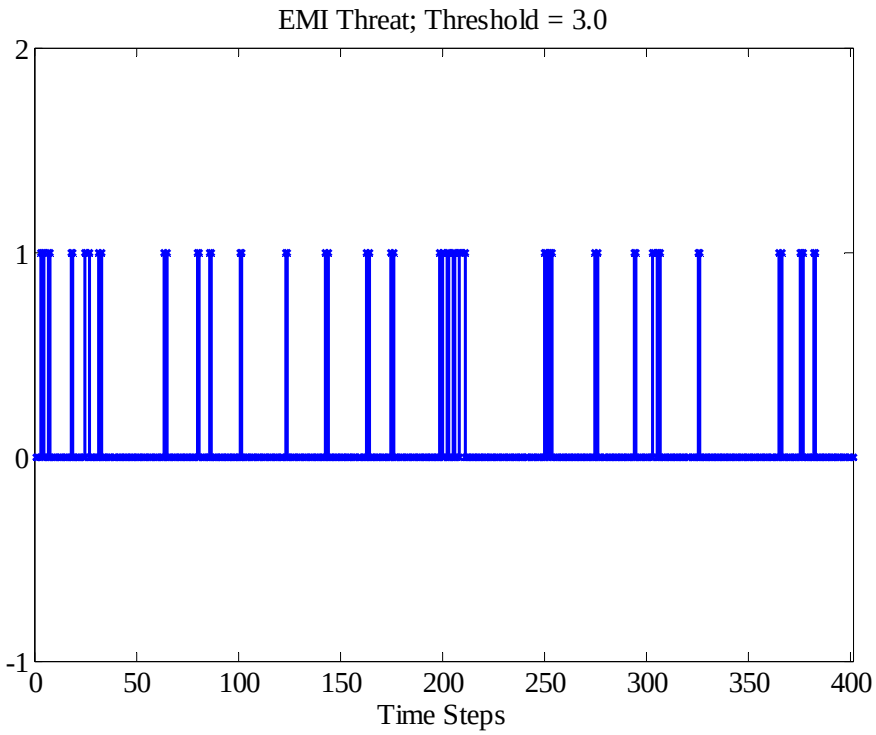

Figure 5. 10 Staircase function representing EMI threat for threshold 3.0 vs. time frame

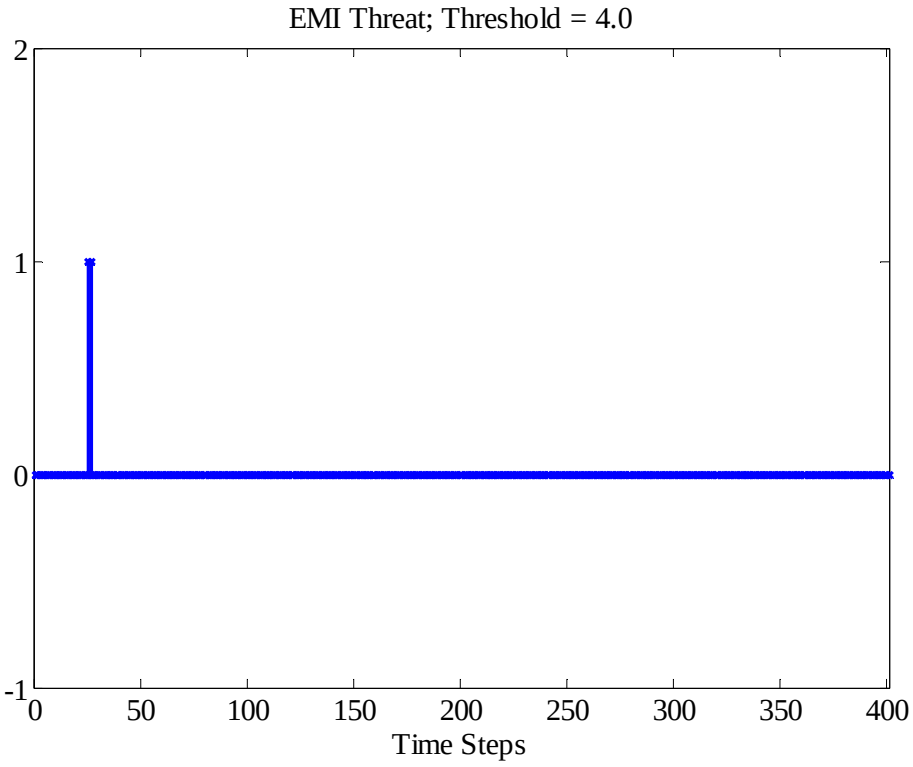

Figure 5. 11 Staircase function representing EMI threat for threshold 4.0 vs. time frame

a. Probability of Peak EMI threat

The ratio of the number of instances that are above the threshold to the total number of instances is an estimate of the probability of peak EMI threat. For example, when the threshold is chosen to be 1.0, at all frequencies the threat values calculated are above the threshold hence the probability of threat is 401/401 = 1. When the threshold is increased to 3.0, the number of instances where the measured threat is above the threshold is 34, hence the probability of threat is 34/401 = 0.0848. In other words when the threshold is 1, at all frequencies the probability of threat is 100% while when the threshold is increased to 3.0, only 8.48% of the time the threat exists.

b. Probability of Average EMI threat

The ratio of a certain number of consecutive points (i.e. window) for which the measured value is above the threshold to the total number of possible consecutive points for which the measured value is above the threshold is an estimate of probability of average EMI threat. For example, if we assume that the threshold is 1.0 and the threat need to be above the threshold for 50 consecutive time frames to cause a threat, the probability of threat due to average EMI is calculated to be 352/352 = 1. When the threshold is reduced to 3.0, the threshold is crossed multiple times in the window but the threshold does not remain crossed for 50 consecutive time frames hence the probability of threat drops to 0/352 = 0.

c. Probability of change of state EMI threat

The ratio of number of times the stipulated transitions occur from below the threshold to above the threshold to the total possible number of times the transition can occur from below the threshold to above the threshold is an estimate of probability of change of state EMI threat. For example if we assume that the threshold is 1.0 and there need to be 5 transitions from below threshold to above threshold state to cause a threat, the probability of threat is calculated to be 0/200 = 0. Because of the lower threshold, there is no transition and at all time frames, the calculated value is above the threshold. When the threshold is moved to 3.0 and 5 transitions from below threshold to above threshold state is required to cause a threat, the probability of threat now changes to 23/200 = 0.115. In other words, because of the transitions that are occurring from below the threshold to above the threshold for a higher threshold limit, there is a finite probability of threat.

A more realistic model for threat is a burst of controller upsets in the presence of EMI because an upset is more likely to occur in an upset state during the previous time frame than in no upset state.

The probability of threat due to EMI peak, average and change of state or transition is tabulated in Table 5.1. The probability of observable exceeding the threshold can be found from the Rayleigh distribution curve explained before and is also tabulated in Table 5.1.

Table 5. 1 Conditional probability of failure calculated from probability of observable and probability of EMI threat

Threshold	Conditional probability of the observable exceeding the threshold	Probability of EMI Threat			Overall conditional probability of failure occurrences in presence of EMI		
		Peak	*Average*	*Transition*	*Peak*	*Average*	*Transition*
1.00	0.45	1.00	1.00	0.00	0.45	0.45	0.00
1.25	0.29	1.00	1.00	0.00	0.29	0.29	0.00
1.50	0.17	1.00	1.00	0.00	0.17	0.17	0.00
1.75	0.09	1.00	1.00	0.00	0.09	0.09	0.00
2.00	0.04	1.00	0.90	0.00	0.04	0.04	0.00
2.25	0.02	0.88	0.00	0.20	0.02	0.00	0.00
2.50	0.01	0.47	0.00	0.46	0.00	0.00	0.00
2.75	0.00	0.22	0.00	0.30	0.00	0.00	0.00
3.00	0.00	0.08	0.00	0.12	0.00	0.00	0.00
3.25	0.00	0.03	0.00	0.03	0.00	0.00	0.00
3.50	0.00	0.01	0.00	0.00	0.00	0.00	0.00
3.75	0.00	0.00	0.00	0.00	0.00	0.00	0.00
4.00	0.00	0.00	0.00	0.00	0.00	0.00	0.00

5.6 Probability of failure

The total probability of failure of the system due to different EMI threats is calculated by multiplying the overall conditional probability of failure with the probability of EMI presence. A model to calculate the EMI presence probability is proposed in the following section. It can be seen from Table 5.1 that the overall conditional probability of failure decreases as the threshold is increased. An analysis like this will help in choosing the right threshold so that the system could be hardened against different types of EMI threats by running one such test.

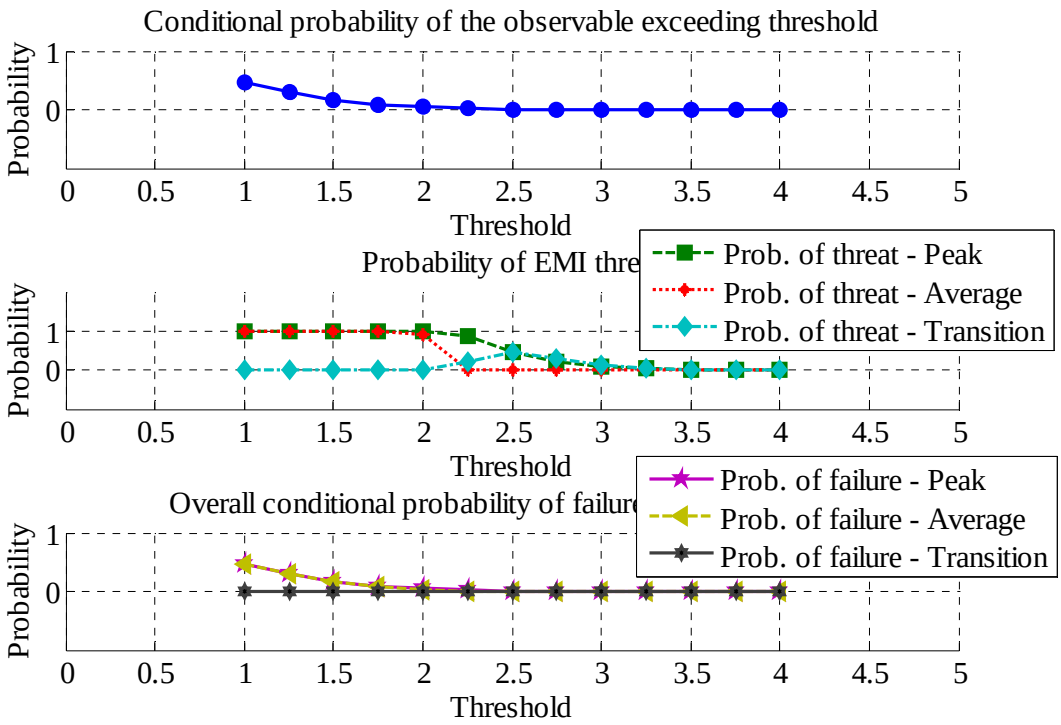

Figure 5. 12 Probability chart

For example by choosing the threshold to be 2.5, the probability of the EMI threat is maximized irrespective of the threat being peak or average or transition. Also if the probability of the observable crossing threshold is small, the probability of failure will also be small. Thus the system has been hardened against different types of EMI threats.

5.7 Markov model For EMI

A simple model for EMI assumes that the failure occurs only when EMI is present (irrespective of the EMI fashion i.e. peak, average or transition) with a probability '*p*'. The time period over which probability assumption is valid is one time frame '*Ts*'. A constant hazard function is assumed for the failure rate which states that the failure

depends only on that particular instant of time and does not depend on the pervious state being faulty or not.

A Markov chain with two states (Refer Figure 5.12) can represent this process of transition from absence to presence of EMI and vice versa. When there is no EMI, no threat exists to the system and when EMI is present, an upset occurs with a probability '*p*'.

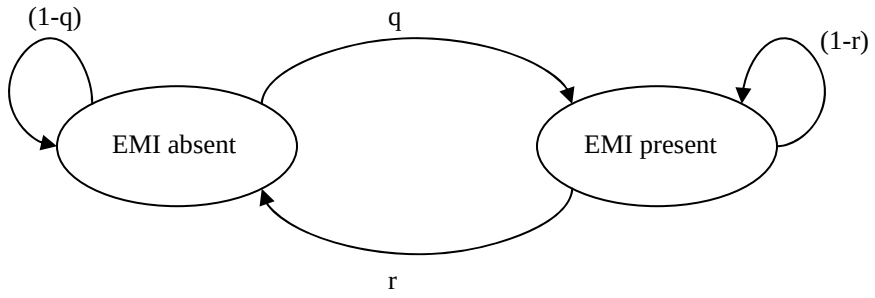

Figure 5. 13 Two stage Markov chain model for EMI causing system upset

The transitional probabilities '*q*' and '*r*'; from EMI absence to EMI presence and from EMI presence to EMI absence during one step of duration '*Ts*' can be calculated based on the assumptions of Poisson process for the arrival process and exponential distribution for the duration.

$$q = \int_0^{T_s} \lambda_e e^{-\lambda_e t} dt = 1 - e^{-\lambda_e T_s}$$
$$r = \int_0^{T_s} \mu_e e^{-\mu_e t} dt = 1 - e^{-\mu_e T_s} \quad \textbf{(5.3)}$$

Eqn. (5.3) [28] describes the transitional probabilities with a Poisson occurrence rate of 'λ' and exponential duration rate of 'μ'. The stationary probability of failure as given in Equation 2 of [28] is

$$\Pi_f = \frac{pq}{q+r} \qquad \textbf{(5.4)}$$

From equation 5.4, it is can be seen that the stationary probability will be equal to the conditional probability '*p*' when EMI is present constantly. When the transition happens from an EMI absence state to an EMI present state where the failures happen, the stationary probability is given by $q/q+r$. The conditional probability '*p*' is calculated from the Rayleigh distribution (for the specific case discussed in this study) as explained before. Hence, the stationary probability of failure reduces to calculating the probability of EMI threat due to the observable crossing the threshold with an assumption that the probability of threat in a specific time frame is independent of its prior states.

To calculate *q* and *r*, the electromagnetic environment has to be observed over a period of time. As an example, a site survey of the EME can be considered to estimate the values of *q* and *r* under the assumption that the arrival process of the EMI follows a Poisson process and the duration for which the EMI exists follows an exponential distribution. The values of *q* and *r* will vary with environment and threshold levels which will be evident from the site survey. Once the EMI occurrence probabilities are determined, the conditional probability of failure along with the type of EMI failure will result in calculating the overall failure probability of the system.

3- Stage Markov model for long term probabilities

A more realistic failure model can describe a burst of upsets in the presence of EMI depending on whether or not an upset occurs during the previous time frame. A Markov chain model with three states: transition from EMI absence to presence and transitioning from presence to failure or no failure state with the elimination of the EMI presence state can describe the aspects of each transition. The assumption is that once EMI is present then it either causes a system failure or no failure. The two conditional probabilities of failure when the system is in no failure and failure state can be expressed as 'p_1' and 'p_2'. The Markov chain of this three state process is given in Figure 5.13 [28]

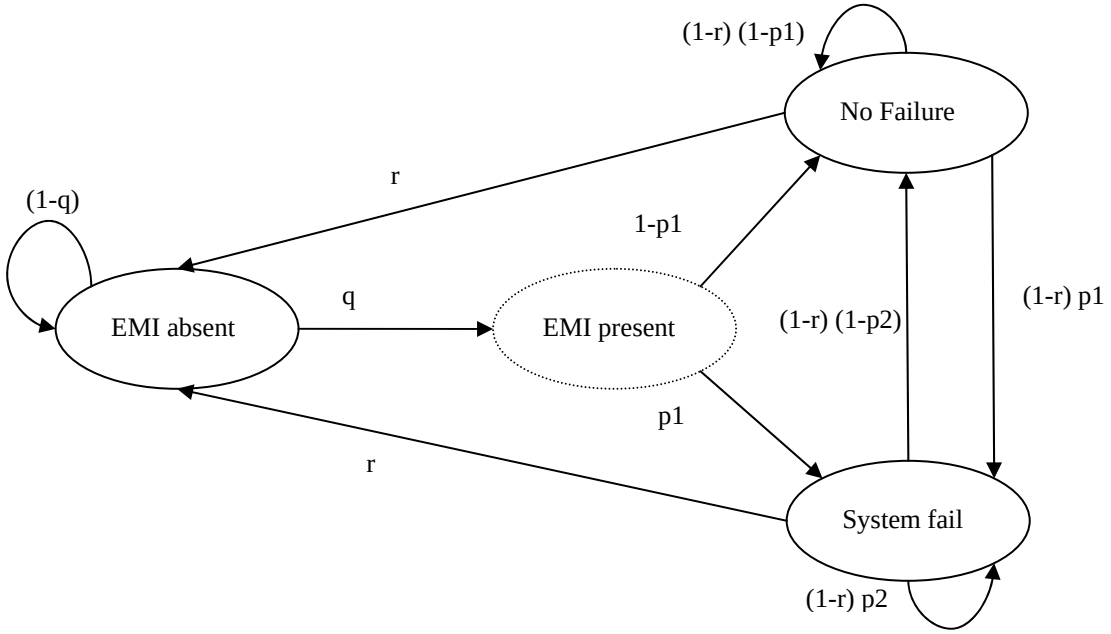

Figure 5. 14 Three stage Markov chain model for EMI causing system upset

The stationary probability of the failure state from the three state process is given as [28]

$$\Pi_F = \frac{q}{q+r}\frac{p_1}{[1-(1-r)(p_2-p_1)]} \qquad \textbf{(5.5)}$$

Following the Markov chain model, and using the values calculated from the distribution of the induced currents as threshold, the stationary probability of the system exists in the failure state can also be calculated. If the measured current exceeds the threshold, it is recorded as a threat otherwise it is recorded as a no threat. Following the procedure established in [28], the probability of threat at each frequency (considering 100 different tuner positions or independent measurement points) can be calculated using Equation 5.3.

To summarize, in this chapter the probability of threat was calculated using the current distribution measured with a wire located inside a cavity. The cavity was excited through an aperture located on one of its walls and subjected to EM energy from all different directions and polarizations by performing the measurement inside the reverberation chamber. For this specific arrangement and frequency of interest, the current seems to follow a Rayleigh distribution which mostly will be true for all overmoded cavities (electrically large and complex) and the EMI arrival times assumed to follow a Poisson distribution. Thus the probability of failure will be the product of the conditional probability that the induced current that will exceed the threshold and the probability of EMI presence.

Though probability distributions have been developed for the field and power measured inside a reverberation chamber, only in this work a distribution for a current induced on the wire is derived. A procedure to develop the distribution for any observable has been established. A probability model has been provided for peak, average and transition types

of EMI. The decoupling of the EMI presence and EMI effects to cause a failure has been an unexplored territory and only in this work a meaningful approach has been proposed to handle such problems. By no means the work that is proposed here is complete and should only be considered as a starting point to build more EMI failure models. The models have to be extended or new models developed for other types of EMI in the future work. The novelty in this work comes from marrying the distribution of the observable and the EMI threat model to arrive at a probability of failure. From the methodology that will be established, a class of distributions for the observable and a family of distributions for types of EMI can be developed which will help in assessing the probability of failure of a system given a threshold and type of EME the system is operating in. The long term probabilities of how long the system would exist in a failure state can also be calculated from a 3 stage Markov model.

Chapter 6

6.0 SUMMARY AND FUTURE WORK

Different test techniques that are available for assessing the EME of any space have been explored. Both frequency and time domain techniques were used to extract information about the EME. An initial focus was placed on measurements inside a reverberation chamber where the procedures for creating/assessing the EME are well established. From measurements, it was shown that both *Q* and reverberation distance could be measured efficiently with reasonable accuracy. Though the reverberation distance measured with both time and frequency domain techniques were comparable, determination of *Q* posed a problem.

When this analysis was extended to rooms and empty spaces and source stirring was used to stir the fields inside, the difference between the measured *Q*'s existed but the time domain data over-predicted the *Q* unlike the measurements inside the chamber where the time domain technique under-predicted the *Q* compared to frequency domain technique. In order to investigate the difference in *Q* that existed in our measurements more rigorous measurements were performed in the SMART 80 chamber at multiple frequencies. From the analysis it was clear that the time domain prediction of *Q* disregards the efficiency of

and the impedance mismatch of the antennas. If the efficiency and the impedance mismatch are factored in the frequency domain measurements, the *Q* values could be similar.

A novel way of measuring the efficiency of the antenna was also developed from this work by comparing the frequency and time domain measurements. In essence, the advantage of a time domain method in the estimation of time decay constant of the chamber is that the direct path components can be windowed out so that only the multipath effects are considered. The effects of antennas that are used in these measurements can be separated in time domain measurements which enable the measurement of antenna properties while in the frequency domain approach the antenna effects are inseparable.

The need for independent samples while calculating the statistical distributions of the measured data was discussed in Chapter 3. Variations in the estimation can exist just from the criterion used to determine independence and also because of the nature of statistical sampling. The key issue of independent vs. measured samples at low frequencies of the chamber needs to be studied while performing tests at lower frequencies. Loading complicates the issue of independent sampling. The effects of decreased available independent samples with increased loading were observed via measurements. The effects of loading on uniformity of the chamber were also discussed in detail.

One way to increase the number of independent samples by introducing a second tuner was investigated and preliminary results are documented. The size and placement of the second tuner with respect to the first tuner was investigated via measurements. A potential to reduce the low frequency limit of the chamber by increasing the complexity of the cavity and not size was demonstrated. More measurements were performed to support the effect of the second tuner on lowering the low frequency limit of the chamber as well. When the second tuner is electrically small, there will be a marginal increase in the performance of the chamber at lower frequencies. As the size of the second tuner gets bigger, the performance of the chamber gets better. If the chamber, by its physical size, cannot support the low frequencies that are required, the size of the tuner is not significant. The need for in band antennas for low frequencies was also observed in the measurements.

The problem of current coupling onto a wire located inside a cavity was analyzed in Chapter 4. The need to use statistical methods to analyze complex cavity problems was discussed by looking at the mode density of the cavity and the impact of the wire by its presence inside the cavity. The distributions of power and field at any point inside an overmoded cavity when the measurement probe was close to the walls and corner were verified. A methodology to measure the current induced on the wire with a simple S-parameter measurement was developed and preliminary results were well within reasonable expectations.

The current induced on a wire placed inside a cavity with an aperture serving as a coupling mechanism was measured and simulated and reasonable comparison was obtained between the two. The current on the wire when the wire is terminated by arbitrary impedance was projected from the measured short circuit current. The difference in the induced current when the wire was short circuited and terminated by impedance provided an insight to determine what the load termination should be in order to subdue the effects of the cavity resonance on the wire.

The distribution of the measured short circuit current with variation in the angles of incidence of the source was calculated in Chapter 5. The wire location was changed to three positions inside the cavity and the same set of measurements were repeated for a different size of the aperture. The current followed a Rayleigh distribution irrespective of the mode regime for the variation. The probability of the current exceeding a certain arbitrary threshold value was calculated for the entire frequency band of interest or particular frequency following the distribution of the current. A threat model for a peak, average, transition types of EMI and a special case of bursty upsets was developed using a Markov chain model. The inter-arrival times of the EMI follows a Poisson model while the duration follows an exponential model. This information was utilized to develop the probability of failure of the system.

Assuming the occurrence of system threat when the threshold is crossed, the probabilities of failure for different threshold currents were calculated for the frequency region of interest from the measured data in a reverberation chamber. Assuming the two

probabilities (Probability of current - observable exceeding a certain value and Probability of threat) to be independent, the probability of failure i.e. the net probability that the system will fail given the threshold has been exceeded for the induced current deduced from the distribution of the current and the threat probability was calculated. In the future, the EMI models developed in this work need to be validated with working systems. Assuming a certain kind of malfunction to be a failure, the probability of the observable exceeding a threshold and the type of EMI threat along with its threat probability must be calculated to see the probability of failure due to a certain event.

6.1 Novel aspects of this work

1. An efficient and robust procedure to calculate the distance at which direct path power is no longer the dominant contributor for different EME has been established by this work.
2. With regard to the difference in the *Q* values in time and frequency domain techniques, though described in the literature, this work is the only one to discuss in detail the reason for the difference.
3. A novel way to measure the antenna efficiency under operating conditions was shown.
4. The difference in the estimation of independent samples based on the criterion chosen and the number of measured samples was clearly brought out in this work.
5. The effect of loading on IS is mentioned in literature but this work investigated the impact in a methodical fashion and distinctly addressed the issues of impact

on uniformity. There is not always a one to one correlation between loading and independent samples and uniformity which was identified in this work.

6. A novel way to increase the number of independent samples and a lowering of the low frequency limit of the chamber by the use of a smaller second tuner is discussed in this work. The size of the second tuner and its impact on the low frequency operation of the chamber was also investigated.
7. A procedure to measure current induced on a wire located inside a cavity was established and for the variation on incidence angles, a probability distribution of the current as a function of frequency was developed and verified in this study.
8. The distribution function has been developed for some cases, answering the question of the probability of the induced current value exceeding a certain threshold at some frequency or a set of frequencies which provides an estimate on how much shielding will be required. The major focus of this work was on the development of the methodology that is sufficiently general to obtain the distribution of any observable.
9. Some types of EMI were discussed and a Markov chain model was used to model EMI. From the model, the probability of threat to a system due to EMI was established.
10. The probability of failure of a system due to EMI inducing a current on the wire and that current exceeding a certain threshold was calculated for the first time in this work.

11. The procedure developed could be used in different scenarios and from a class of distributions developed for each scenario, the probability of threat and probability of failure of a system due to EMI can be calculated.

6.2 Future work

The difference between frequency and time domain quality factor has to be resolved by performing detailed analysis on the measurable inside the cavity. In this work, the difference has been attributed to the coupling efficiency between the antennas and the chamber. Validation of this coupling efficiency is necessary.

The effect of loading on independent samples as covered in this work is an interesting topic and has practical implications on testing. More work need to be done to understand the impact at the low frequency limits of the chamber and understanding the relationship between independent samples and uniformity with loading. The size of the secondary tuner and the use of a secondary tuner to push the low frequency limit of the chamber need to be investigated with more measurements and by using different types and sizes of the secondary tuner.

Other observables of the cavity like the power density could be measured with minimum perturbation of the field and probability models for those observables could be developed. In this work only a limited number of random variables have been varied to generate different distribution functions, this could be extended to identifying and varying other random variables and generating other distribution functions.

Though a model was proposed to address the change of state from EMI absence to EMI presence and its effect on causing system failures, only the conditional probability of failure of a system in EMI presence have been explored in this study. More measurements need to be performed on real systems when there is a state change from EMI absence to EMI presence and vice versa. Some types of failure models that have been proposed in this work need to be verified via measurements on operational systems. Different types of failures other than the ones proposed in this work need to be identified and probability models have to be developed for those to be used in conjunction with the observable probabilities to compute the overall probability of failure limits.

REFERENCES

[1] Hill, D. A., "Plane Wave Integral Representation for the Fields in Reverberation Chamber," *IEEE Transactions on Electromagnetic Compatibility,* vol. 40(3), pp. 209-217, August 1998.

[2] D. A. Hill, Mark T. Ma, Arthur Ondrejka, Bill F. Riddle, Myron F. Crawford and Robert T. Johnk., "Aperture Excitation of Electrically Large Cavities," NIST Technical Note 1361.

[3] T. H. Lehman, G. J. Freyer, M .O. Hatfield, J. M. Ladbury and G. Koepke, "Verification of Fields Applied to an EUT in Reverberation Chamber Using Numerical Modeling," *International Symposium of Electromagnetic Compatibility*, pp. 28-33, 1998.

[4] "Test and Measurement Techniques - Reverberation Chamber Test Methods." *Electromagnetic Compatibility Part 4-21.*

[5] "Environmental Conditions and Test procedures for Airborne Equipment." *RTCA DO 160 E*

[6] Christopher L. Holloway, David A. Hill, John M. Ladbury, Perry F. Wilson, Galen Koepke and Jason Coder, "On the Use of Reverberation Chamber to Simulate a Rician Radio Environment for the Testing of Wireless Devices," *IEEE Transactions on Antennas and Propagation*, vol. 54(11), pp: 3167-3177, November 2006.

[7] J.B. Andersen, J. O. Nielsen,G. F. Pedersen, G. Bauch and M. Herdin., "Room Electromagnetics," *IEEE Antennas and Propagation Magazine*, vol 49(2), pp.27-33, April 2007.

[8] Robert E. Richardson, "Reverberant Microwave Propagation," *NSWCDD/TR-08/127*, October 2008.

[9] Luk Arnaut, "Time-Domain Measurement and Analysis of Mechanical Step Transitions in Mode-Tuned Reverberation: Characterization of Instantaneous Field," *IEEE Transactions on Electromagnetic Compatibility*, vol. 49(4), pp. 772-784, 2007.

[10] Kunthong, J. and Bunting, C.F., "Source-stirring and mechanical-stirring reverberation chamber measurement comparison for 900MHz and 1800MHz," *International Symposium on Electromagnetic Compatibility*, pp. 193-196, August 2009.

[11] Kunthong, J. and Bunting, C.F., “Statistical characterization of the 900MHz and 1800MHz indoor propagation using reverberation source stirring technique,” *International Symposium on Antennas and Propagation*, pp. 1-4, June 2009.

[12] Hill, D. A. and John M. Ladbury, “Spatial Correlation Functions of Fields and Energy Density in a Reverberation Chamber,” *IEEE Transactions on Electromagnetic Compatibility*, vol. 4(1), February 2002.

[13] Mark Johnson, Michael Hatfield, Michael Slocum, Arthur Ondrejka, Robert Johnk and Gustav Freyer, “Phase II Demonstration Test of the Electromagnetic Reverberation Characteristics of a Large Transport Aircraft,” *NSWCDD/TR-97/84*, Sep 1997.

[14] David A. Hill, “Electromagnetic Fields in Cavities,” Wiley Publications, 2009.

[15] Olof Lunden, Mats Backstrom and Niklas Wellander, “Evaluation of Stirrer Efficiency in FOI Mode Stirred Reverberation Chambers,” November 2001.

[16] Personal communication: Greg Tait

[17] Paul A. Johnson and Kevin R. Goldsmith, “An Experimental Study of the Placement An Aircraft Inside A Large Welded Zinc-Plated Steel Electromagnetic

Reverberation Chamber, “Digital *Avionics Systems Conference Proceedings*, vol. 1, 1998.

[18] Paul Hallbjorner, Ulf Carlberg, Kent Madsen and Johan Andersson, “Extracing Electrical Material Parameters of Electrically Large Dielectri Objects from Reverberation Chamber Measurements of Absoption Cross Section,” *IEEE Transactions on Electromagnetic Compatibility*, vol. 47(2), pp. 291-303, May 2005.

[19] Zhang DM, Li Ep, David Yeo, Chow WS and James Quek, “Influences of Loading Absorber on the Performances of a Reverberation Chamber,” *International Symposium on Electromagnetic Compatibility*, vol. 1, pp. 279-281, August 2003.

[20] Rajamani V., Bunting C. F. and West, J. C., “Calibration of a Numerically Modeled Reverberation Chamber,” *International Symposium on Electromagnetic Compatibility*, pp. 87-91, August 2009.

[21] Arnaut, Luk., “Operation of Electromagnetic Reverberation Chambers with Wave Diffractors At Relatively Low Frequencies,” *IEEE Transactions on Electromagnetic Compatibility*, vol. 43(4), pp. 637-653, November 2001.

[22] Arnaut, Luk., “Effect of Size, Orientation and Eccentricity of Mode Stirrers On Their Performance in Reverberation Chambers,” *IEEE Transactions on Electromagnetic Compatibility*, vol. 48(3), pp. 600-602, August 2006.

[23] John Ladbury, Galen Koepke and Dennis Camell, “Evaluation of the NASA Langley Research Center Mode-Stirred Chamber Facility,” *NIST Technical Note 1508*, January 1999.

[24] Breakall. J, and Hudson .H, “The Equivalent Current Measurement Technique and its Comparison With Current Probe Methods,” *IEEE Transactions on Antennas and Propagation*, vol. 34(1), pp. 119-122, 1986.

[25] Holloway, C. L., Hill, D. A., Ladbury, J., Koepke, G. and Garzia, R., “Shielding Effectiveness Measurements of Materials Using Nested Reverberation Chambers,” *IEEE Transactions on Electromagnetic Compatibility*, vol. 45(2), May 2003.

[26] M. L. Shooman., A Study of Occurance Rates of Electromagnetic Interference to Aircraft With A Focus On HIRF,” *NASA CR – 194895*, April 1994.

[27] Steven Gray, Oscar Gonzalez and Mustafa Dogan, “Stability Analysis of Digital Linear Flight Controllers Subject to Electromagnetic Disturbances,” *IEEE Transactions on Aerospace and Electronic Systems*, vol. 36(4), pp. 1204-1218, October 2000.

[28] Hagabae Kim, Allan L. White and Kang G. Shin, “Effects of Electromagnetic Interference on Controller-Computer Upsets and System Stability,” *IEEE Transactions on Control Systems Technology*,” vol. 8(2), pp. 351-357, March 2000.

[29] D. Middleton, “Statistical-Physical Models of Electromagnetic Compatibility,” *IEEE Transactions on Electromagnetic Compatibility*,” vol. 19(3), 1977.

[30] P. Ng, R. Dalke and J. Horembala, “Application of Triggered Lightening Numerical Models to the F106b and Extension to other Aircraft,” *NASA CR – 4207*, December 1998.

[31] Broster, Burns and Rodriguez-Navas, “Timing Analysis of Real-Time Communication Under Electromagnetic Interference,” *Real Time Systems*, vol. 30, pp. 55-81, 2005.

[32] Gus Freyer, Charles F. Bunting and Vignesh Rajamani, “Reverberation Chamber Theory and Experiment Short Course Notes.”

[33] Personal Communication: Buddy Coffey

[34] Jansson, L. and Backstrom, M., “Directivity of Equipment and its Effect on Testing in Mode-Stirred and Anechoic Chamber,” *International Symposium on Electromagnetic Compatibility*, vol. 1, pp. 2-6, August 1999.

[35] Corona, P., Ferrara, G. and Migliaccio, M., “A Spectral Approach for the Determination of The Reverberating Chamber Quality Factor,” *IEEE Transactions on Electromagnetic Compatibility*,” vol. 40(2), pp. 145-153, May 1998.

[36] Hill, D. A., "Boundary Fields In Reverberation Chambers," *IEEE Transactions on Electromagnetic Compatibility*," vol. 47(2), May 2005.

[37] Yi Huang and J. T. Zhang, "Field Measurements Inside Reverberation Chamber," *International Symposium on Antennas and Propagation*, pp. 20-25, June 2004.

[38] Corona, P., Ferrara, G. and Migliaccio, M., "Generalized Stochastic Field Model for Reverberation Chambers," *IEEE Transactions on Electromagnetic Compatibility*," vol. 44(4), Nov 2004.

[39] Hill, D. A., "Linear Dipole Response in a Reverberation Chamber," *IEEE Transactions on Electromagnetic Compatibility*," vol. 41(4), pp. 365-368, Nov 1999.

[40] Gregory Tait, Michael Slocum and Robert Richardson, "On Multipath Propagation in Electrically Large Reflective Spaces," *IEEE Antennas and Wireless Propagation Letters*, vol. 8, pp. 232-235, 2009.

[41] Holloway, C. L., Hill, D. A., Ladbury, L. M. and Koepke, G., "Requirements for an Effective Reverberation Chamber: Unloaded or Loaded," *IEEE Transactions on Electromagnetic Compatibility*," vol. 48(1), pp. 187-194, Feb 2006.

[42] Cerri, G., Primiani, V. M., Pennesi, S. and Russo, P., "Source Stirring Mode for Reverberation Chambers," *IEEE Transactions on Electromagnetic Compatibility*," vol. 47(4), pp. 815-823, Nov 2005.

[43] Orjubin, G., Richalot, E., Mengue, S. and Picon, O., "Statistical Model for an Undermoded Reverberation Chamber," *IEEE Transactions on Electromagnetic Compatibility*," vol. 48(1), pp. 248-251, Feb 2006.

[44] Holland, R. and John R. H., "Statistical response of EM-driven Cables Inside an Overmoded Enclosure," *IEEE Transactions on Electromagnetic Compatibility*," vol. 40(4), pp. 311-324, Nov 1998.

[45] Koepke, G., Hill, D. A. and Ladbury, J. M., "Directivity of the Test Device in EMC Measurements," *International Symposium on Electromagnetic Compatibility*, vol. 2, pp. 21-25, August 2000.

[46] Tyagi, S. K., "Transient Response of Electronic Devices and Their Failure Mechanism," *International Conference on Electromagnetic Compatibility*, pp. 497-499, December 1999.

[47] Bendel, R., "Application of the Statistical Method and Quality Factor Decomposition to Determine Microwave Fields Inside an Equipment Cavity," *International Symposium on Electromagnetic Compatibility*, vol. 2, pp. 345-350, August 2006.

[48] Wellander, N., Lunden, O. and Backstrom, M., "Design Parameters for Efficient Stirring of Reverberation Chambers," *International Symposium on Electromagnetic Compatibility*, vol. 2, pp. 263-268, August 2006.

[49] Dawson, J. F., Konefal, T., Robinson, M. P., Marvin, A. C., Porter, S. J., and Chirwa, L. C., "Field Statistics in an Enclosure with an Aperture – Effect of Q-factor and Number of Modes," *International Symposium on Electromagnetic Compatibility*, vol. 1, pp. 141-146, August 2005.

[50] Orlenius, C., Franzen, M., Kildal, P. S. and Carlberg, U., "Investigation of Heavily Loaded Reverberation Chamber for Testing of Wideband Wireless Units," *International Symposium on Antennas and Propagation*, pp. 3569-3572, June 2006.

[51] Clegg, J., Marvin, A. C., Dawson, J. F. and Porter, S. J., "Optimization of Stirrer Designs in a Reverberation Chamber," *IEEE Transactions on Electromagnetic Compatibility*," vol. 47(4), pp. 824-832, Nov 2005.

[52] Carpenter, D., "Statistical Electromagnetics: An End-Game to Computational Electromagnetics," *International Symposium on Electromagnetic Compatibility*, vol. 3, pp. 736-741, August 2006.

[53] Kempf D. R. and Brezinski K. A., "Using Reverberation Techniques for Testing an Intercommunications System on a Navy Aircraft," *20th Digital Avionics Systems Conference*, vol. 1, 2001.

[54] G. J. Freyer, T. H. Lehman, J. M. Ladbury, G. Koepke and M .O. Hatfield, "Verification of Fields Applied to an EUT in Reverberation Chamber Using Statistical Theory," *International Symposium of Electromagnetic Compatibility*, pp. 34-38, 1998.

[55] Charles K. Alexander and M. N. O. Sadiku, "*Fundamentals of Electric Circuits*," McGraw Hill, 3rd Edition.

[56] Personal communication: Bob Johnk

[57] Robert W. Young, "Sabine Reverberation Equation and Sound Power Calculations," *Journal of the Acoustical Society of America*, vol. 31, no. 7, July 1959

[58] Personal communication: Bob Richardson

[59] Personal communication: Gus Freyer

[60] Lee, C.S., Duffy, A. and Lee, C., “Antenna Efficiency Measurements in a Reverberation Chamber Without the Need for a Reference Antenna,” ,” I*EEE Antennas and Wireless Propagation Letters*, vol 7, pp. 448-450, 2008

[61] Khaleghi, A., “Time-Domain Measurement of Antenna Efficiency in Reverberation Chamber,” *IEEE Transactions on Antennas and Propagation*, vol. 57(3), pp. 817-821, 2009

[62] Piette, M., “Antenna radiation efficiency measurements in a reverberation chamber,” *Proceedings Asia Pacific Radio Science Conference*, 2004

[63] Conway, G.A.; Scanlon, W.G.; Orlenius, C.; Walker, C.;, “In Situ Measurement of UHF Wearable Antenna Radiation Efficiency Using a Reverberation Chamber,” I*EEE Antennas and Wireless Propagation Letters*, vol 7, pp. 271-274, 2008

[64] http://www.uekae.tubitak.gov.tr/img/tempest/acik_hava_test_alani_buyuk.gif

[65] http://www.parkes.atnf.csiro.au/observer_info/rfi/images/anechoic_horn.jpg

[66] http://www.cetecom-ict.de/gfx/halle_f.jpg

[67] http://www.temconsulting.com/support%20pages/gtem_background.htm

[68] http://images.google.com/imgres?imgurl=http://www.mttco.co.jp/msm/emc/shaff/img/shaff_04_01.jpg&imgrefurl=http://www.mttco.co.jp/msm/emc/shaff/shaff_04.html&h=300&w=420&sz=66&hl=en&start=10&tbnid=gCtH_kNafGj75M:&tbnh=89&tbnw=125&prev=/images%3Fq%3DGTEM%26gbv%3D2%26svnum%3D10%26hl%3Den

[69] Genender, E., Holloway, C.L., Remley, K.A., Ladbury, J., Koepke, G. and Garbe, H., "Use of Reverberation Chamber To Simulate The Power Delay Profile of a Wireless Environment," *International Symposium on Electromagnetic Compatibility*, EMC Europe 2008.

[70] Guillemin. E. A., "The Mathematics of Circuit Analysis," MIT press, Seventh printing, July 1962.

Appendix 1

Measured Received power Statistics.

Horn antenna

Relative Evaluation of Candidate Models

Model	Relative Score		Parameters
1 - Weibull(E)	100.00	Location	3.00461e-6
		Scale 6.06882e-3	
		Shape 0.95722	
2 - Weibull	93.06	Location	0.00000
		Scale 6.08401e-3	
		Shape 0.96150	
3 - Gamma(E)	90.28	Location	3.00461e-6
		Scale 6.58229e-3	
		Shape 0.94037	

Absolute Evaluation of Model 1 - Weibull(E)

Evaluation: Good

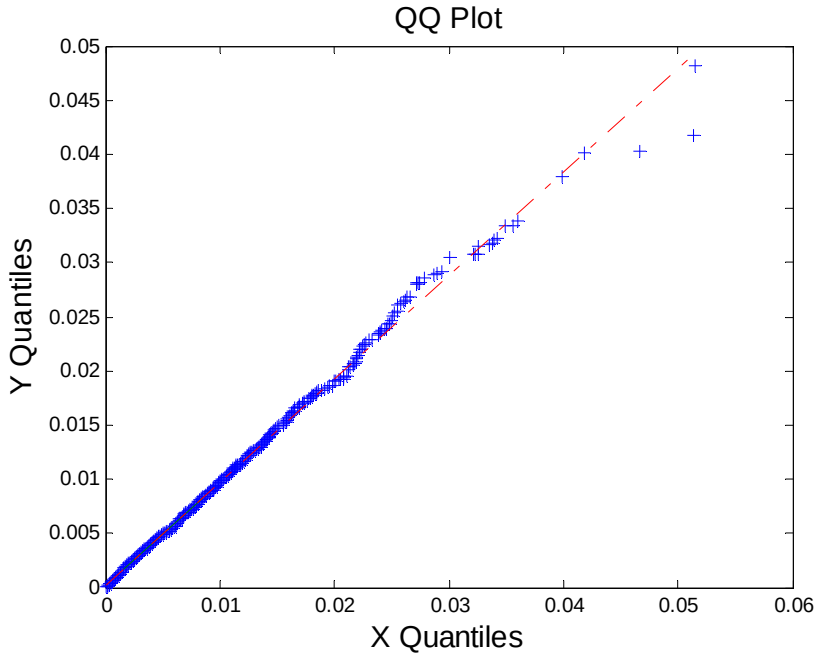

Monopole at the geometric center of the chamber

Relative Evaluation of Candidate Models

Model	Relative Score		Parameters
1 - Weibull	96.88	Location	0.00000
	Scale	1.08204e-4	
	Shape	1.04087	
2 - Weibull(E)	93.75	Location	4.97737e-8
	Scale	1.07714e-4	
	Shape	1.03007	
3 - Gamma	89.06	Location	0.00000
	Scale	1.02475e-4	
	Shape	1.03958	

Absolute Evaluation of Model 1 - Weibull
Evaluation: Borderline

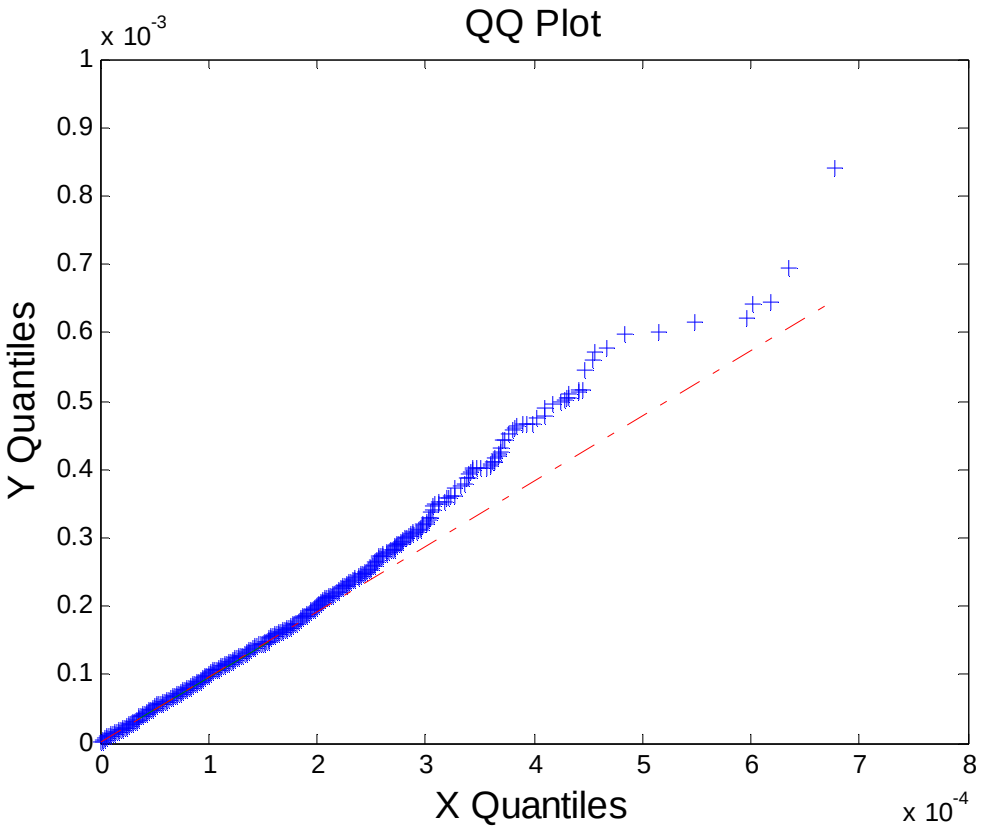

Monopole parallel to one wall

Relative Evaluation of Candidate Models

Model	Relative Score		Parameters
1 - Gamma(E)	88.24	Location	2.98386e-8
	Scale	1.55161e-4	
	Shape	1.03941	
2 - Weibull(E)	88.24	Location	2.98386e-8
	Scale	1.63146e-4	
	Shape	1.02889	
3 - Exponential(E)	85.29	Location	2.98401e-8
	Scale	1.61276e-4	

18 models are defined with scores between 1.47 and 88.24

Absolute Evaluation of Model 1 - Gamma(E)

Evaluation: Good

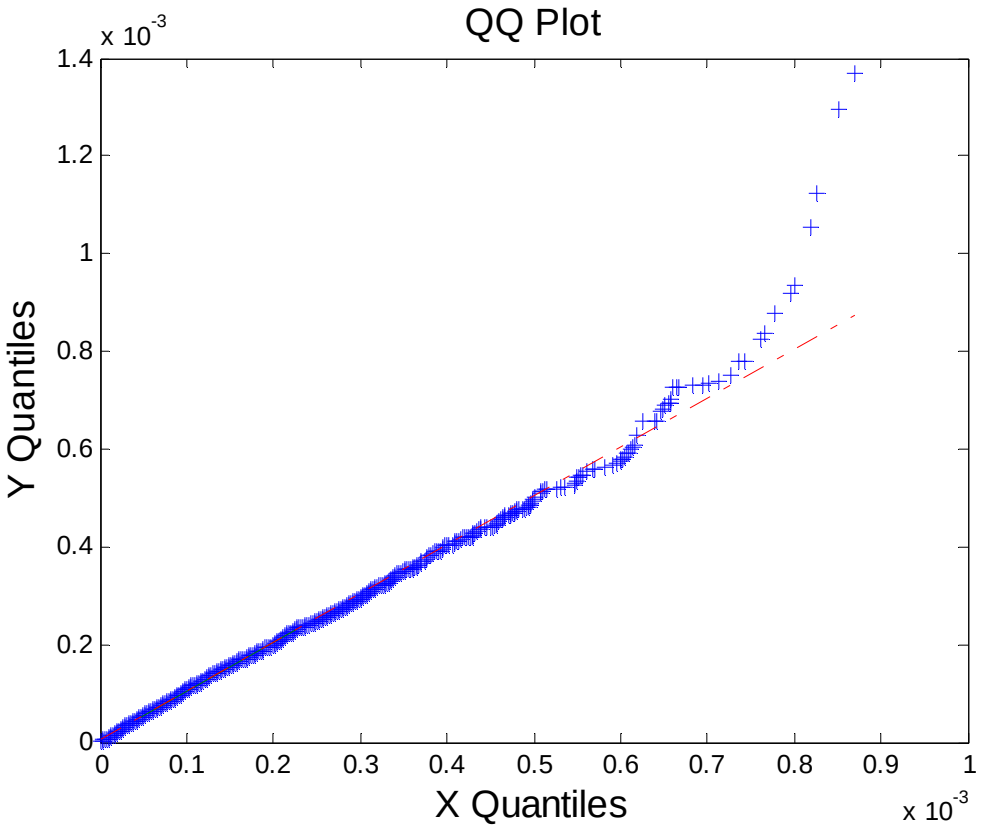

Monopole in a corner

Relative Evaluation of Candidate Models

Model	Relative Score		Parameters
1 - Gamma(E)	97.06	Location	7.27625e-9
	Scale	2.02286e-5	
	Shape	0.91607	
2 - Gamma	91.18	Location	0.00000
	Scale	2.00102e-5	
	Shape	0.92643	
3 - Weibull(E)	89.71	Location	7.27625e-9
	Scale	1.81174e-5	
	Shape	0.95039	

Absolute Evaluation of Model 1 - Gamma(E)
Evaluation: Good

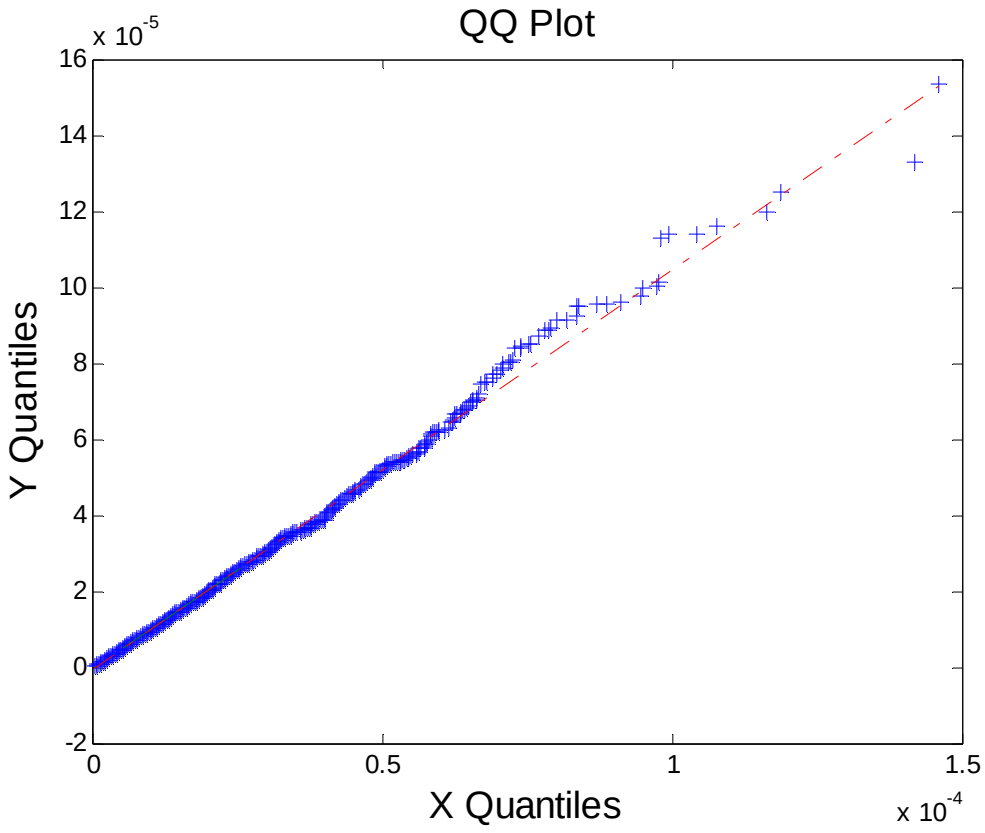

Measured E field Statistics

Horn antenna

Relative Evaluation of Candidate Models

Model	Relative Score		Parameters
1 - Weibull	97.50	Location	0.00000
	Scale	28.95348	
	Shape	1.92300	
2 - Weibull(E)	97.50	Location	0.63881
	Scale	28.15932	
	Shape	1.85588	
3 - Gamma	90.00	Location	0.00000
	Scale	8.54823	
	Shape	3.00121	

Absolute Evaluation of Model 1 - Weibull
Evaluation: Good

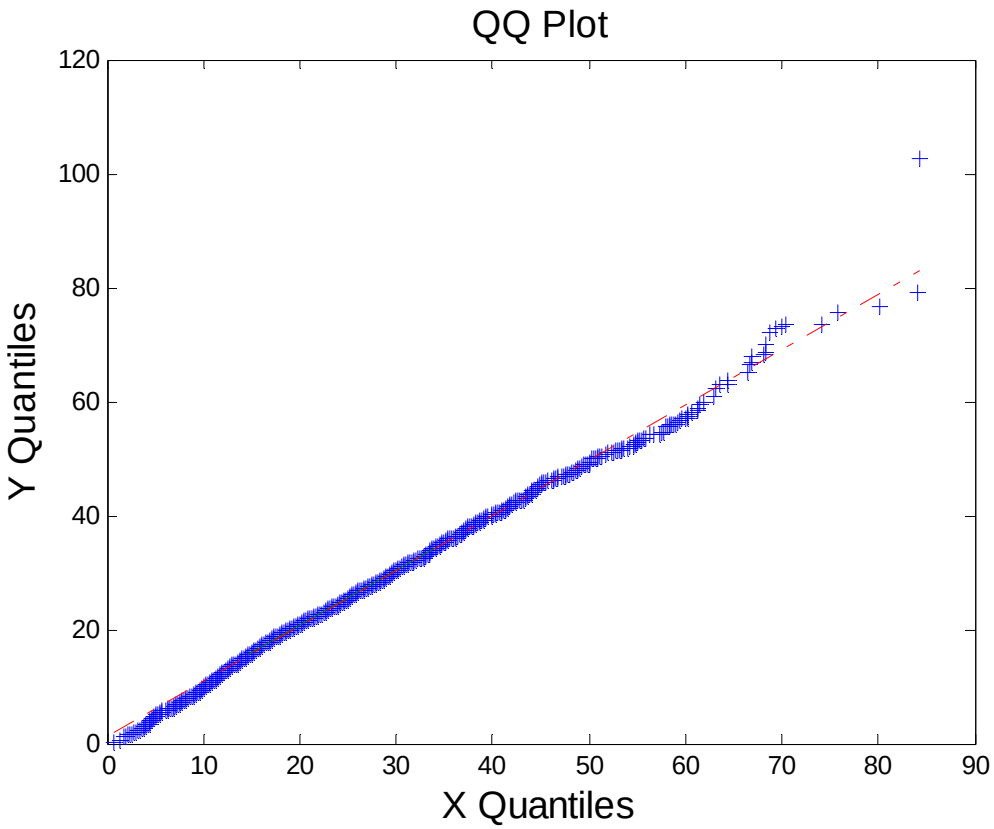

Monopole at the geometric center

Relative Evaluation of Candidate Models

Model	Relative Score		Parameters
1 - Weibull	100.00	Location	0.00000
	Scale 3.86124		
	Shape 2.08173		
2 - Weibull(E)	95.24	Location	0.08281
	Scale 3.75141		
	Shape 1.98391		
3 - Gamma	89.29	Location	0.00000
	Scale 1.06923		
	Shape 3.20288		

Absolute Evaluation of Model 1 - Weibull
Evaluation: Borderline

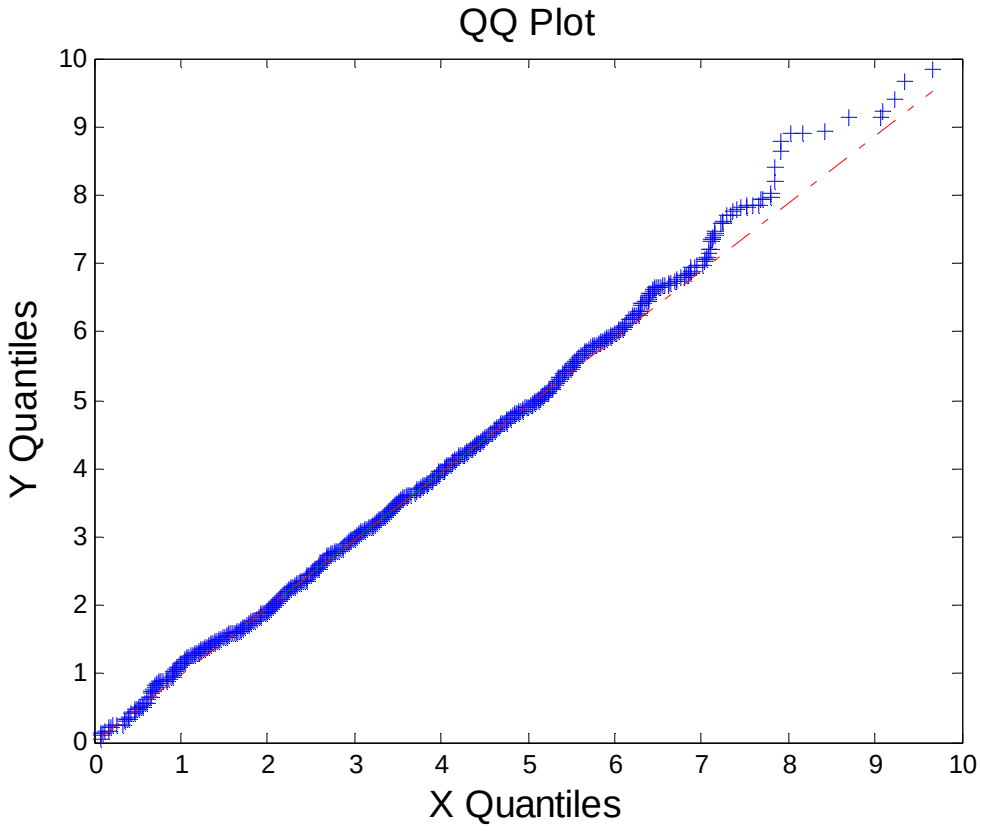

Monopole corner

Relative Evaluation of Candidate Models

Model	Relative Score		Parameters
	Relative		
1 - Weibull	100.00	Location	0.00000
	Scale	1.58203	
	Shape	1.91020	
2 - Weibull(E)	95.00	Location	0.03154
	Scale	1.54191	
	Shape	1.84403	
3 - Gamma	90.00	Location	0.00000
	Scale	0.48998	
	Shape	2.86473	

Absolute Evaluation of Model 1 - Weibull
Evaluation: Good

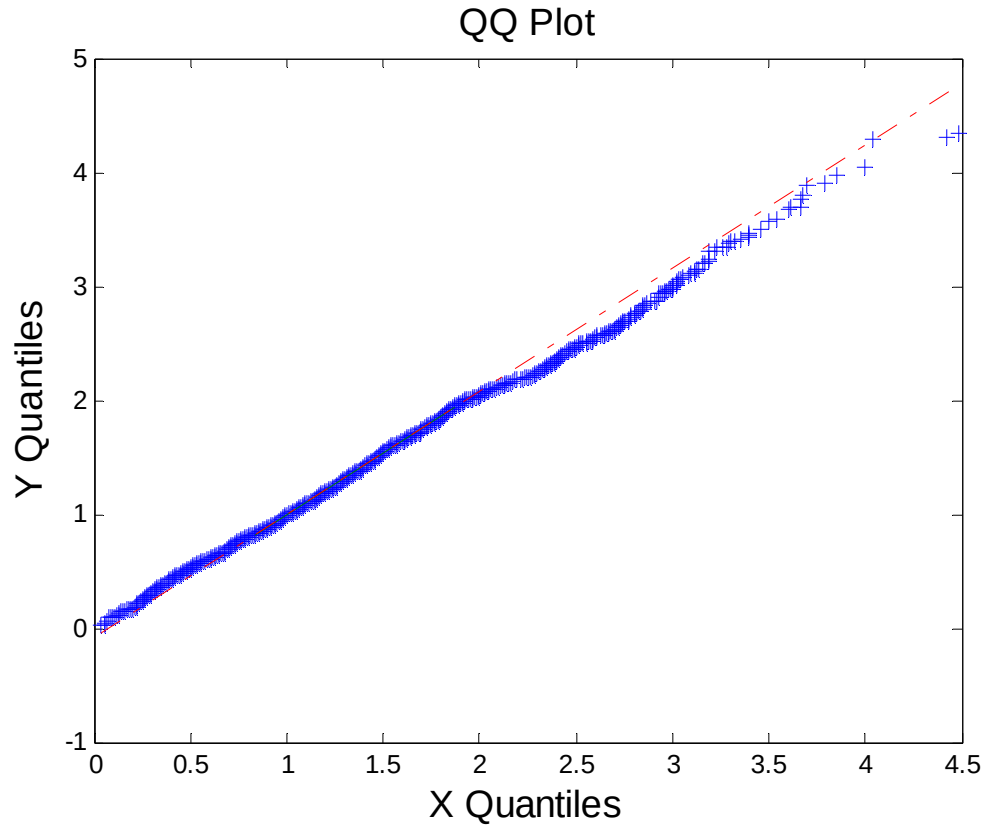

Appendix 2

Simulated Received Power Statistics

1-power

Relative Evaluation of Candidate Models

Model	Relative Score		Parameters
1 - Weibull	94.12	Location	0.00000
	Scale	1.97339	
	Shape	0.98130	
2 - Weibull(E)	91.18	Location	2.43615e-4
	Scale	1.96857	
	Shape	0.97595	
3 - Gamma	89.71	Location	0.00000
	Scale	2.06534	
	Shape	0.96322	

Absolute Evaluation of Model 1 - Weibull
Evaluation: Good

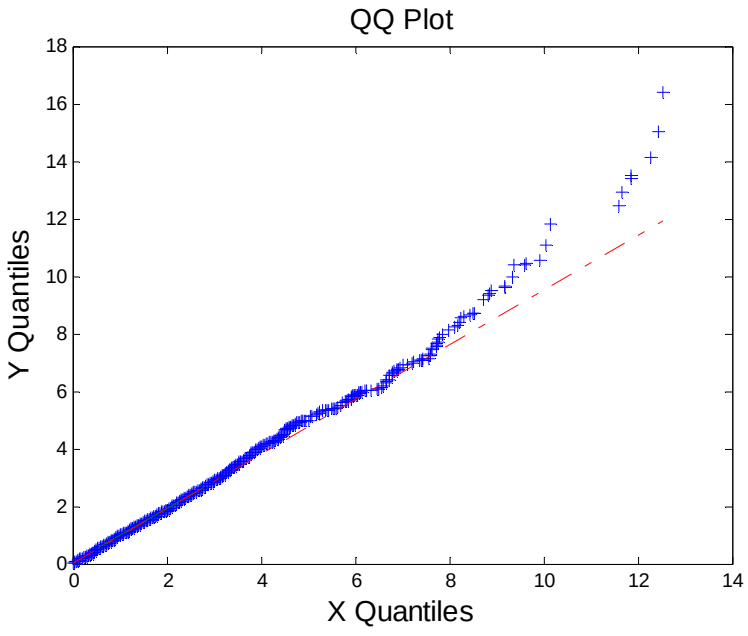

2-power

Relative Evaluation of Candidate Models

Model	Relative Score		Parameters
1 - Chi-Square(E)	94.12	Location	6.96262e-5
	d.f.	2.04622	
2 - Gamma(E)	86.76	Location	6.96262e-5
	Scale	2.03103	
	Shape	1.01350	
3 - Gamma	77.94	Location	0.00000
	Scale	2.01372	
	Shape	1.02225	

Absolute Evaluation of Model 1 - Chi-Square(E)
Evaluation: Good

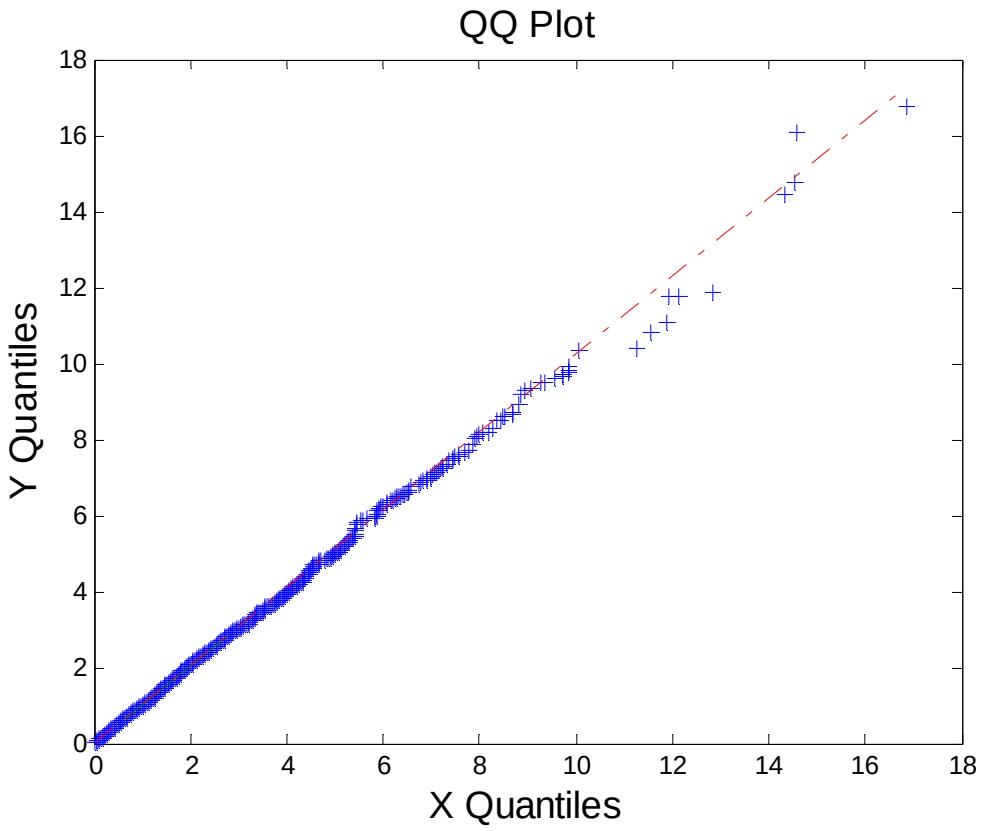

3-power

Relative Evaluation of Candidate Models

Model	Relative Score		Parameters
1 - Gamma	96.88	Location	0.00000
	Scale	2.13452	
	Shape	0.92263	
2 - Gamma(E)	95.31	Location	3.02433e-4
	Scale	2.16511	
	Shape	0.90945	
3 - Weibull	84.38	Location	0.00000
	Scale	1.92959	
	Shape	0.95479	

Absolute Evaluation of Model 1 - Gamma
Evaluation: Good

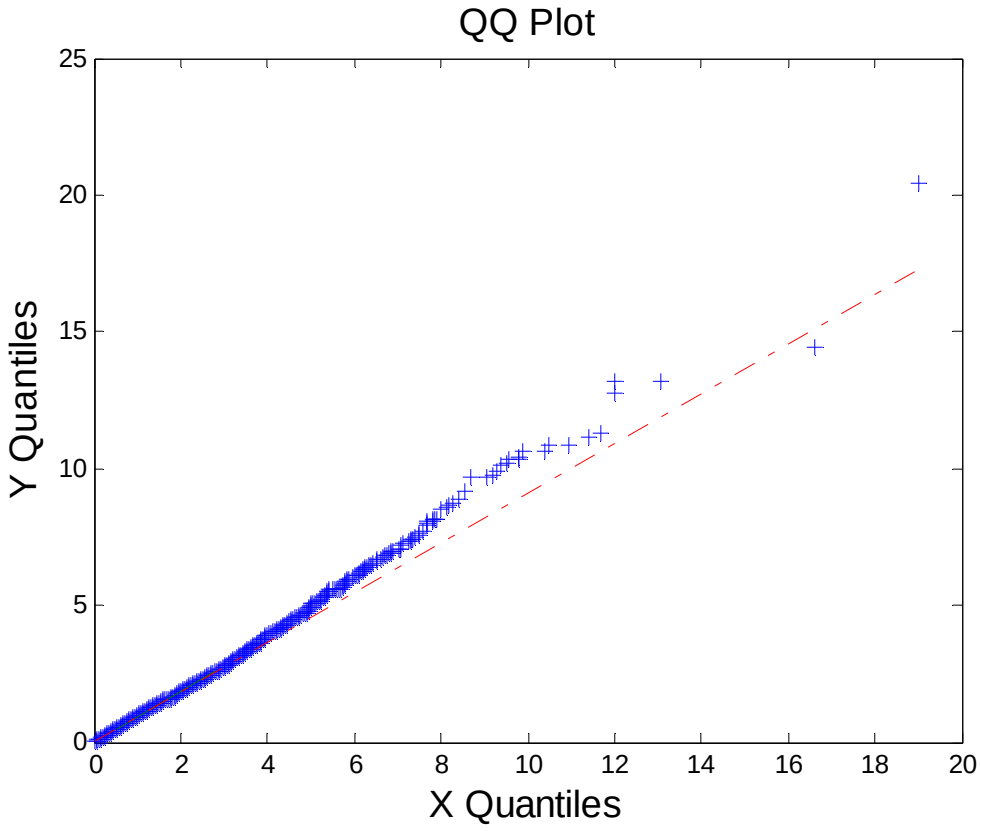

Simulated E field Statistics

1 – efield

Relative Evaluation of Candidate Models

Model	Relative Score		Parameters
1 - Weibull	100.00	Location	0.00000
	Scale	1.40477	
	Shape	1.96260	
2 - Weibull(E)	95.24	Location	0.01560
	Scale	1.38365	
	Shape	1.91509	
3 - Gamma	88.10	Location	0.00000
	Scale	0.41896	
	Shape	2.97515	

Absolute Evaluation of Model 1 - Weibull
Evaluation: Good

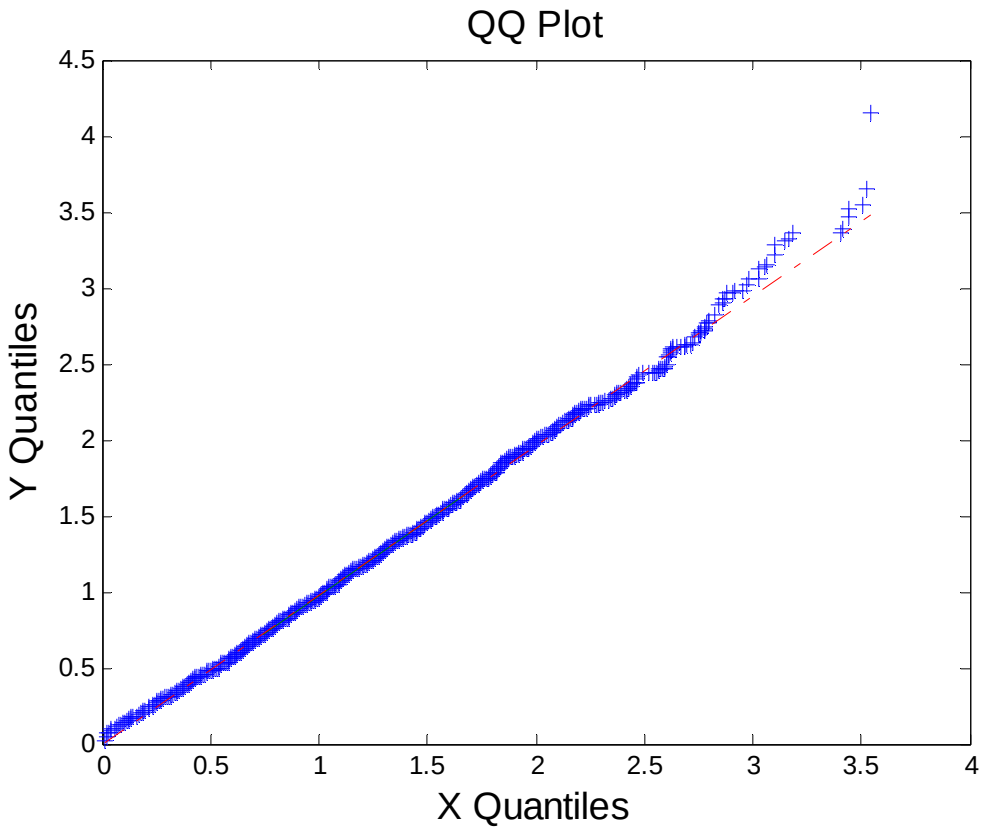

2- efield

Relative Evaluation of Candidate Models

Model	Relative Score		Parameters
1 - Weibull(E)	98.86	Location	8.28018e-3
	Scale	1.42632	
	Shape	1.99286	
2 - Weibull	96.59	Location	0.00000
	Scale	1.43727	
	Shape	2.01662	
3 - Gamma	90.91	Location	0.00000
	Scale	0.39297	
	Shape	3.24007	

Absolute Evaluation of Model 1 - Weibull(E)
Evaluation: Good

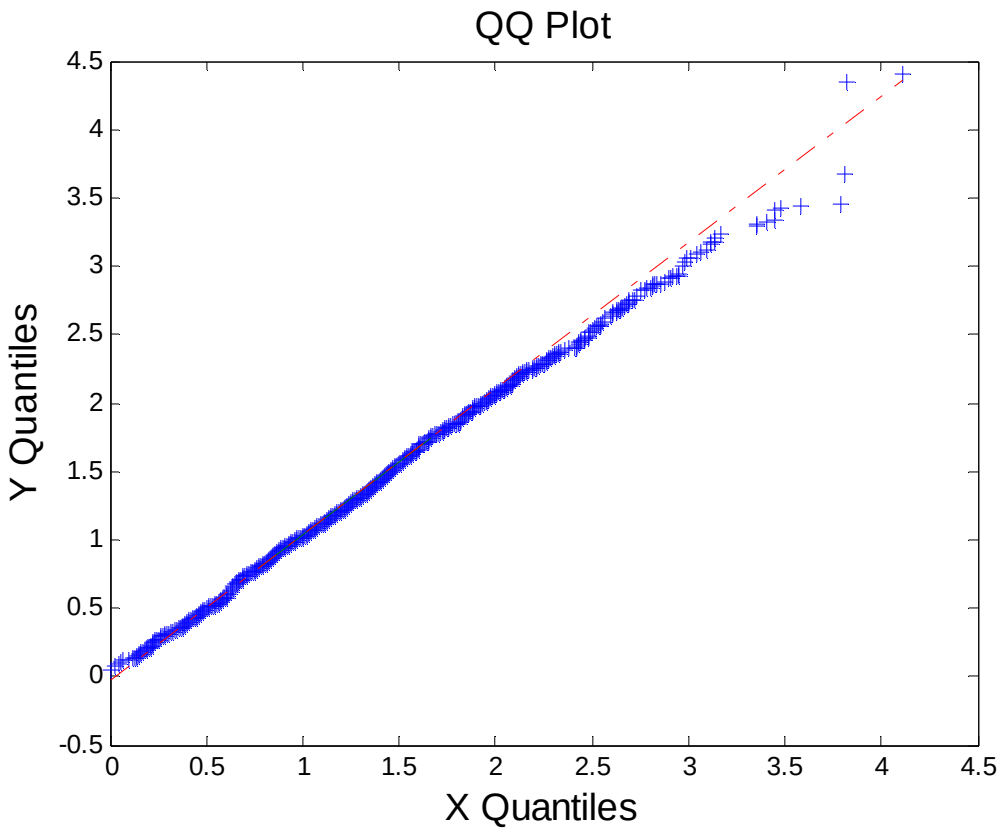

3 – efield

Relative Evaluation of Candidate Models

Model	Relative Score		Parameters
	Relative		
1 - Weibull	100.00	Location	0.00000
	Scale	1.38910	
	Shape	1.90958	
2 - Weibull(E)	95.00	Location	0.01739
	Scale	1.36527	
	Shape	1.85707	
3 - Erlang	88.75	Location	0.00000
	Scale	0.41116	
	Shape	3	

Absolute Evaluation of Model 1 - Weibull

Evaluation: Good

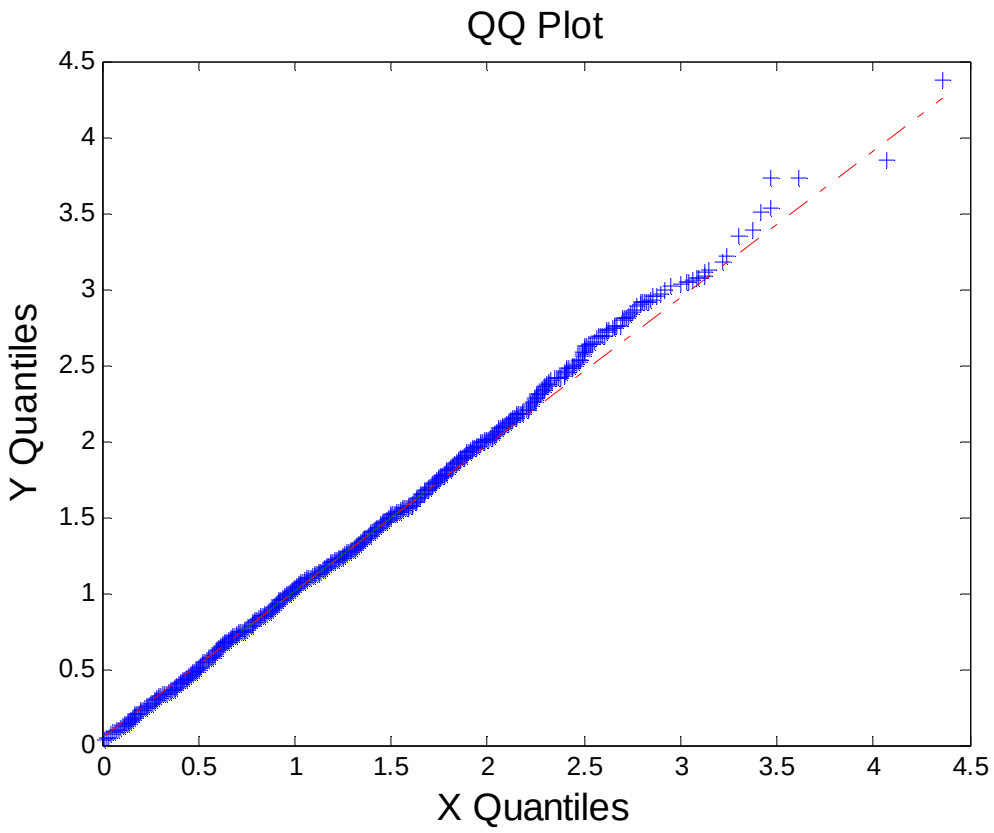

VITA

Vignesh Rajamani

Candidate for the Degree of

Doctor of Philosophy

Dissertation: ESTABLISHING PROBABILITY OF FAILURE OF A SYSTEM DUE TO ELECTROMAGNEITC INTERFERENCE

Major Field: Electrical Engineering

Biographical:

Education:

Completed the requirements for the Doctor of Philosophy in Electrical Engineering at Oklahoma State University, Stillwater, Oklahoma in July, 2010.

Completed the requirements for the Master of Science in Electrical Engineering at Oklahoma State University, Stillwater, Oklahoma in December, 2004.

Completed the requirements for the Bachelor of Science in Electronics and Communication Engineering at University of Madras, India in May, 2002.

Experience:

Co-Op, IBM, Research Triangle Park, NC (Summer ’07)

Research Associate, REFTAS and IEM, Oklahoma State University (2005)

Research Assistant and Teaching Assistant, REFTAS, Oklahoma State University (Jan ’06 – present)

Professional Memberships:

IEEE EMC Society, IEEE APS Society, Eta Kappa Nu, Phi Kappa Phi and Golden Key Member

Name: Vignesh Rajamani Date of Degree: July, 2010

Institution: Oklahoma State University Location: Stillwater, Oklahoma

Title of Study: ESTABLISHING PROBABILITY OF FAILURE OF A SYSTEM DUE TO ELECTROMAGNEITC INTERFERENCE

Pages in Study: 205 Candidate for the Degree of Doctor of Philosophy

Major Field: Electrical Engineering

Scope and Method of Study:

A wire placed inside the metallic box will serve as the equipment under test and the distributions of current and fields will be calculated via measurements. From the distribution, the probability of the observable exceeding a certain threshold can be determined. From the nature of the EME generated, the probability of threat due to EMI can be derived under some assumptions. Combining both the probabilities, the net probability of failure of the system could be determined. Reverberation chambers will be useful in measurements in this study as they simulate operating conditions of the EUT inside a cavity and as the EUT is exposed in all directions to the electromagnetic field, the uncertainty is also reduced. The probability models can provide insight into what type of testing is required to assure worst case testing with reasonable accuracy.

Findings and Conclusions:

The final outcome of this work is to establish the probability of failure due to current coupled onto a cable or a cable bundle located close to the wall of a cavity due to external or internal coupling of EM. The electromagnetic environment of the cavity was determined to estimate the probability of threat depending on the location of the cable inside the cavity. Given that the probability of threat exists, then the probability that the value of the current exceeding a certain threshold was determined. The environment in which the EUT operates and the influence of the environment on the observable that is being targeted was also determined which aids in the calculation of threshold probability. Finally, the net probability of failure of a system was determined from the individual probabilities. The major focus of this work was on the development of the methodology that is sufficiently general to obtain the distribution of any observable. The procedure developed could be used in different scenarios and from a class of distributions developed for each scenario, the probability of threat and probability of failure of a system due to EMI can be calculated.

ADVISER'S APPROVAL: Dr. Charles F. Bunting _____